Optical Characterization of Dynamic Exchange Coupling Interaction in Ferromagnetic Heterostructures

Xiao Liu

Jinan, Shandong, P. R. China

Bachelor of Science, University of Science
and Technology of China, 2014

A Dissertation presented to the Graduate Faculty of The College of William & Mary in Candidacy for the Degree of
Doctor of Philosophy

Department of Applied Science

College of William & Mary
August, 2019

APPROVAL PAGE

This Dissertation is submitted in partial fulfillment of
the requirements for the degree of

Doctor of Philosophy

Xiao Liu

Approved by the Committee, July, 2019

Committee Chair
Professor Gunter Luepke, Applied Science
College of William & Mary

Professor Mark Hinders, Applied Science
College of William & Mary

Professor Hannes Schniepp, Applied Science
College of William & Mary

Professor Gina Hoatson, Physics
College of William & Mary

ABSTRACT

This thesis presents the optical characterization of interfacial exchange coupling interaction in ferromagnetic bilayer heterostructures. Both static and dynamic magnetic response are investigated in the exchange-coupled Co_2FeAl/(Ga,Mn)As bilayer system using static magneto-optical Kerr effect (MOKE) and time-resolved magneto optical Kerr effect (TRMOKE) techniques. The goal of this thesis is to understand the underlying physics of the interfacial exchange coupling effect on the ultrafast spin dynamics in a ferromagnetic metal/ferromagnetic semiconductor bilayer heterostructure. Our finding provides a viable pathway for designing advanced semiconductor spintronic devices for ultrafast low-power spin manipulation.

First, a significant enhancement of the excitation efficiency of coherent magnetization precession is observed in the ferromagnetically exchange-coupled Co_2FeAl/(Ga,Mn)As bilayer heterostructures at temperatures below the Curie temperature of (Ga,Mn)As, $\boldsymbol{T_C}$ = 50 K, under photoexcitation of low-fluence, near-infrared pump pulses. The coherent magnetization precession persists to room temperature, indicating that proximity-induced ferromagnetism plays an important role in the optical excitation mechanism. A subsequent simulation of the temperature-dependent precession amplitude and frequency behavior is performed based on the Landau-Lifshitz-Gilbert (LLG) equation, suggesting that the high-efficiency excitation mechanism can be attributed to the modulation of the exchange coupling field at the interfacial area, which is induced by the emergence of the dynamic exchange coupling effect between the precessing magnetizations in the two ferromagnets.

Second, the Gilbert damping property of the magnetization precession in the Co_2FeAl/(Ga,Mn)As bilayer system is studied. At temperatures below the Curie temperature of (Ga,Mn)As, $\boldsymbol{T_C}$ = 50 K, ultrafast pump excitation creates a counter-precessing, exchange-coupled mode in the ferromagnetic bilayer. The precessing magnetization in the Co_2FeAl layer transfers a pure spin current directly into the (Ga,Mn)As layer at a certain intensity of external magnetic field where the Fe(Co) spins and the Mn spins precess at the same frequency. A photo-induced enhancement of the Gilbert damping constant $\boldsymbol{\alpha}$ is observed, indicating that spin-angular momentum is transferred at the resonance magnetic fields. This can be attributed to the effect of the interfacial dynamic exchange coupling interaction between the precessing magnetizations in two ferromagnetic layers. A corresponding phase shift of the magnetization precession is also observed at the resonance field where the Gilbert damping peak appears.

TABLE OF CONTENTS

ACKNOWLEDGEMENTS

I am truly grateful to everyone who has directly or indirectly supported and helped me during the completion of this dissertation. First and foremost, I would like to thank my advisor, Professor Gunter Luepke, for his guidance, encouragement and mentoring throughout my doctoral study at the College of William and Mary. He has always provided enthusiasm and perspective for the research process. This dissertation would not have been possible without his help, support and guidance.

Special appreciation goes to Professor Haibin Zhao and his group members – Haochen Yuan and Jingyu Shi from Fudan University for their contribution to the characterization work. I truly appreciate their sharing of high-quality data and inspired visions about the projects.

I owe special thank to Professor Jianhua Zhao and his group members from Institute of Semiconductors, Chinese Academy of Sciences, Beijing, China. I am indebted to them for providing a series of high-quality samples.

I'm similarly grateful to my lab mates: Wei Zheng, Xin Ma, Fan Fang, and Peiwen Liu. I appreciate their friendships and collective encouragement to finish this dissertation. In particular, I would like to thank Wei Zheng for assistance in maintaining laser systems and Fan Fang for assistance in data collection and discussion. I have enjoyed every moment that we have worked together.

My appreciation would also go to my doctoral dissertation committee members: Professor Mark Hinders of Applied Science, Professor Hannes Schniepp of Applied Science, and Professor Gina Hoatson of Physics for their participation, comments and suggestions in the review of this dissertation.

Finally, I wish to express my sincere gratitude to my family – Lesen Liu, Shuling Ding, and Wenning Tao. Their truly and constant love and encouragement have always been the source of my strength and motivation. In particular, I would like to appreciate my wife Wenning Tao for her great understanding and support during my doctoral study. I would also like to thank my cat King for his company. Anything I have been able to accomplish is a tribute to them.

This dissertation is dedicated to my family

LIST OF TABLES

LIST OF FIGURES

Chapter 1

Introduction

This chapter introduces the basic concept of the spin dynamics in ferromagnetic heterostructures. Section 1.1 presents an introduction to the ferromagnetic material and spintronic devices based on the precise control of the ultrafast magnetization dynamics. Section 1.2 discusses the magnetization switching and dynamics in the ferromagnets. The spin injection and spin-transfer torque effect are investigated in Section 1.3. Section 1.4 provides a general review of the interlayer and interfacial exchange coupling interaction in ferromagnetic multilayer heterostructures. Section 1.5 states the scope of this dissertation.

1.1 Ferromagnetic Material and Spintronic Devices

Permanent magnets can be divided into two types according to their alignment levels of the magnetic ordering under an external applied magnetic field: the ferromagnetic (FM) material exhibit a strict alignment of magnetic magnetization, while in the ferrimagnet material, although the spontaneous magnetization still exists, a small portion of magnetic

moments align in an opposite direction so that the spontaneous magnetization is slightly weaken [1]. In FM material, the magnetic fields of the domains, where the unpaired electron spins line up parallel with each other, align in random orientations, i.e., no net magnetic field is generated in the bulk material. When an external magnetic field is applied on FM material, the magnetic fields of these individual domains that originally align in different directions are attracted to line up along the direction of the applied magnetic field. As a result, the applied magnetic field is expected to be strengthened [2-3]. The spontaneous magnetization in the magnetized FM material preserves even when the applied magnetic field is removed.

The major difference between FM metal and non-magnetic normal metal results from the distribution of the spin polarization at the Fermi level. The density of states for the spin-up and spin-down electrons are equal in the normal metal due to time-reversal symmetry, causing the net spin polarization to be zero, as shown in Fig. 1.1(a). However, in FM material time-reversal symmetry is broken by the spontaneous magnetization. The Coulomb interaction induces exchange splitting of electron spins and hence the density of states for spin-up and spin-down electrons are unequal near the Fermi level (Fig. 1.1(b)). Since spin transport is usually achieved based on the existence of spin polarization, the inequality of the density of states at the Fermi level makes the FM metal an ideal medium for ultrafast low-power spin detection and manipulation [4].

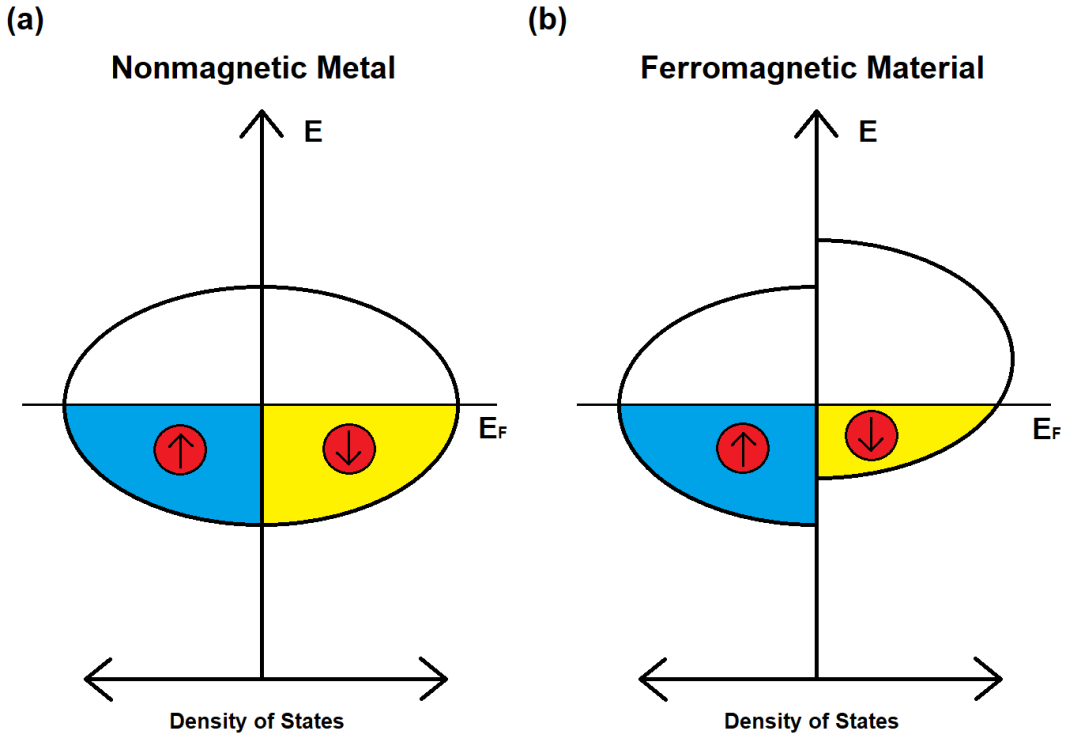

Figure 1.1 Schematics of density of states for spin-up and spin-down electrons near Fermi level in (a) nonmagnetic metal and (b) ferromagnetic material. E_F indicates Fermi level.

In the past decades, FM materials have been widely utilized in magnetic recording and spintronics. One of the most well-known commercial application is the giant magnetoresistance (GMR) read-head which is designed based on the spin-valve structures. A spin-valve structure contains two FM metal layers which are separated by a very thin non-magnetic conducting spacer layer. One of the two FM layers behaves as a “hard” layer with a large coercivity which makes its magnetization

orientation difficult to be switched. The other FM layer acts as a “soft” layer with a relatively small coercivity, i.e., a very small externally applied magnetic field is able to reverse its magnetization direction. The two magnetizations in both FM layers are either parallel or antiparallel depending on the direction of the small external magnetic field. Typically, the electrical resistance for the antiparallel alignment is more than %10 higher than that for the parallel configuration at room temperature, which is considered as the result of giant magnetoresistive effect [5]. Based on this property, the GMR read-head is designed and utilized in a hard disk, as seen in Fig. 1.2. As a result, an ultrafast reading rate and high density of stored information (from 1 Gb/in^2 to 600 Gb/in^2 by the end of 2007 [6]) have been achieved through the exchange-biased spin-valve structure.

Today, in order to increase the access rate and reduce the energy consumption in the magnetic recording process, more and more novel designs in spintronic devices have been investigated. An advanced spintronic application, Magnetic Random Access Memory (MRAM), is designed based on the high tunnel magnetoresistance in magnetic tunnel junctions (MTJs) [6]. The MTJs can be created by replacing the nonmagnetic conducting normal metal spacer layer in the spin valves by a nonmagnetic insulating spacer layer in order to achieve a much higher magnetoresistance. Compared to the conventional silicon electrically erasable programmable read-only memory and flash memory, MRAM

exhibits very short access time with low power consumption and non-volatile property of magnetic memories [7]. Thus, it attracts abundant interest in the computer industry.

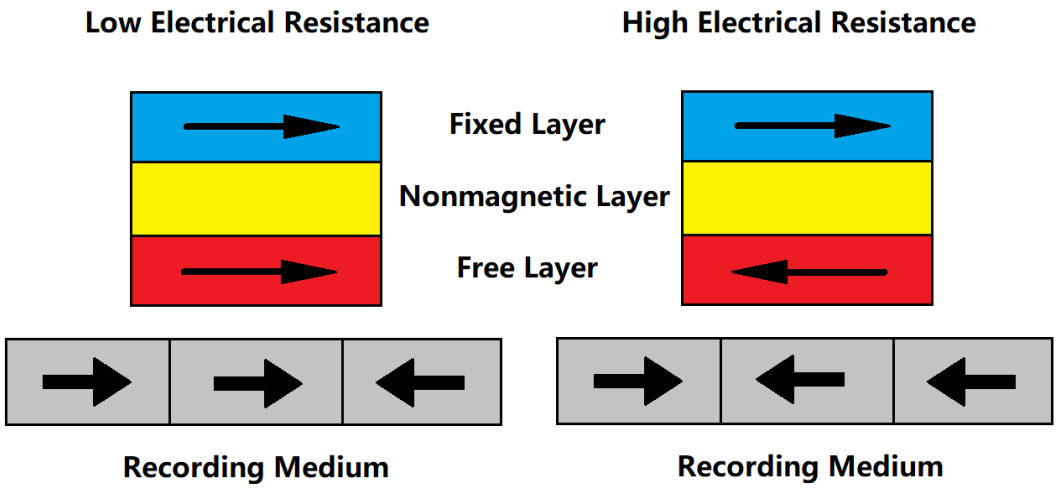

Figure 1.2 Schematics of spin-valve structure in giant magnetoresistance read-head. Black arrows indicate the direction of magnetization. Low electrical resistance is related to parallel alignment while high electrical resistance occurs at antiparallel alignment.

Besides the ferromagnetic metals which have been well studied and used in spintronic devices, ferromagnetic semiconductors also show large-scale potential applications in ultrafast low-power spin manipulation, because they combine the advantage of both metals and semiconductors such as the large conductivity and high spin polarization of charge carriers. By utilizing the spin degrees of freedom, the FM semiconductor is expected to provide high density of information storage and new spintronic

functionalities of both ferromagnetic and semiconductor material systems. The spin manipulation can be achieved through connection between the magnetic states and optical signal in FM semiconductor spintronic devices, leading to an improvement of access speed and energy consumption in the data recording process.

Although FM semiconductor spintronics has not been utilized as widely as FM metallic devices, they already show great potential in the industry. One of the success applications is the spin transistor, which was proposed by Datta and Das in 1990, as shown in Fig. 1.3 [9]. As an advanced version of the conventional electronic transistor, the spin transistor is a semiconductor-based spin-dependent device, which is sensitive to a magnetic field. First, the spin polarized electrons enter the spin transistor channel from the FM source electrode. When the electrons propagate through the channel, their spins start to precess under the influence of the spin-orbit coupling induced by the intrinsic magnetic field. An applied voltage on the gate is able to induce a change of the effective magnetic field and hence tune the strength of the Rashba spin-orbit coupling, leading to a modulation of the electron spin precession. As the electrons reach the FM drain electrode on the other side, they will only be transmitted into the collector if their resulting spin polarization direction is parallel to the magnetization direction in the FM drain (low resistance). Otherwise, the spin electrons will be reflected (high resistance). Therefore,

switching between low- and high-resistance states can be realized. Note that the spin states can be detected or manipulated without electric current, which allows a small size of the spin transistor with low power consumption to achieve more sensitive detection. Furthermore, the semi-permanent character of the spins makes it possible to realize non-volatile solid state storage.

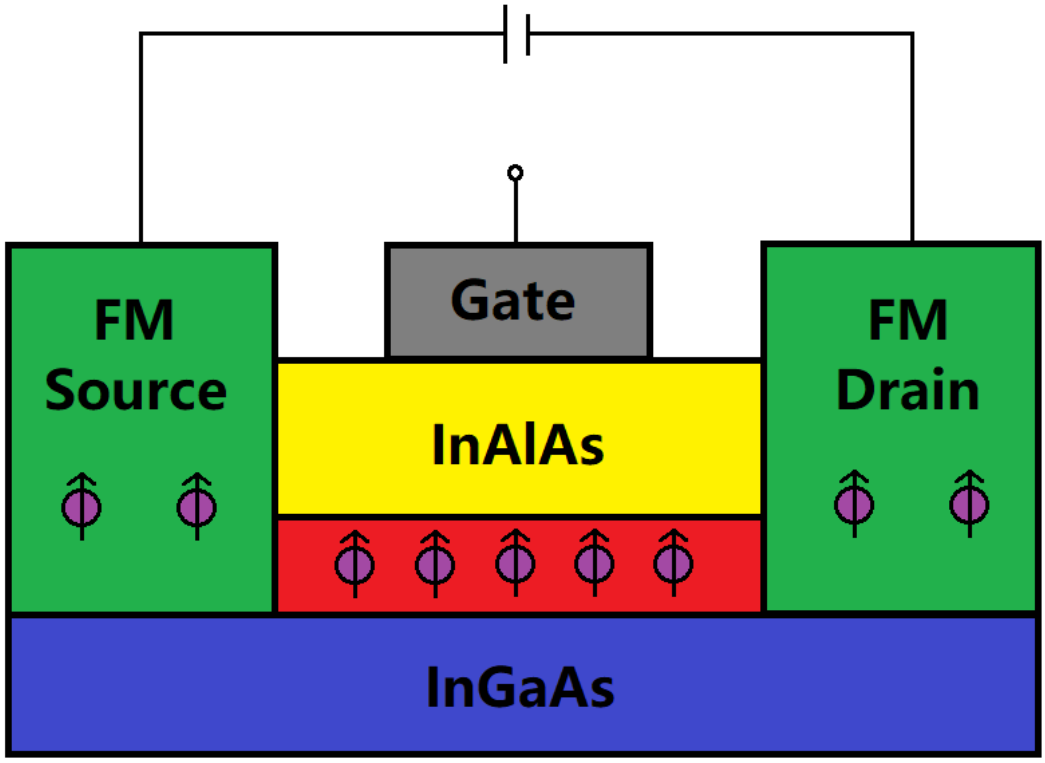

Figure 1.3 Schematic of spin transistor (Datta-Das transistor). Electrons are shown in purple circles with arrows.

1.2 Magnetization Switching and Dynamics

In the past decades, the magnetization switching and dynamics attracted lots of interest for applications of advanced spintronic devices. In general, the magnetization switching refers to the process that reverses the direction of magnetization in a magnetized medium from its original stable direction. Today, there are several methods to rotate the magnetization by 180 degrees. A direct way is to apply an external magnetic field in the direction opposite to the initial magnetization state, which is considered as the conventional approach to achieve the magnetization reversal [10-12] and has been utilized in spintronic devices such as hard disks.

However, a potential limitation occurs at high density of information storage. The increasing storage density requires larger magnetic anisotropy, which leads to higher energy barrier for magnetization switching between opposite states, causing large energy consumption. Moreover, the large applied magnetic field may induce an unexpected influence on the units adjacent to the target cell. Recently, this limitation has been eliminated by an interesting strategy where the magnetization switching can be realized by spin injection via the spin-polarized current. This directly triggers the local magnetization switching in the magnetized sample, which has been investigated both experimentally [13-15] and theoretically [16]. This novel approach, in particular, exhibits significant

potential for applications of spintronic devices such as MRAM, because it can be used to address only the target memory cell without affecting adjacent units, which is difficult to be achieved simply by applying an external magnetic field [17]. Furthermore, the magnetization switching can also be realized optically, as reported by Stanciu et al., who switched the magnetization by a single 40-femtosecond circular-polarized laser pulse without applying any external magnetic field [18]. As the size of storage units is getting smaller with higher density of information stored, the precise manipulation of the magnetization in the ferromagnetic medium becomes crucial in the realization of spintronic devices.

Typically, the magnetization switching and dynamics can be described by the Landau-Lifshitz-Gilbert (LLG) equation [19]:

$$\frac{\partial \boldsymbol{M}}{\partial t} = -\gamma\left(\boldsymbol{M} \times \boldsymbol{H}_{eff}\right) + \alpha \boldsymbol{M} \times \frac{\partial \boldsymbol{M}}{\partial t},$$

where the first term on the right side represents the precession motion of the magnetization $\boldsymbol{M}$ along an effective field $\boldsymbol{H}_{eff}$ with the gyromagnetic ratio γ. The second term represents the damping of the precession motion towards $\boldsymbol{H}_{eff}$ with the Gilbert damping constant α.

In the design of spintronic devices, the data access rate is one of the most important characters to assess the performance of a magnetic device. High data access rate requires the magnetization to be not only switched but also stabilized in a short time scale. In most magnetic

transition metals, the damping factor α is relatively small and the recovery time of the magnetization precession may be several nanoseconds, which is a limitation for the rate of magnetization switching. Thus, it is important to achieve larger α in order to push the data access rate beyond this limitation. A lot of effort has been devoted into the enhancement of the Gilbert damping constant [20-24].

Experimentally, the magnetization switching and dynamics can be investigated by the time-resolved magneto-optical Kerr effect (TRMOKE) technique. With ultrafast pulsed laser system, the excitation, precession and recovery process of the bulk magnetization in a magnetized sample can be observed on a femtosecond time scale, which will enable the development of advanced ultrafast spintronic devices.

1.3 Spin Injection and Spin Transfer Torque Effect

As discussed above, the limitation of applying an external magnetic field in magnetic recording creates a bottleneck for the realization of advanced spintronic devices. One promising approach is to achieve magnetization switching via spin injection of spin-polarized current, as depicted in Fig. 1.4.

Here, we consider the case of writing information into an MRAM cell with the spin transfer torque (STT) effect [25]. A thick FM layer and a thin FM layer are separated by a tunneling barrier. The spin-polarized current can be triggered either electrically or by optical excitation. When the spin-unpolarized current arrives at the thick FM electrode, the electrons with spins parallel to the local magnetization direction pass through the thick FM layer while the electrons with antiparallel spins get reflected by the interface. The outgoing spin-polarized current is then injected into the thin FM electrode, transferring spin angular momentum into this layer and hence exerting a spin transfer torque on the local magnetization to align it parallel to the magnetization direction in the thick FM electrode. Therefore, the operation of writing “0” is achieved.

If the spin-unpolarized current goes through the thin ferromagnetic electrode first, the spins of electrons can’t be fully polarized due to the short propagating length in this layer. This causes a significant spin scattering when the conducting electrons arrive at the interface between the tunneling barrier and the thick FM layer. As a consequence, the electrons with spin polarization antiparallel to the magnetization direction in the thick FM electrode are reflected back and then enter the thin FM layer, exerting a spin transfer torque on the local magnetization to align it antiparallel to that in the thick layer by transferring opposite spin angular momentum. Therefore, the operation of writing “1” is realized.

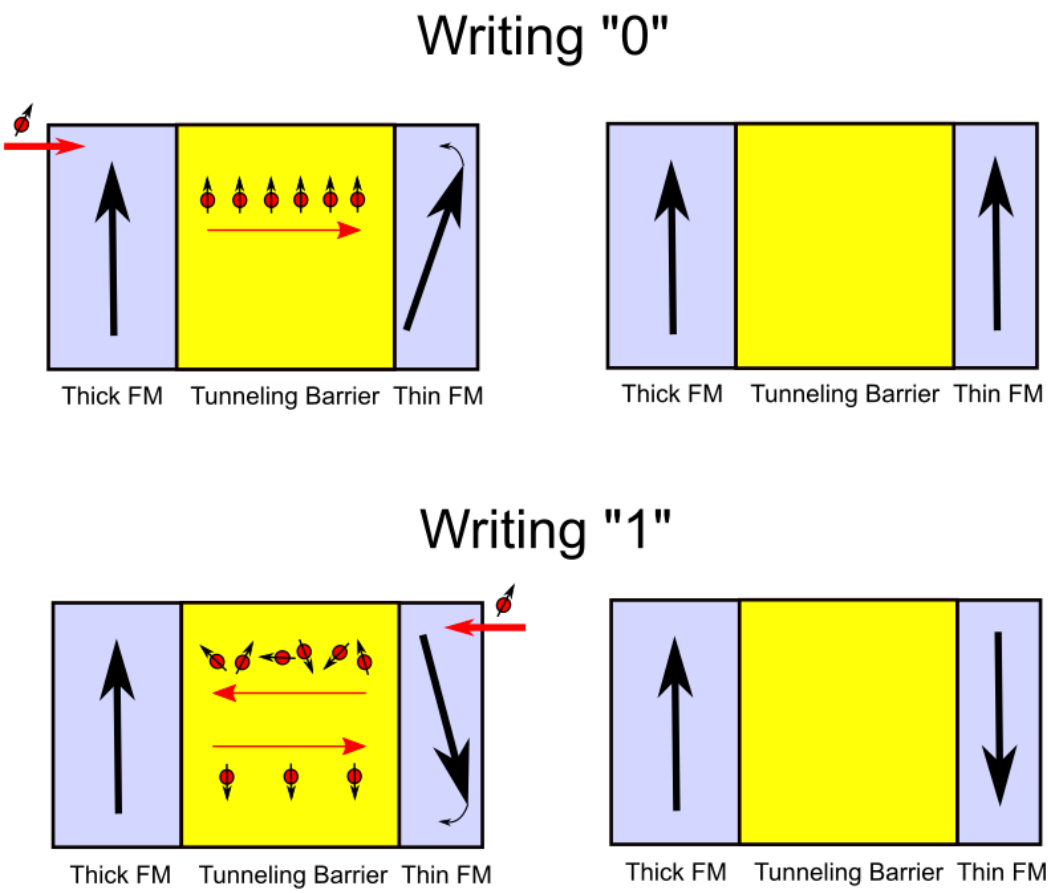

Figure 1.4 Schematics of writing process in magnetic recording. Black arrows indicate magnetization. Red arrows exhibit current flowing directions.

1.4 Interlayer and Interfacial Exchange Coupling Interaction

The systematic study of the interlayer and interfacial exchange coupling interaction has significantly contributed to the realization of rapid low-power magnetic recording spintronic devices. In general, the interlayer exchange coupling interaction refers to the effect that the magnetizations in two ferromagnetic layers separated by a nonmagnetic spacer layer are exchange-coupled to each other [27]. The first experimental demonstration of the interlayer exchange coupling effect was performed in 1986 both in transition metal multilayers [28] and in rare-earth multilayers [29-30]. The subsequent study observed a change in the electrical resistance between the parallel configuration and antiparallel configuration of the magnetization in both ferromagnetic layers, which is the giant magnetoresistance that has been applied in magnetic recording devices, as discussed in Section 1.1 [31].

Two kinds of interactions can be taken into account as the origin of the interlayer exchange coupling interaction. One is the magnetic dipole-dipole interaction, also known as dipolar coupling, which refers to the direct interaction between two magnetic dipoles [32]. The dipolar coupling may have a contribution in inhomogeneous magnetic layers, which are not saturated and spilt into magnetic domains. However, modern fabrication techniques are able to ensure the high quality of the homogeneously

magnetized sample, so the influence from dipolar coupling can be neglected [33]. The other effect is an indirect interlayer interaction between the nuclear magnetic moments or localized electron spins mediated by the conduction electrons, which is known as the oscillatory coupling or Ruderman–Kittel–Kasuya–Yosida (RKKY) interaction [34-36]. This effect well explains the origin of the interlayer exchange coupling in the spin valve structures and has let to important advances in condensed matter physics.

In a ferromagnetic bilayer system, the magnetic coupling energy per unit area can be simply described by:

$$\boldsymbol{E = Jcos(\theta)},$$

where $\boldsymbol{\theta}$ denotes the angle between the magnetizations in two ferromagnetic layers and $\boldsymbol{J}$ is the exchange coupling constant. Here only the bilinear form is considered. Higher order terms, which originate from the non-colinear alignment of two magnetizations due to the roughness, are neglected [37-38]. Both, static and dynamic exchange coupling interactions have a contribution to $\boldsymbol{J}$. The static ferromagnetic exchange coupling interaction exists in the parallel alignment of the magnetizations in two ferromagnetic layers, while the dynamic exchange coupling effect occurs only between two precessing magnetizations through spin pumping effect, as shown in Fig. 1.5.

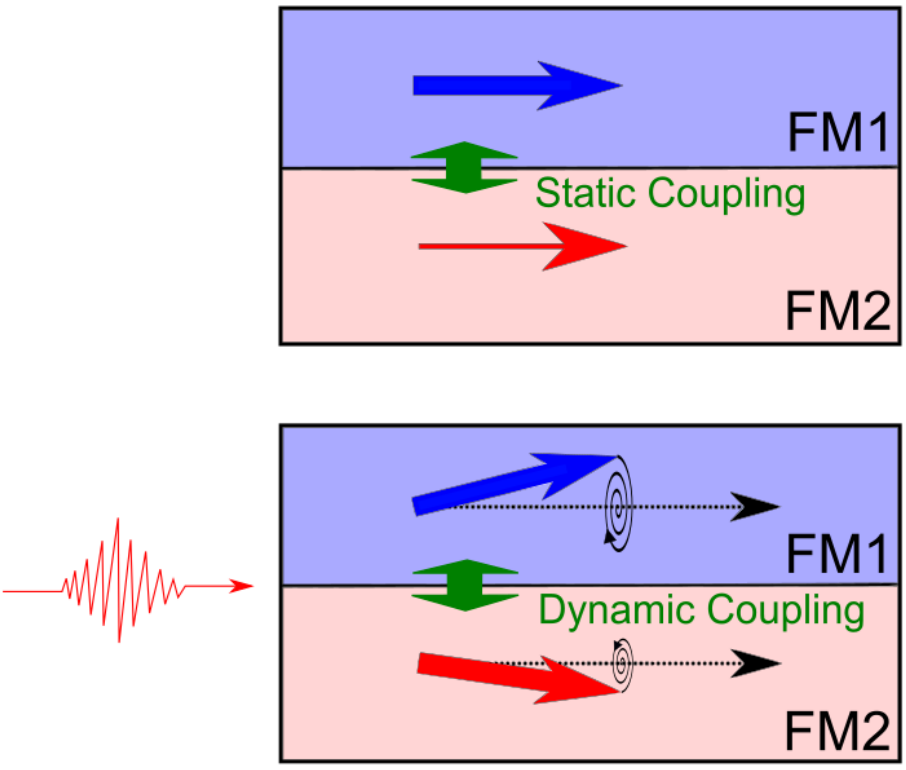

Figure 1.5 Schematics of static and dynamic exchange coupling interactions. Red wave represents optical excitation. Blue and red arrows indicate magnetization in FM1 and FM2, respectively.

The interfacial exchange coupling interaction originates from the direct contact of two adjacent layers in a magnetic bilayer/multilayer medium. Both the crystal lattice structure and the magnetic property at the interface may have a contribution to the interfacial exchange coupling effect. In general, there are two novel phenomena directly induced by the interfacial exchange coupling interaction: the exchange bias effect and the magnetic proximity effect, which may occur alone or simultaneously in

different types of multilayer heterostructures and nanoparticle systems [39-40].

The exchange bias effect or exchange anisotropy, which exists at the interface of the ferromagnet/antiferromagnet, describes the process of a shift in the soft magnetization curve of a FM layer due to the influence of the hard magnetization configuration in the adjacent AFM layer [41]. Typically, it can be observed in the difference between the field-cooled hysteresis loops and zero field-cooled hysteresis loops [40], which was first discovered by Meiklejohn and Bean in 1956 [42]. A lot of studies on the exchange bias effect have been achieved in the past decades on a variety of exchange-coupled systems including magnetic multilayers [43], core–shell type nanoparticles [44] and inhomogeneous materials [42, 45].

In contrast to the exchange bias effect, the magnetic proximity effect, another effect arising from the interfacial exchange coupling interaction, doesn't attract that much interest until recent years [46-50]. The magnetic proximity effect refers to the mechanism that one or several surface layers in a paramagnetic/nonmagnetic layer in proximity to a FM layer can be magnetized by the FM ordering in the adjacent ferromagnet [46]. Either ferromagnetic or antiferromagnetic coupling are expected to be formed, depending on the atomic structure at the interface [49-50]. Zuckermann et al reported that the magnetic ordering temperature of the paramagnetic component is able to be raised with increasing thickness of the adjacent

FM layer [40, 46], which is further proved by the increased Curie temperature or Neel temperature reported in later studies [48, 51-53]. Some other novel features such as the enhanced perpendicular magnetic anisotropy in a ferromagnet/antiferromagnet bilayer system [54], the increased temperature of reorientation transition temperature in a FM layer [55] and the increased coercivity of a ferromagnet/antiferromagnet bilayer at temperatures higher than the Neel temperature [56] are investigated in the past decade [40].

Figure 1.6 presents an interfacial ferromagnetic exchange coupling interaction in a Co_2FeAl/(Ga,Mn)As bilayer system. The spin polarization in the ferromagnetic semiconductor layer which is exchange-coupled to the adjacent ferromagnetic metal layer reaches the depth of 2.11 nm at room temperature [49]. At temperatures above the Curie temperature $\boldsymbol{T_C}$ = 50 K, the interfacial layers in the (Ga,Mn)As film are magnetized by the ferromagnetic ordering in the Co_2FeAl layer due to the magnetic proximity effect, while the bulk (Ga,Mn)As medium remains disordered, i.e. in the paramagnetic phase.

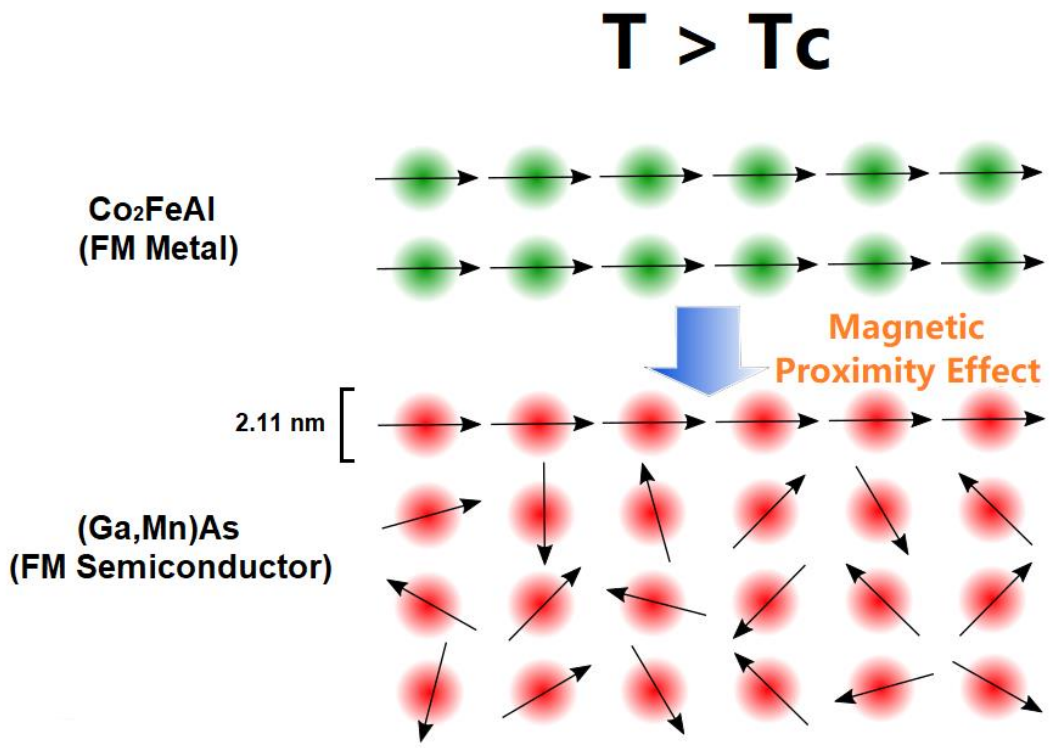

Figure 1.6 Schematic of magnetic proximity effect in Co_2FeAl/(Ga,Mn)As bilayer system

1.5 Scope of this Dissertation

The fundamental understanding of the interfacial exchange coupling effect on the ultrafast spin dynamics in a ferromagnetic bilayer heterostructure is the major focus of this dissertation. The half-metallic Heusler alloy, Co_2FeAl, possesses large spin polarization [57] with high

Curie temperature [58], which is crucial for spin-torque oscillators due to low switching current density. The (Ga,Mn)As material also exhibits large potential in the development of spin-based devices [59] due to its pronounced carrier effect on the magnetic properties [60]. As a promising exchange-coupled system – FM metal/FM semiconductor, the Co_2FeAl/(Ga,Mn)As bilayer makes it possible to effectively modulate the magnetic response through a small alteration of the exchange coupling interaction. For the first time, the high-efficient excitation mechanism induced by the dynamic exchange coupling effect in the Co_2FeAl/(Ga,Mn)As bilayer heterostructure is investigated under ultrafast low-power pump excitation.

Chapter 2 presents the basic experimental techniques utilized in this dissertation for the optical characterization of the bulk static and dynamic magnetization behavior under ultrafast photoexcitation. The magneto-optical Kerr effect (MOKE) is used to study the static bulk magnetic response. The time-resolved magneto-optical Kerr effect is used to systematically investigate the ultrafast magnetization dynamics in time domain.

Chapter 3 presents a study of the high-efficiency excitation mechanism in the ferromagnetically exchange-coupled Co_2FeAl/(Ga,Mn)As bilayer system. By applying an external magnetic field, a strong temperature dependence of the magnetization precession amplitude is

observed through the TRMOKE technique at the temperature below the Curie temperature of (Ga,Mn)As ***Tc*** = 50 K. The precession amplitude increases dramatically with decreasing temperature. A simulation of the precession dynamics based on the Landau-Lifshitz-Gilbert (LLG) equation is performed, indicating that the high-efficiency excitation can be attributed to the modulation of the interfacial exchange coupling which is induced by the emergence of the dynamic exchange coupling effect.

Chapter 4 presents a study of the photo-enhanced Gilbert damping constant and the corresponding phase shift in the Co_2FeAl/(Ga,Mn)As bilayer system. The simulation of the magnetization precession shows that the Gilbert damping constant can be significantly enhanced at a certain intensity of the external applied magnetic field below the Curie temperature ***Tc*** = 50 K. The damping peak shifts to higher field with increasing temperature. A phase shift of the magnetization precession in relation to the magnetic field is also observed corresponding to the damping peak. The enhancement of the Gilbert damping constant can be attributed to the spin pumping effect between the precessing magnetizations in the two ferromagnetic layers, which are dynamically exchange-coupled.

Chapter 5 provides the summary of this dissertation.

References:

[1] https://en.wikipedia.org/wiki/Ferromagnetism

[2] https://theory.uwinnipeg.ca/mod_tech/node101.html

[3] http://hyperphysics.phy-astr.gsu.edu/hbase/Solids/ferro.html

[4] http://asdn.net/asdn/electronics/spintronics.php

[5] https://en.wikipedia.org/wiki/Spin_valve

[6]https://www.sigmaaldrich.com/technical-documents/articles/materials-science/vistas-in-current-magnetic-materials-research.html

[7] Hu, Jia-Mian, et al. "High-density magnetoresistive random access memory operating at ultralow voltage at room temperature." *Nature communications* 2 (2011): 553.

[8] Chen, Lin, and Jianhua Zhao. "Magneto-Transport Behaviors of (Ga, Mn) As Based Nano-structures and Devices." *Handbook of Spintronics* (2016): 585-614.

[9] Datta, Supriyo, and Biswajit Das. "Electronic analog of the electro-optic modulator." *Applied Physics Letters* 56.7 (1990): 665-667.

[10] Gerrits, Th, et al. "Ultrafast precessional magnetization reversal by picosecond magnetic field pulse shaping." *Nature*418.6897 (2002): 509.

[11] Mallinson, John C. "Damped gyromagnetic switching." *IEEE transactions on magnetics* 36.4 (2000): 1976-1981.

[12] Bertotti, G., et al. "Comparison of analytical solutions of Landau–Lifshitz equation for “damping” and “precessional” switchings." *Journal of applied physics* 93.10 (2003): 6811-6813.

[13] Kubota, H., et al. "Magnetization switching by spin-polarized current in low-resistance magnetic tunnel junction with MgO [001] barrier." *IEEE transactions on magnetics* 41.10 (2005): 2633-2635.

[14] Hayakawa, Jun, et al. "Current-driven magnetization switching in CoFeB/MgO/CoFeB magnetic tunnel junctions." *Japanese Journal of Applied Physics* 44.9L (2005): L1267.

[15] Yang, Tao, Takashi Kimura, and Yoshichika Otani. "Giant spin-accumulation signal and pure spin-current-induced reversible magnetization switching." *Nature Physics* 4.11 (2008): 851.

[16] Zhang, Shufeng, P. M. Levy, and A. Fert. "Mechanisms of spin-polarized current-driven magnetization switching." *Physical review letters* 88.23 (2002): 236601.

[17] http://wpage.unina.it/mdaquino/PhD_thesis/main/node39.html

[18] Stanciu, C. D., et al. "All-optical magnetic recording with circularly polarized light." *Physical review letters* 99.4 (2007): 047601.

[19] Gilbert, Thomas L. "A Lagrangian formulation of the gyromagnetic equation of the magnetization field." *Phys. Rev.*100 (1955): 1243.

[20] Tserkovnyak, Yaroslav, Arne Brataas, and Gerrit EW Bauer. "Enhanced Gilbert damping in thin ferromagnetic films." *Physical review letters* 88.11 (2002): 117601.

[21] Kapelrud, André, and Arne Brataas. "Spin pumping and enhanced Gilbert damping in thin magnetic insulator films." *Physical review letters* 111.9 (2013): 097602.

[22] Emley, N. C., et al. "Time-resolved spin-torque switching and enhanced damping in permalloy/Cu/permalloy spin-valve nanopillars." *Physical review letters* 96.24 (2006): 247204.

[23] Tserkovnyak, Yaroslav, Arne Brataas, and Gerrit EW Bauer. "Dynamic exchange coupling and Gilbert damping in magnetic multilayers." *Journal of applied physics* 93.10 (2003): 7534-7538.

[24] Liu, Yi, et al. "Interface enhancement of Gilbert damping from first principles." *Physical review letters* 113.20 (2014): 207202.

[25] Slonczewski, John C. "Conductance and exchange coupling of two ferromagnets separated by a tunneling barrier." *Physical Review B* 39.10 (1989): 6995.

[26] Chappert, Claude, Albert Fert, and Frédéric Nguyen Van Dau. "The emergence of spin electronics in data storage." *Nanoscience And Technology: A Collection of Reviews from Nature Journals*. 2010. 147-157.

[27] Stiles, Mark D. "Interlayer exchange coupling." *Journal of Magnetism and Magnetic Materials* 200.1-3 (1999): 322-337.

[28] Grünberg, P. E. T. E. R., et al. "Layered magnetic structures: Evidence for antiferromagnetic coupling of Fe layers across Cr interlayers." *Physical review letters* 57.19 (1986): 2442.

[29] Majkrzak, C. F., et al. "Observation of a magnetic antiphase domain structure with long-range order in a synthetic Gd-Y superlattice." *Physical review letters* 56.25 (1986): 2700.

[30] Salamon, M. B., et al. "Long-range incommensurate magnetic order in a Dy-Y multilayer." *Physical review letters* 56.3 (1986): 259.

[31] Baibich, Mario Norberto, et al. "Giant magnetoresistance of (001) Fe/(001) Cr magnetic superlattices." *Physical review letters* 61.21 (1988): 2472.

[32]https://en.wikipedia.org/wiki/Magnetic_dipole%E2%80%93dipole_interaction

[33] Bruno, P. "Interlayer exchange interactions in magnetic multilayers." *Magnetism: Molecules to Materials III* (2002): 329.

[34] Ruderman, Melvin A., and Charles Kittel. "Indirect exchange coupling of nuclear magnetic moments by conduction electrons." *Physical Review* 96.1 (1954): 99.

[35] Kasuya, Tadao. "A theory of metallic ferro-and antiferromagnetism on Zener's model." *Progress of theoretical physics* 16.1 (1956): 45-57.

[36] Yosida, Kei. "Magnetic properties of Cu-Mn alloys." *Physical Review* 106.5 (1957): 893.

[37] Slonczewski, J. C. "Overview of interlayer exchange theory." *Journal of Magnetism and magnetic materials* 150.1 (1995): 13-24.

[38] Demokritov, S. O. "Biquadratic interlayer coupling in layered magnetic systems." *Journal of Physics D: Applied Physics*31.8 (1998): 925.

[39] Manna, P. K., et al. "The magnetic proximity effect in a ferrimagnetic Fe3O4 core/ferrimagnetic γ-Mn2O3 shell nanoparticle system." *Journal of Physics: Condensed Matter*23.50 (2011): 506004.

[40] Manna, P. K., and S. M. Yusuf. "Two interface effects: Exchange bias and magnetic proximity." *Physics Reports*535.2 (2014): 61-99.

[41] https://en.wikipedia.org/wiki/Exchange_bias

[42] Meiklejohn, William H., and Charles P. Bean. "New magnetic anisotropy." *Physical review* 102.5 (1956): 1413.

[43] Nogués, J., et al. "Positive Exchange Bias in Fe F 2-Fe Bilayers." *Physical review letters* 76.24 (1996): 4624.

[44] Zeng, Hao, et al. "Tailoring magnetic properties of core/shell nanoparticles." *Applied Physics Letters* 85.5 (2004): 792-794.

[45] Kouvel, J. S. "A ferromagnetic-antiferromagnetic model for copper-manganese and related alloys." *Journal of Physics and Chemistry of Solids* 24.7 (1963): 795-822.

[46] Zuckermann, M. J. "The proximity effect for weak itinerant ferromagnets." *Solid State Communications* 12.7 (1973): 745-747.

[47] Unguris, John, R. J. Celotta, and Daniel T. Pierce. "Magnetism in Cr thin films on Fe (100)." *Physical review letters* 69.7 (1992): 1125.

[48] Maccherozzi, F., et al. "Evidence for a magnetic proximity effect up to room temperature at Fe/(Ga, Mn) As interfaces." *Physical review letters* 101.26 (2008): 267201.

[49] Nie, S. H., et al. "Ferromagnetic interfacial interaction and the proximity effect in a Co 2 FeAl/(Ga, Mn) As bilayer." *Physical review letters* 111.2 (2013): 027203.

[50] Sperl, Matthias, et al. "Reorientation transition of the magnetic proximity polarization in Fe/(Ga, Mn) As bilayers." *Physical Review B* 85.18 (2012): 184428.

[51] Schwickert, M. M., et al. "Magnetic moments, coupling, and interface interdiffusion in Fe/V (001) superlattices." *Physical Review B* 57.21 (1998): 13681.

[52] Yang, T., et al. "Polarization of Pd atoms in Ni/Pd magnetic multilayers." *Journal of Physics: Condensed Matter* 7.6 (1995): 1121.

[53] Van Lierop, J., et al. "Proximity effects in an exchange-biased Ni 80 Fe 20⁄Co 3 O 4 thin film." *Physical Review B* 75.13 (2007): 134409.

[54] Wang, Bo-Yao, et al. "Enhanced perpendicular magnetic anisotropy in Fe/Mn bilayers by incorporating ultrathin ferromagnetic underlayer through magnetic proximity effect." *Applied Physics Letters* 103.4 (2013): 042407.

[55] Sort, J., et al. "Using exchange bias to extend the temperature range of square loop behavior in [Pt⁄ Co] multilayers with perpendicular anisotropy." *Applied Physics Letters* 87.24 (2005): 242504.

[56] Frey, N. A., et al. "Magnetic anisotropy in epitaxial Cr O 2 and Cr O 2⁄ Cr 2 O 3 bilayer thin films." *Physical Review B* 74.2 (2006): 024420.

[57] Kandpal, Hem C., Gerhard H. Fecher, and Claudia Felser. "Calculated electronic and magnetic properties of the half-metallic, transition metal based Heusler compounds." *Journal of Physics D: Applied Physics* 40.6 (2007): 1507.

[58] Webster, P. J. "Magnetic and chemical order in Heusler alloys containing cobalt and manganese." *Journal of Physics and Chemistry of Solids* 32.6 (1971): 1221-1231.

[59] Ohno, Hideo. "Making nonmagnetic semiconductors ferromagnetic." *science* 281.5379 (1998): 951-956.

[60] Matsubara M, et al. Ultrafast optical tuning of ferromagnetism via the carrier density. Nature Commun. 6, 6724 (2015).

Chapter 2

Experimental Techniques

This chapter focuses on the experimental techniques utilized in my research project for the magneto-optical characterization of the magnetization dynamics in exchange-coupled ferromagnetic bilayer heterostructures. Both experimental setup and theoretical framework for the static magneto-optical Kerr effect (MOKE) and the time-resolved magneto-optical Kerr effect (TRMOKE) are discussed in detail in the following three sections.

Section 2.1 introduces the MOKE concept and its geometry for detecting the magnetization response under an external applied magnetic field. All three types of MOKE – polar MOKE, longitudinal MOKE and transversal MOKE – are discussed in this section. Section 2.2 describes the TRMOKE geometry which is usually used for measuring the magnetization dynamics in the ferromagnetic thin films. The magnetization precession and its mathematic derivations are discussed in this section as well. Section 2.3 presents the experimental setup for both MOKE and TRMOKE measurement.

2.1 Magneto-optical Kerr effect (MOKE)

The Kerr effect, also called the quadratic electro-optic effect, is a change in the refractive index of a material in response to an applied electric field, as was first discovered by John Kerr in 1875 [1]. In 1877, John Kerr reported a special case of the Kerr effect called magneto-optical Kerr effect (MOKE). The MOKE effect can be described by the microscopic quantum theory [2] or the macroscopic dielectric theory [3]. Considering linear-polarized light as a combination of left circular-polarized light and right circular-polarized light, the difference between the refraction indices of the two circular polarizations of the light induces the MOKE effect when the incident light gets reflected from a magnetized medium [4]: the difference between the real parts of the complex refraction indices gives rise to a rotation of the polarization plane of light, because left- and right-circular polarized light have different propagation speeds which causes a phase-shift when the light is propagating through the magnetized medium. The difference between the imaginary parts of the complex refraction indices leads to the different absorption rates for the two circular polarizations of the light and thus causes an elliptical polarization of the light propagating in the magnetic material. In short, the polarization state of the incident light is expected to undergo a change depending on the state of the local magnetization, leading to a modification of ellipticity [5].

In the microscopic quantum theory of the magneto-optic effect, light induces a potential gradient ∇V which interacts with local electron spins s with momentum p through spin-orbit coupling inside the medium, leading to an interaction term $(\nabla V \times p) \cdot s$ that connects the magnetic and optical properties of the magnetized medium. In the macroscopic picture, MOKE is described by the asymmetric off-diagonal components in the dielectric tensor which are determined by the state of the local magnetization in the magnetized medium:

$$\vec{\varepsilon} = \varepsilon_0 \begin{pmatrix} 1 & iQ_z & -iQ_y \\ -iQ_z & 1 & iQ_x \\ iQ_y & -iQ_x & 1 \end{pmatrix}, \tag{2.1.1}$$

where ε_0 is the average dielectric constant, and $\vec{Q} = (Q_x, Q_y, Q_z)$ is the Voigt vector. Here, $n = \sqrt{\varepsilon}$ is the average refraction index, $n_L = n\left(1 - \frac{\vec{Q}\cdot\vec{k}}{2}\right)$ and $n_R = n\left(1 + \frac{\vec{Q}\cdot\vec{k}}{2}\right)$ are the refraction indexes for left- and right-circular polarized light, respectively, and $\vec{k}$ is the unit vector along the light propagation direction [3]. If the light propagates through the magnetized medium by a distance L, the rotation of the polarization plane of light is given by

$$\varphi = \frac{\pi L}{\lambda} Re(n_L - n_R) = -\frac{\pi L}{\lambda} Re\left(\vec{Q} \cdot \vec{k}\right), \tag{2.1.2}$$

where λ is the wavelength in vacuum.

MOKE can be categorized into three different modes: polar MOKE, longitudinal MOKE and transverse MOKE, based on the geometry of the direction of magnetization $\overrightarrow{\boldsymbol{M}}$ in relation to the plane of the incident beam and the sample surface, as depicted in Fig. 2.1. (i) Polar MOKE is usually observed with normal incident beam when the direction of magnetization is perpendicular to the sample surface. (ii) Longitudinal MOKE is examined when the direction of magnetization is parallel to both the plane of incident beam and the sample surface. (iii) Transverse MOKE represents the case when the magnetization vector is parallel to the plane of sample surface but perpendicular to the plane of incident beam.

Since MOKE is defined according to the geometry of magnetization with respect to the incident plane and the sample surface, the direction of polarization of the beam must be taken into account in the MOKE measurements. In the convenient decomposition scheme, the incident or reflected beam is considered as a combination of p-polarized light (linear polarized light with the polarization direction parallel to the incident plane) and s-polarized light (linear polarized light with the polarization direction perpendicular to the incident plane). Thus, MOKE can be represented by:

$$\begin{pmatrix} \boldsymbol{E_s^{out}} \\ \boldsymbol{E_p^{out}} \end{pmatrix} = \boldsymbol{r} \begin{pmatrix} \boldsymbol{E_s^{in}} \\ \boldsymbol{E_p^{in}} \end{pmatrix}, \tag{2.1.3}$$

where $\boldsymbol{E_s^{in}}$ and $\boldsymbol{E_p^{in}}$ denote the s-polarized and p-polarized components of the incident beam, $\boldsymbol{E_s^{out}}$ and $\boldsymbol{E_p^{out}}$ represent the s-polarized and p-polarized components of the reflected beam. $\boldsymbol{r} = \begin{pmatrix} \boldsymbol{r_{ss}} & \boldsymbol{r_{sp}} \\ \boldsymbol{r_{ps}} & \boldsymbol{r_{pp}} \end{pmatrix}$ is the scattering matrix with four Fresnel coefficients that describe the reflection mechanism for all three types of MOKE, as summarized in Table 2.1 for p-polarized incident light [6]. We can see the MOKE strongly depends on the magnetization geometry. The longitudinal and polar components of $\vec{\boldsymbol{M}}$ lie in the plane of the incident beam. They are expected to rotate the polarization plane and introduce ellipticity upon reflection. In contrast, the transverse component lies along the direction perpendicular to the incident plane and thus changes only the intensity of the beam but has no effect on its polarization.

According to the magnetization geometry discussed above, the detection of MOKE requires different setups for the three different modes, i.e., the combination of the set polarization angles of the polarizer and analyzer determines which component will be measured. In general, the incident beam is p-polarized light. For the longitudinal or the polar geometry, the angle of analyzer is set normal to the incident plane, because the detection of s-polarization change is sensitive to the in-plane component of magnetization. For the transverse MOKE, the angle of analyzer should be set parallel to the incident plane so that the out-of-plane

component can be detected. The detailed experimental setup is given in Section 2.3.

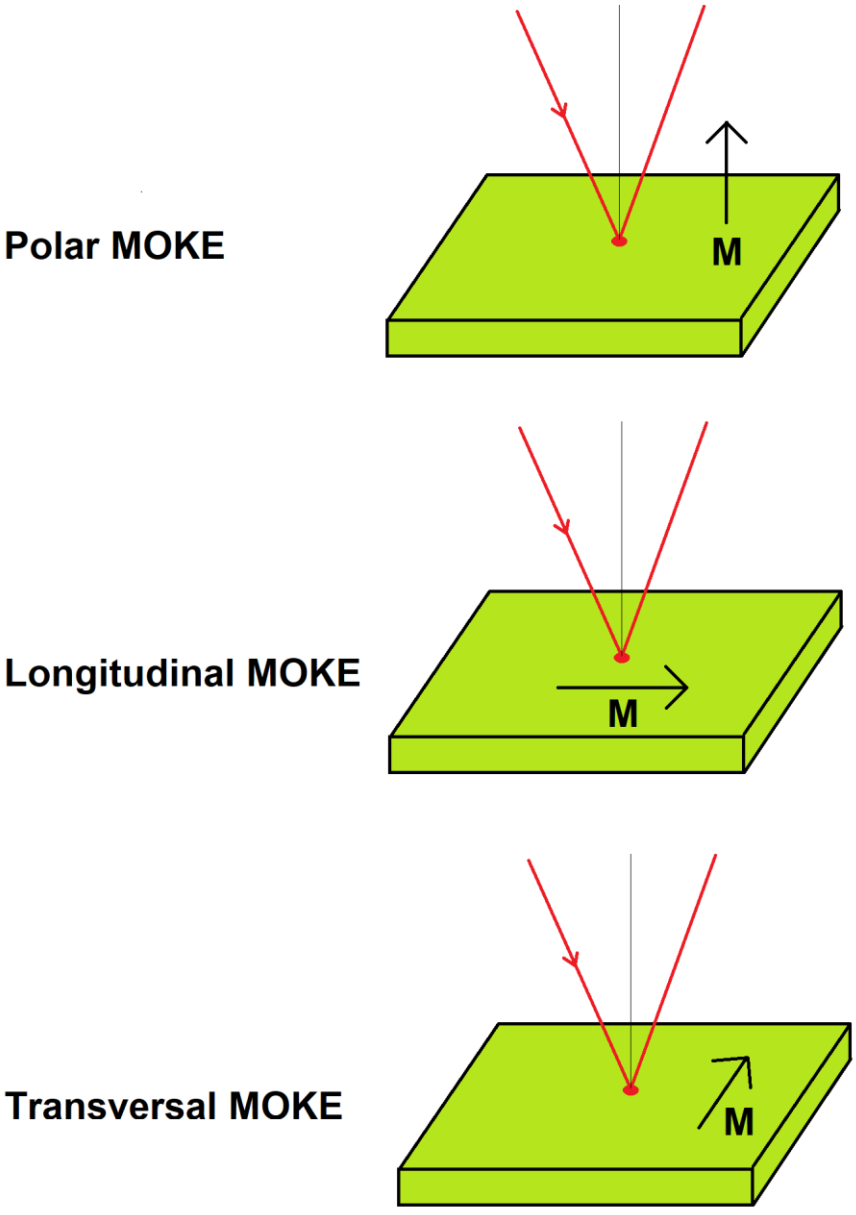

Figure 2.1 Schematics of polar, longitudinal and transverse MOKE. ***M*** denotes the direction of local magnetization.

Table 2.1: The Fresnel coefficients for p-polarized light incident on a magnetic medium. $\boldsymbol{\theta_1}$, $\boldsymbol{\theta_2}$ represent the incident angle and the refracted angle in the magnetic layer, respectively. The Voigt coefficients $\boldsymbol{Q_P}$, $\boldsymbol{Q_L}$, and $\boldsymbol{Q_T}$ denote the polar, longitudinal and transverse projection of the Voigt vector $\vec{\boldsymbol{Q}}$, respectively, which are proportional to the magnetization components along the corresponding directions [6].

	$\boldsymbol{r_{pp}}$	$\boldsymbol{r_{ps}}$
Polar	$\frac{\sqrt{\varepsilon}cos\theta_1 - cos\theta_2}{\sqrt{\varepsilon}cos\theta_1 + cos\theta_2}$	$\frac{Q_P\sqrt{\varepsilon}cos\theta_1}{i(\sqrt{\varepsilon}cos\theta_1 + cos\theta_2)(cos\theta_1 + \sqrt{\varepsilon}cos\theta_2)}$
Longitudinal	$\frac{\sqrt{\varepsilon}cos\theta_1 - cos\theta_2}{\sqrt{\varepsilon}cos\theta_1 + cos\theta_2}$	$\frac{Q_L\sqrt{\varepsilon}cos\theta_1 tan\theta_1}{i(\sqrt{\varepsilon}cos\theta_1 + cos\theta_2)(cos\theta_1 + \sqrt{\varepsilon}cos\theta_2)}$
Transverse	$\frac{\sqrt{\varepsilon}cos\theta_1\sqrt{1 - Q_T^2/cos^2\theta_2} - cos\theta_2 - i\sqrt{\varepsilon}Q_T cos\theta_1 tan\theta_2}{\sqrt{\varepsilon}cos\theta_1\sqrt{1 - Q_T^2/cos^2\theta_2} + cos\theta_2 - i\sqrt{\varepsilon}Q_T cos\theta_1 tan\theta_2}$	**0**

Figure 2.2 presents the MOKE measurement in the Co_2FeAl/(Ga,Mn)As bilayer sample at room temperature (300 K). The incident beam is set to be p-polarized while the s-component of the reflected beam is measured by the photodetector, indicating the longitudinal component is detected in the experiment. The external magnetic field is applied along the intermediate axis [100].

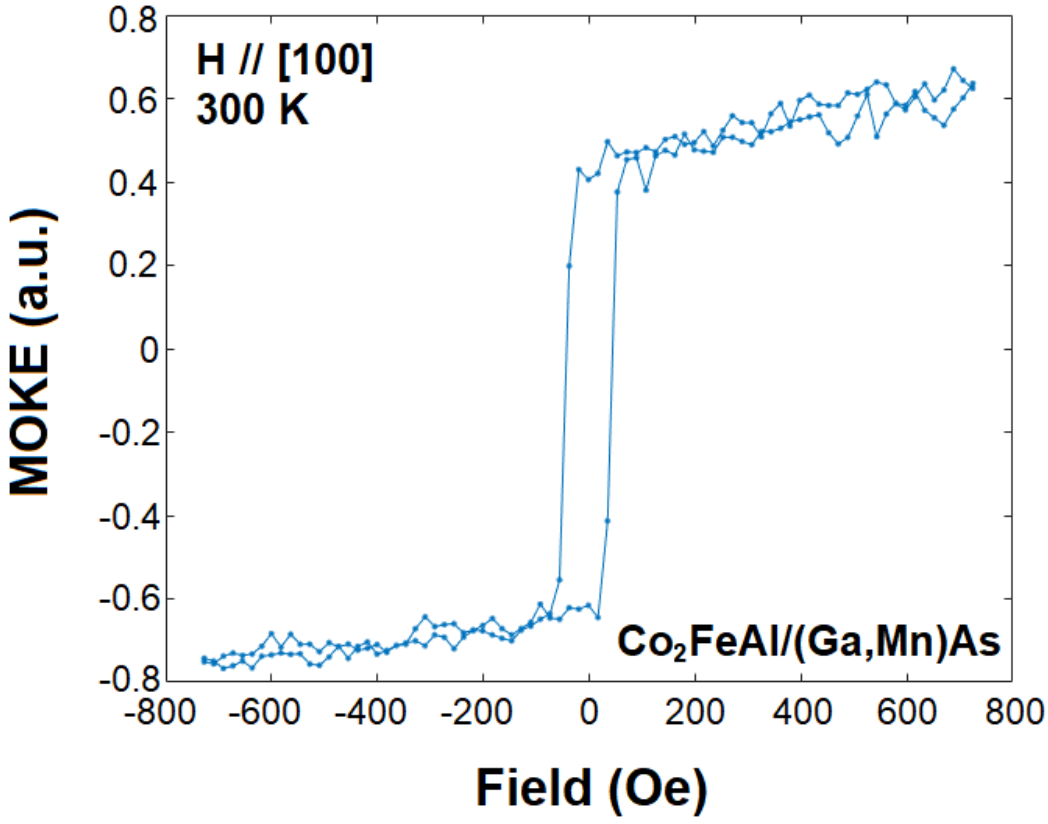

Figure 2.2 MOKE measurement in Co_2FeAl/(Ga,Mn)As sample at room temperature

2.2 Time-resolved Magneto-optical Kerr effect (TRMOKE)

Unlike MOKE or MSHG which looks into the static magnetic response, time-resolved magneto-optical Kerr effect (TRMOKE) provides a reliable path to detect the ultrafast magnetization dynamics of a magnetic medium in the time domain, which was introduced in 1991 [15].

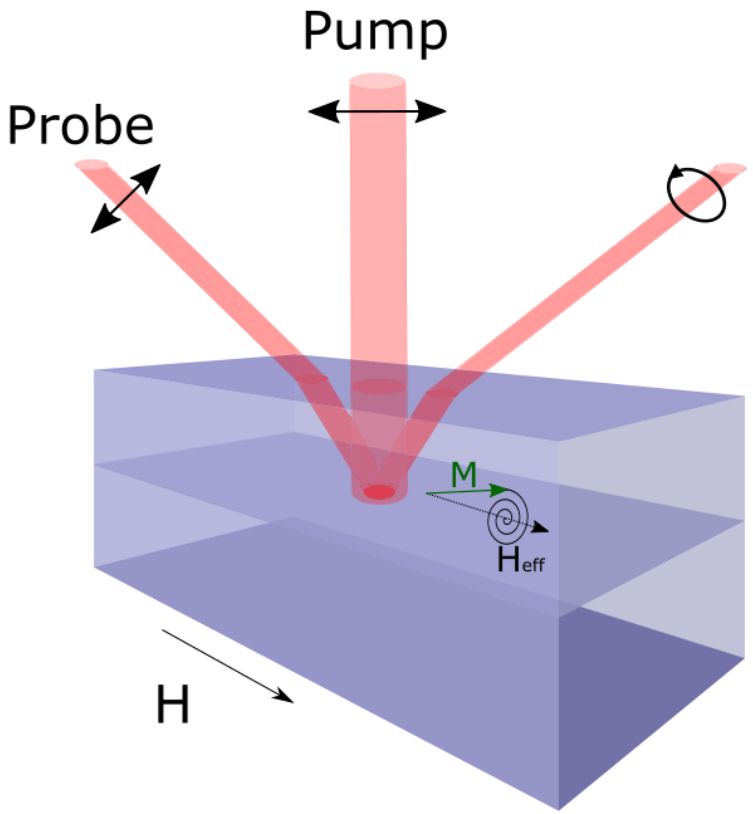

Figure 2.3 Schematic of TRMOKE measurement setup

The TRMOKE measurement (Fig. 2.3) is usually performed with the pump-probe technique: an intense laser pulse is utilized to initiate the magnetization precession while a comparably weak linear-polarized beam

of light is used to measure the magnetization dynamics with the MOKE technique. With the pump-probe setup, a real-time trace of Kerr rotation can be obtained by controlling the delay time between the pump beam and the probe beam.

2.2.1 Laser-induced Magnetization Precession

In the exchange-coupled ferromagnetic bilayer system, the magnetization precession can be triggered by photoexcitation, as shown in Figure 2.4. In equilibrium, the magnetization $\vec{\boldsymbol{M}}$ is along an effective field $\boldsymbol{H_{eff}}$, which is the sum of external magnetic field, the demagnetizing field, the anisotropy fields, and the exchange-coupling field. In the case of my measurements, the effective field $\boldsymbol{H_{eff}}$ lies in the plane of the sample surface. At $\boldsymbol{\Delta t}$ = 0 ps, the linear-polarized incident pump pulses arrive at the surface of the sample, exciting the electrons within a few picoseconds. The ultrafast photo-excitation destroys the previous equilibrium, changing the effective field from $\boldsymbol{H_{eff}}$ to $\boldsymbol{H'_{eff}}$. The transient effective field $\boldsymbol{H'_{eff}}$ creates a strong dynamic spin torque $\boldsymbol{\tau}(\Delta t)$ on the current magnetization $\vec{\boldsymbol{M}}$ to align it along a new equilibrium direction. At $\boldsymbol{\Delta t}$ > 0 ps, $\vec{\boldsymbol{M}}$ precesses along the transient effective field. After tens of picoseconds ($\boldsymbol{\Delta t}$ >> 0 ps), due to carrier recombination and heat diffusion, the effective field returns to the previous equilibrium direction. Although $\boldsymbol{\tau}(\boldsymbol{\Delta t})$ has vanished, $\vec{\boldsymbol{M}}$ has

been “pulled” away from its original direction. As a consequence, $\vec{M}$ starts to precess along H_{eff} in a damped circling way.

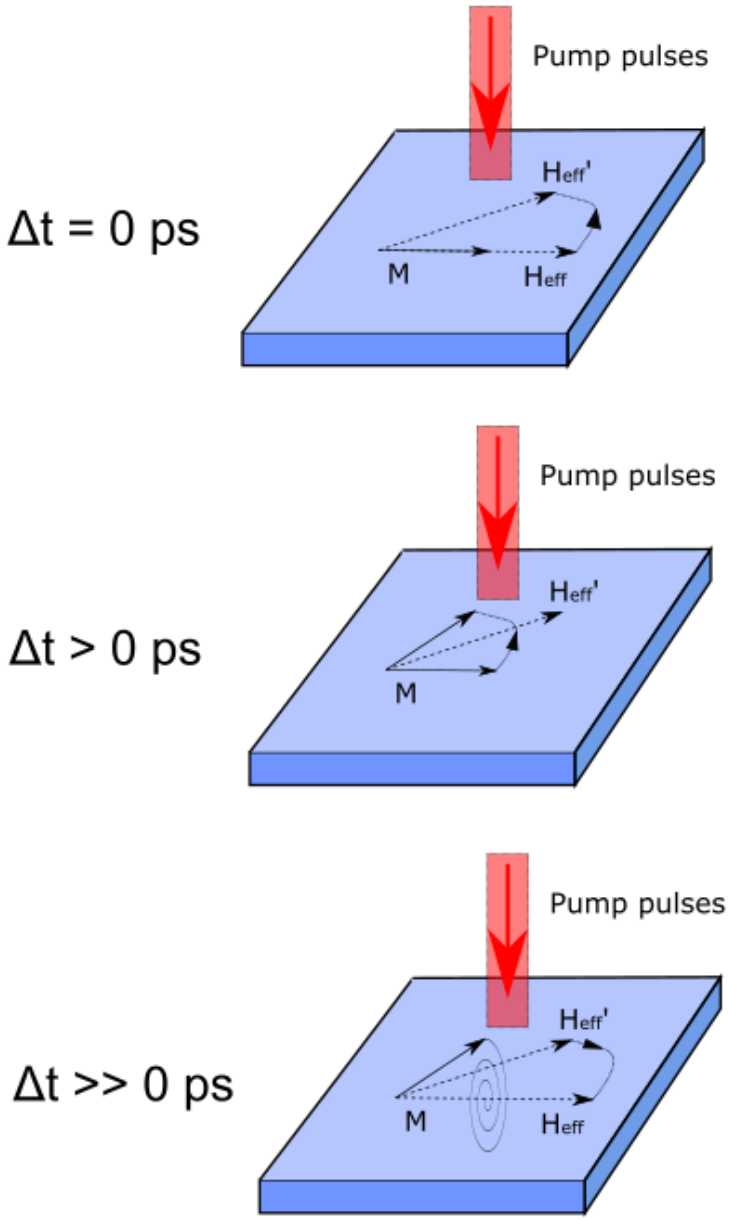

Figure 2.4 Schematic diagrams of the photo-excitation process of the magnetization precession.

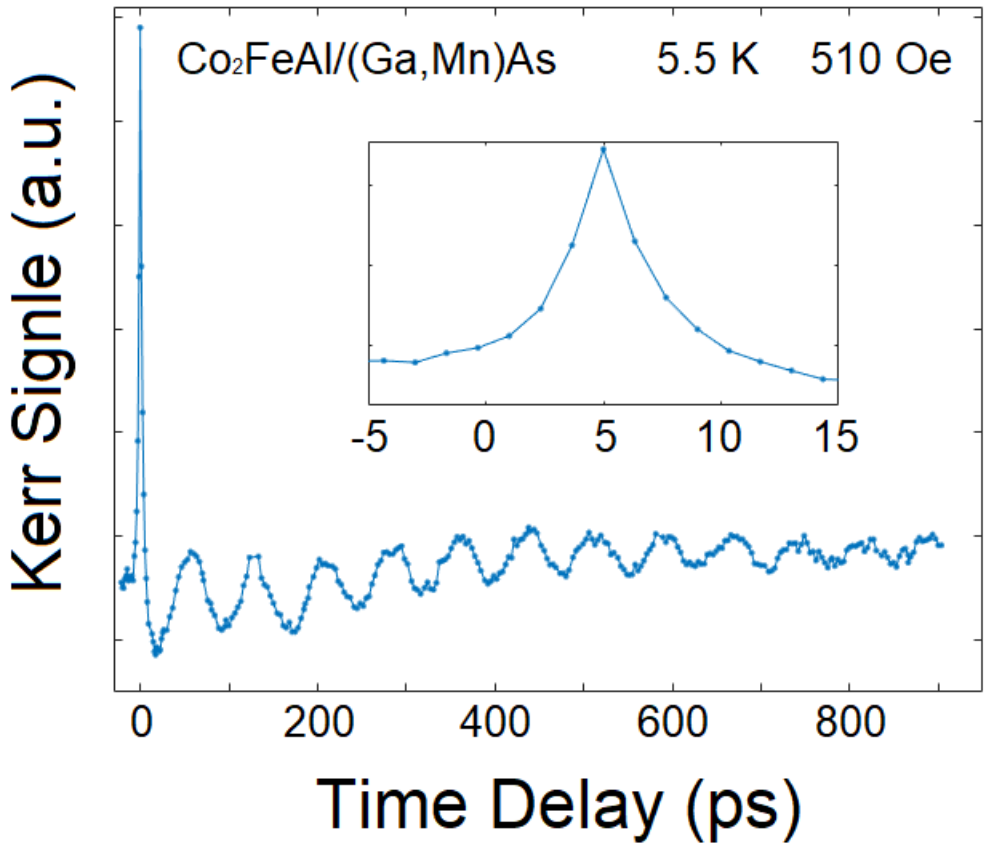

Figure 2.5 TRMOKE measurement on the Co_2FeAl/(Ga,Mn)As bilayer at 5.5 K with applying external magnetic field of 510 Oe along [100] direction. The inset shows the close-up around 0 ps.

Figure 2.5 displays the TRMOKE signal measured on the Co_2FeAl/(Ga,Mn)As bilayer at 5.5 K under magnetic field of 510 Oe. The incident beam of light is p-polarized, while the reflected beam of light passes through an s-polarized analyzer before entering the photodetector. A clear picture of magnetization motion under pump-pulse excitation can be presented. The close-up inset shows the Kerr signal around 0 ps.

Before $\boldsymbol{\Delta t}$ = 5 ps, the pump beam excites the electrons which then relax through phonon-assisted spin-flip scattering. The increasing temperature of spins leads to a large and rapid demagnetization, which represents the first process shown in Fig. 2.4. The recovery process occurs at 5 ps < $\boldsymbol{\Delta t}$ < 15 ps, corresponding to the second process in Fig. 2.4. The third process starts after 15 ps when the magnetization precesses with damped circular motion towards the previous equilibrium direction.

2.2.2 Precession Frequency and Effective Gilbert Damping

Landau and Lifshitz modeled in 1935 for the first time the magnetization precession with a modified continuum precession equation, which is called the Landau-Lifshitz equation:

$$\frac{\partial \boldsymbol{M}}{\partial \boldsymbol{t}} = -\boldsymbol{\gamma}\left(\boldsymbol{M} \times \boldsymbol{H}_{\boldsymbol{eff}}\right), \tag{2.2.1}$$

where $\gamma = \frac{g\mu_B}{\hbar}$ is the gyromagnetic ratio. The effective field $\boldsymbol{H}_{\boldsymbol{eff}}$ is the sum of external magnetic field, the demagnetizing field, the anisotropy fields, and the exchange-coupling field. This equation describes the precession motion of the magnetization around the equilibrium direction under the torque induced by the effective field $\boldsymbol{H}_{\boldsymbol{eff}}$. However, it does not include the dissipative process accompanying the magnetization precession. In 1955, Gilbert [16] introduced a kind of “viscous” torque whose components are

proportional to the time derivatives of the generalized coordinates: $\boldsymbol{\alpha M \times \frac{\partial M}{\partial t}}$, where $\boldsymbol{\alpha} > 0$ is the dimensionless Gilbert damping constant [17]. This term describes the damping of the magnetization oscillation which arises from exchanging magnetic energy and angular momentum with the environment.

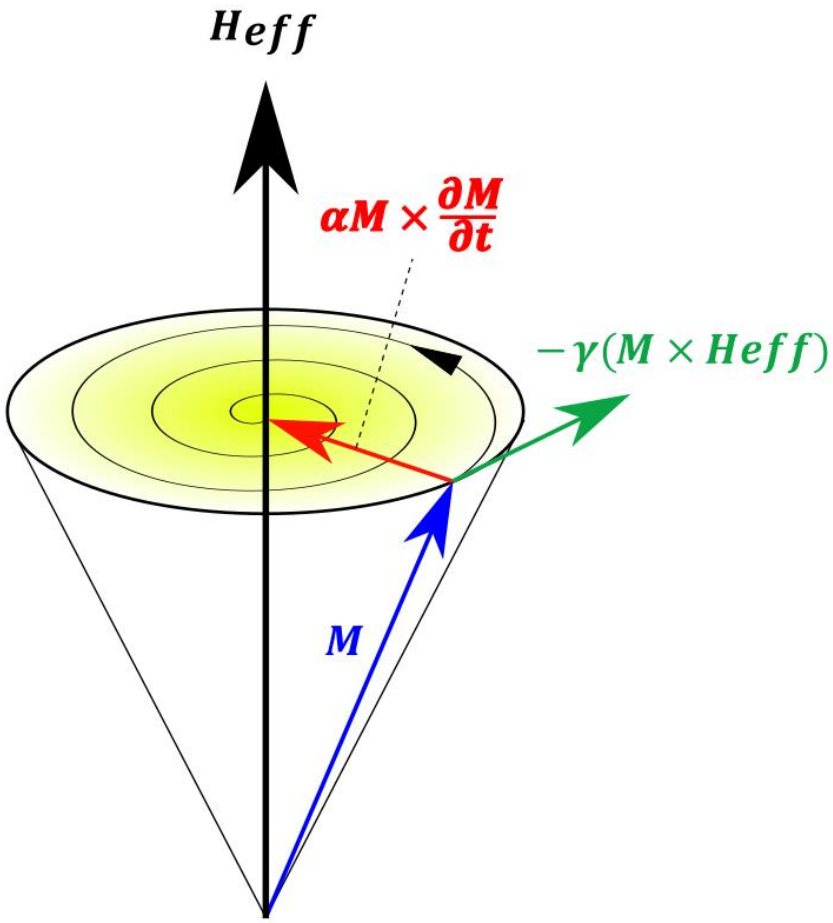

Figure 2.6 Schematic of ultrafast magnetization precession modeled by Landau-Lifshitz-Gilbert equation

With the modification according to Gilbert's work, the ultrafast magnetization precession can be described by the Landau-Lifshitz-Gilbert (LLG) equation:

$$\frac{\partial \boldsymbol{M}}{\partial \boldsymbol{t}} = -\boldsymbol{\gamma}\left(\boldsymbol{M} \times \boldsymbol{H}_{\boldsymbol{eff}}\right) + \boldsymbol{\alpha M} \times \frac{\partial \boldsymbol{M}}{\partial \boldsymbol{t}}, \tag{2.2.2}$$

as seen in Fig. 2.6.

In general, the oscillation frequency of the magnetization precession can be derived from LLG equation with the following steps if the angle of the precession is small. First, the equation for the magnetization precession can be derived by describing the torques induced by the effective field $\boldsymbol{H}_{\boldsymbol{eff}}$ that act on the magnetization. Second, we need to find the equilibrium direction of magnetization which is determined by the effective field $\boldsymbol{H}_{\boldsymbol{eff}}$. Finally, with the help of Maxwell's equations and boundary conditions, the linearized equations of motion can be solved to derive the oscillation frequency of the magnetization precession.

Considering a coordinate system with the *x* axis along the equilibrium direction, then according to the LLG equation (Eq. (2.2.2)) the motion of the magnetization precession can be expressed by:

$$\frac{\boldsymbol{dm_x}}{\boldsymbol{dt}}\vec{\boldsymbol{x}} + \frac{\boldsymbol{dm_y}}{\boldsymbol{dt}}\vec{\boldsymbol{y}} + \frac{\boldsymbol{dm_z}}{\boldsymbol{dt}}\vec{\boldsymbol{z}} = -\boldsymbol{\gamma}\begin{bmatrix} \vec{\boldsymbol{x}} & \vec{\boldsymbol{y}} & \vec{\boldsymbol{z}} \\ \boldsymbol{m_x} + \boldsymbol{M_s} & \boldsymbol{m_y} & \boldsymbol{m_z} \\ \boldsymbol{H_x} & \boldsymbol{H_y} & \boldsymbol{H_z} \end{bmatrix}, \tag{2.2.3}$$

where $\boldsymbol{m_x}$, $\boldsymbol{m_y}$ and $\boldsymbol{m_z}$ represent the projection of the magnetization $\vec{\boldsymbol{M}}$ on x-axis, y-axis and z-axis, respectively. $\boldsymbol{H_x}$, $\boldsymbol{H_y}$ and $\boldsymbol{H_z}$ denote the projection

of the effective field $\overrightarrow{\boldsymbol{H_{eff}}}$ on x, y and z-axis, respectively. $\boldsymbol{M_s}$ is the saturation magnetization.

Figure 2.7 depicts a ferromagnetic thin film with the easy axis along [110] direction, which is under pump-pulse excitation with applied external magnetic field $\boldsymbol{H}$. The magnetization is expected to precess along the in-plane equilibrium direction with the free energy represented by:

$$\boldsymbol{F = -M_s H cos(\varphi_M - \varphi_H) + K_u sin^2 \varphi_M + \frac{K_1}{4} sin^2(2\varphi_M)}$$

$$\boldsymbol{+(2\pi M_s^2 + K_\perp) sin^2 \varphi_\perp}, \qquad (2.2.4)$$

where $\boldsymbol{\varphi_M}$ denotes the equilibrium angle of the magnetization vector with respect to the easy axis [110] direction, $\boldsymbol{\varphi_H}$ is the angle between external field and [110] axis, $\boldsymbol{\varphi_\perp}$ represents the angle of the magnetization vector with respect to the sample plane, $\boldsymbol{K_u}$ is the in-plane uniaxial anisotropy constant and $\boldsymbol{K_1}$ is the in-plane cubic anisotropy field. Since the angle of magnetization precession is considered small, $\boldsymbol{cos\theta}$ is very close to 1. In Eq. (2.2.4), the first term $\boldsymbol{-M_s H cos(\varphi_M - \varphi_H)}$ represents the contribution of Zeeman energy density, the second term $\boldsymbol{K_u sin^2 \varphi_M}$ denotes the uniaxial anisotropy energy density, the third term $\boldsymbol{\frac{K_1}{4} sin^2(2\varphi_M)}$ is the cubic anisotropy energy density, and the fourth term $\boldsymbol{(2\pi M_s^2 + K_\perp) sin^2 \varphi_\perp}$ is the sum of the demagnetization energy density and the perpendicular anisotropy energy density.

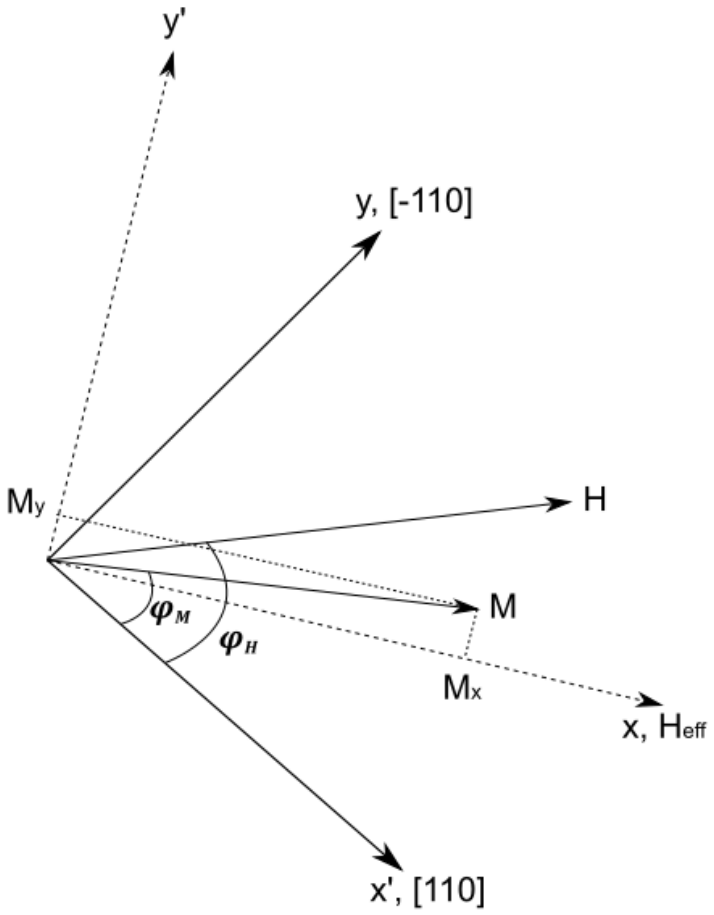

Figure 2.7 Coordinate system for solving LLG equation. $\boldsymbol{M_x}$ and $\boldsymbol{M_y}$ is projection of magnetization $\vec{\boldsymbol{M}}$ onto x- and y-axis, respectively. $\boldsymbol{\varphi_M}$ denotes equilibrium angle of magnetization vector with respect to easy axis [110] direction, $\boldsymbol{\varphi_H}$ is angle between external field and [110] axis.

Since spins tend to rotate to the direction of lower energy state, the equilibrium axis aligns along the direction of the energy minimum. In order

to determine the equilibrium direction, we need to take the derivative of the free energy F over φ_M, which turns out to be:

$$M_s H sin(\varphi_M - \varphi_H) + K_u sin(2\varphi_M) + \frac{K_1}{2} sin(4\varphi_M) = 0,$$

The magnetization precession is driven by a torque induced by the effective field $\overrightarrow{H_{eff}} = H_x\vec{x} + H_y\vec{y} + H_z\vec{z}$, which is represented by:

$$H_x = -\frac{dF}{dm_x} + \cos(\varphi_M - \varphi_H)$$

$$H_y = -\frac{dF}{dm_y} - \sin(\varphi_M - \varphi_H) \quad (2.2.6)$$

$$H_z = -\frac{dF}{dm_z}.$$

In order to solve the equation of motion (Eq. 2.2.3), we need to transfer the expression of the free energy F into the coordinate system with x-axis along the equilibrium direction (Fig. 2.7). We have $\cos\varphi_M = \frac{M_x'}{M_s}$, $\sin\varphi_M = \frac{M_y'}{M_s}$ and $\sin\varphi_\perp = \frac{M_z'}{M_s}$, where M_x', M_y' and M_z' are the projections of the magnetization $\overrightarrow{M}$ on [110] direction and [-110] direction, respectively. According to the coordinate transformation, which is $M_x' \rightarrow (M_x cos\varphi_M - M_y sin\varphi_M)$, $M_y' \rightarrow (M_x sin\varphi_M + M_y cos\varphi_M)$ and $M_z' \rightarrow M_z$, the magnetic free energy can be represented by:

$$F = K_u \frac{(M_x sin\varphi_M + M_y cos\varphi_M)^2}{M_s^2}$$

$$+K_1\frac{(M_x cos\varphi_M - M_y sin\varphi_M)^2 \times (M_x sin\varphi_M + M_y cos\varphi_M)^2}{M_s^4}$$

$$+2\pi M_z^2 + K_\perp \frac{M_z^2}{M_s^2} \quad (2.2.7)$$

By substituting Eq. (2.2.7) into Eq. (2.2.6), the expression of the effective field can be derived:

$$H_x = -\frac{2K_u}{M_s} sin^2\varphi_M - \frac{K_1}{M_s} sin^2(2\varphi_M) + Hcos(\varphi_M - \varphi_H)$$

$$H_y = -\frac{K_u}{M_s} sin(2\varphi_M) - \frac{K_1}{2M_s} sin(4\varphi_M) - Hsin(\varphi_M - \varphi_H) \quad (2.2.8)$$

$$H_x = -4\pi M_z - \frac{2K_\perp M_z}{M_s^2} .$$

Therefore, the torque equations are:

$$\frac{dm_y}{dt} = -\gamma[Hcos(\varphi_M - \varphi_H) - \frac{2K_u}{M_s} sin^2\varphi_M - \frac{K_1}{M_s} sin^2(2\varphi_M)$$

$$+4\pi M_s + \frac{2K_\perp}{M_s}]m_z \quad (2.2.9)$$

$$\frac{dm_z}{dt} = -\gamma[-Hcos(\varphi_M - \varphi_H) - \frac{2K_u}{M_s} cos(2\varphi_M) - \frac{2K_1}{M_s} cos(4\varphi_M)]m_y.$$

Considering the uniform oscillation, the usual ansatz can be applied to solve the torque equations (Eq. (2.2.9)):

$$m_y = m_{y0} e^{i\omega t + \varphi_y}$$

$$m_z = m_{z0} e^{i\omega t + \varphi_z}. \quad (2.2.10)$$

By substituting Eq. (2.2.10) into Eq. (2.2.9), we can easily derive the expression of the spin precession frequency $\boldsymbol{f}$:

$$\boldsymbol{f} = \frac{\boldsymbol{\gamma}}{\boldsymbol{2\pi}}(\boldsymbol{H_a} \cdot \boldsymbol{H_b})^{\frac{1}{2}}, \tag{2.2.11}$$

where

$$\boldsymbol{H_a} = \boldsymbol{H}\boldsymbol{cos}(\boldsymbol{\varphi_M} - \boldsymbol{\varphi_H}) + \boldsymbol{H_u}\boldsymbol{cos}(\boldsymbol{2\varphi_M}) + \boldsymbol{H_1}\boldsymbol{cos}(\boldsymbol{4\varphi_M})$$

$$\boldsymbol{H_b} = \boldsymbol{H}\boldsymbol{cos}(\boldsymbol{\varphi_M} - \boldsymbol{\varphi_H}) + \boldsymbol{4\pi M_{eff}} - \boldsymbol{H_u}\boldsymbol{sin^2\varphi_M} + \frac{\boldsymbol{H_1}}{\boldsymbol{4}}\big(\boldsymbol{3} + \boldsymbol{cos}(\boldsymbol{4\varphi_M})\big).$$

Here $\boldsymbol{H_u} = \frac{\boldsymbol{2K_u}}{\boldsymbol{M_s}}$ denotes the uniaxial anisotropy field, $\boldsymbol{H_1} = \frac{\boldsymbol{2K_1}}{\boldsymbol{M_s}}$ represents the cubic anisotropy field and $\boldsymbol{M_{eff}} = \boldsymbol{M_s} + \frac{\boldsymbol{K_\perp}}{\boldsymbol{2\pi M_s}}$ is the effective magnetization of the sample.

Note that Eq. (2.2.6) comes from the first term in the LLG equation (Eq. (2.2.2)) which describes the motion of the magnetization. In order to examine the decay behavior of the magnetization precession, we need to consider the second term in LLG equation. The effective Gilbert damping is calculated from the external applied magnetic field, the anisotropy fields and the lifetime of the spin waves, using

$$\boldsymbol{\alpha} = \boldsymbol{2}/[\boldsymbol{\tau\gamma}(\boldsymbol{2H}\boldsymbol{cos}(\boldsymbol{\varphi_M} - \boldsymbol{\varphi_H}) + \boldsymbol{H_a} + \boldsymbol{H_b})], \tag{2.2.12}$$

where $\boldsymbol{\tau}$ represents the lifetime of the magnetization precession and can be obtained by fitting the TRMOKE signal.

The derivation given above provides a general procedure to deduce the frequency and damping parameter of the magnetization precession. The real situation may be more complicated so that sometimes we need to use a modified LLG equation with extended magnetic free energy to describe the magnetization precession, as shown in Chapter 3.

2.3 Experimental Setup

The experimental setup for MOKE in this dissertation is based on the magnetization geometry (Fig. 2.1) discussed in Section 2.1, as shown in Fig. 2.8. The laser light is provided by a Ti:sapphire oscillator laser system, which produces 150-ps pulses at 800 nm wavelength with a repetition rate of 80 MHz. The detection of MOKE is usually performed as follows: a laser beam first passes through a linear polarizer with polarization angle set to 0° in relation to the incident plane and then the beam is modulated by a chopper before hitting the sample surface. The incident angle of the probe beam is set to 45°. After reflected from the sample surface, the beam is directed to pass through an analyzer and finally reach the photodetector. The set angle of the analyzer depends on which component of the magnetization is to be measured. For the longitudinal or the polar geometry, the angle of analyzer is set to nearly 90°

in relation to the incident plane in order to detect the change of s-polarization. For the transverse MOKE, the angle of analyzer should be set to 0° so that the out-of-plane polarization component can be detected. An external magnetic field generated by a superconducting magnet is applied along the in-plane direction of the sample during measurement.

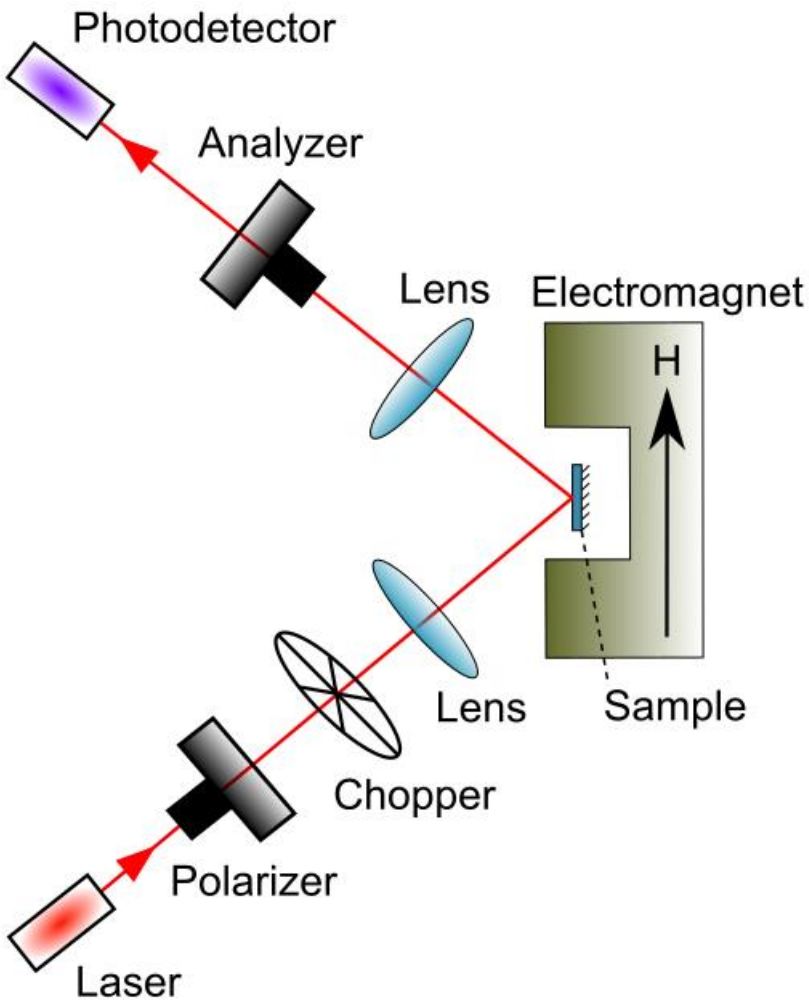

Figure 2.8 Sketch of experiment setup for MOKE

The experimental setup for TRMOKE in this dissertation is designed based on the pump-probe setup (Fig. 2.3), as shown in Fig. 2.9. The output laser light is split into a pump beam and a probe beam through a beam splitter with different power density. The probe fluence is fixed at ~0.5 $\mu J/cm^2$ and the pump fluence varies from 0.5-100 $\mu J/cm^2$. A delay line is placed in the pump beam path in order to control the time delay between the pump beam and the probe beam. The pump beam is modulated by a chopper and is focused to a spot with diameter of 0.468 mm on the sample surface as photoexcitation source. The incident angle of pump beam is set to 89° in order to avoid double reflection that may induce more noise for probe detection. The probe beam is directed to pass through a linear polarizer with polarization angle set to 0° in relation to the incident plane and then it is incident on the same spot on the sample surface as the pump beam. The incident angle of the probe beam is set to 45°. After reflection from the sample surface, the probe beam is directed to pass through an analyzer with polarization angle set to nearly 90° in relation to the incident plane. A photodetector is utilized for detecting the probe beam to investigate the transient change of magnetic state along the longitudinal and polar directions. An external magnetic field generated by the superconducting magnet is applied along the in-plane direction of the sample during experiment.

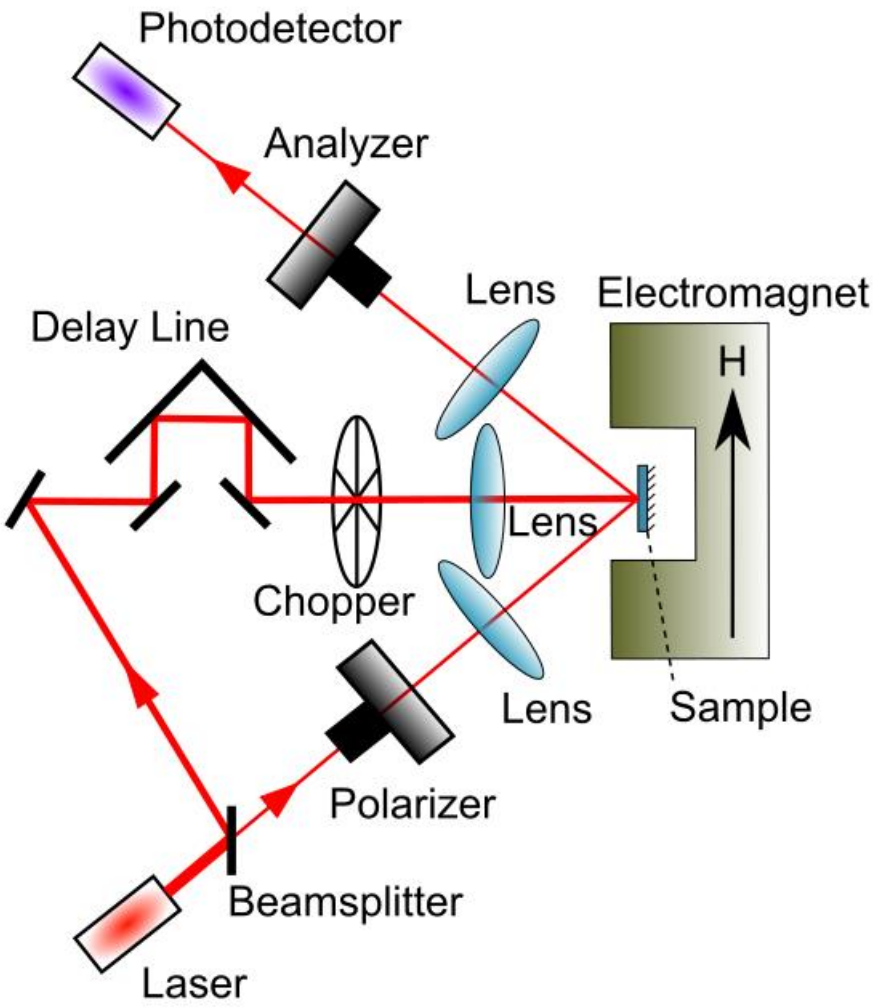

Figure 2.9 Sketch of experiment setup for TRMOKE

References:

[1] Kerr, John. "XL. A new relation between electricity and light: Dielectrified media birefringent." *The London, Edinburgh, and Dublin Philosophical Magazine and Journal of Science* 50.332 (1875): 337-348.

[2] Lifshĭts, Evgeniĭ Mikhaĭlovich. *Electrodynamics of continuous media*. Vol. 8. Pergamon Press, 1960.

[3] Qiu, Z. Q. "ZQ Qiu and SD Bader, Rev. Sci. Instrum. 71, 1243 (2000)." *Rev. Sci. Instrum.* 71 (2000): 1243.

[4] J. C. Maxwell, Electricity and Magnetism 2, Chap. 21 (1873).

[5] https://en.wikipedia.org/wiki/Magneto-optic_Kerr_effect

[6] Daboo, C., et al. "Vectorial magnetometry with the magneto-optic Kerr effect applied to Co/Cu/Co trilayer structures." *Physical Review B* 47.18 (1993): 11852.

[7] Kirilyuk, Andrei, and Theo Rasing. "Magnetization-induced Second Harmonic Generation." *Handbook of magnetism and advanced magnetic Materials* (2007).

[8] Reif, J., et al. "Effects of surface magnetism on optical second harmonic generation." *Physical review letters* 67.20 (1991): 2878.

[9] Reif, J., C. Rau, and E. Matthias. "Influence of magnetism on second harmonic generation." *Physical review letters* 71.12 (1993): 1931.

[10] Bennemann, Karl Heinz, ed. *Non-linear optics in metals*. No. 98. Oxford University Press, 1998.

[11] Rasing, Th. "Nonlinear magneto-optics." *Journal of magnetism and magnetic materials* 175.1-2 (1997): 35-50.

[12] Lüpke, Gunter. "Characterization of semiconductor interfaces by second-harmonic generation." *Surface Science Reports*35.3-4 (1999): 75-161.

[13] Shen, Yuen-Ron. "The principles of nonlinear optics." *New York, Wiley-Interscience, 1984, 575 p.* (1984).

[14] W. G. Rado, The nonlinear third order dielectric susceptibility coefficients of gases and optical third harmonic generation, *Applied Physics Letters* (Volume:11 , Issue: 4) 123 - 125, 1967

[15] Freeman, M. R., R. R. Ruf, and R. J. Gambino. "Picosecond pulsed magnetic fields for studies of ultrafast magnetic phenomena." *IEEE transactions on magnetics* 27.6 (1991): 4840-4842.

[16] Gilbert, Thomas L. "A Lagrangian formulation of the gyromagnetic equation of the magnetization field." *Phys. Rev.*100 (1955): 1243.

[17] http://wpage.unina.it/mdaquino/PhD_thesis/main/node29.html

[18] Grünberg, P. E. T. E. R., et al. "Layered magnetic structures: Evidence for antiferromagnetic coupling of Fe layers across Cr interlayers." *Physical review letters* 57.19 (1986): 2442.

[19] Majkrzak, C. F., et al. "Observation of a magnetic antiphase domain structure with long-range order in a synthetic Gd-Y superlattice." *Physical review letters* 56.25 (1986): 2700.

[20] Salamon, M. B., et al. "Long-range incommensurate magnetic order in a Dy-Y multilayer." *Physical review letters* 56.3 (1986): 259.

Chapter 3

High-efficiency Excitation in Co_2FeAl/(Ga,Mn)As

Fast spin manipulation in magnetic heterostructures, where magnetic interactions between different materials often define the functionality of devices, is a key issue in the development of ultrafast spintronics. Although recently developed optical approaches such as ultrafast spin-transfer and spin-orbit torques open new pathways to fast spin manipulation, these processes do not utilize the unique possibilities offered by interfacial magnetic coupling effects in ferromagnetic (FM) multilayer systems. Here, the ultrafast photoenhanced interfacial exchange interactions is experimentally demonstrated in the ferromagnetic Co_2FeAl/(Ga,Mn)As system at low laser fluence levels by the time-resolved magneto-optical Kerr effect (TRMOKE). The pump light induces a transient torque that acts on the spins, leading to the magnetization precession along the equilibrium direction. At the temperature below the Curie temperature of the (Ga,Mn)As layer, $\boldsymbol{T_c}$ = 50 K, the excitation efficiency of the bilayer system is 30-40 times higher than without the (Ga,Mn)As layer due to the emergence of the dynamic exchange coupling interaction between two ferromagnetic layers. The coherent spin precessions persist to room temperature, indicating that proximity-induced ferromagnetism

plays a key role in the optical excitation mechanism in this bilayer heterostructure. The results highlight the importance of considering the range of interfacial exchange interactions in ferromagnetic heterostructures and how these magnetic coupling effects can be utilized for ultrafast, low-power spin manipulation.

3.1 Introduction

Ultrafast optical control of coherent spin dynamics in ferromagnetic heterostructures is currently of great interest because of its significance in spintronic devices and magnetic recording [1-9]. A great amount of research is devoted to discover non-thermal, low-power excitation processes to circumvent the disadvantages associate with thermal mechanisms [10-16]. A promising approach is to make use of the interaction between selectively photo-excited carriers and magnetization since the photo-carrier recombination time is considerably shorter than the thermal dissipation process. A promising idea is to utilize exchange-coupled systems, because the magnetic properties may respond notably to a small transient alteration of the exchange-coupling strength [17,18]. The combination of a ferromagnetic (FM) metal and a FM semiconductor is quite favorable for low-power spin manipulation, because the FM

semiconductor may have pronounced carrier effect on the magnetic properties [19].

As a promising spin injector, the half-metallic ferromagnetic material possesses extremely large spin polarization due to its special band structure that is composed of two spin bands. The majority spin (spin-up) band exhibits metallic properties with a nonzero density of states around the Fermi level, as seen on the left side in Fig. 3.1. The minority spin (spin-down) band shows semiconductor-like behavior with a gap at the Fermi level [20], as shown on the right side in Fig. 3.1. Therefore, the half-metallic compounds can be considered as a combination of metal and semiconductor [20]. Its half-metallicity leads to ideal 100% spin polarization of the charge carriers at the Fermi level [21], which has great potential in the development of ultrafast spintronic applications [22]. Among the half-metallic ferromagnets, a special class with the general formula X_2YZ, where X and Y are transition metals and Z is a main group element, is called full-Heusler alloy [23]. There is also another composition XYZ called half-Heusler alloy where one of four fcc sublattices is unoccupied [20]. Since the first discovery of the Cu_2MnAl ferromagnetic structure by Friedrich Heusler in 1903 [24], Heusler alloys have attracted lots of interests in the past century. One of the most well-known Heusler alloy is the Co_2FeAl compound material that has nearly full spin polarization with

high Curie temperature [25], which is crucial for spin-torque oscillators due to low switching current density.

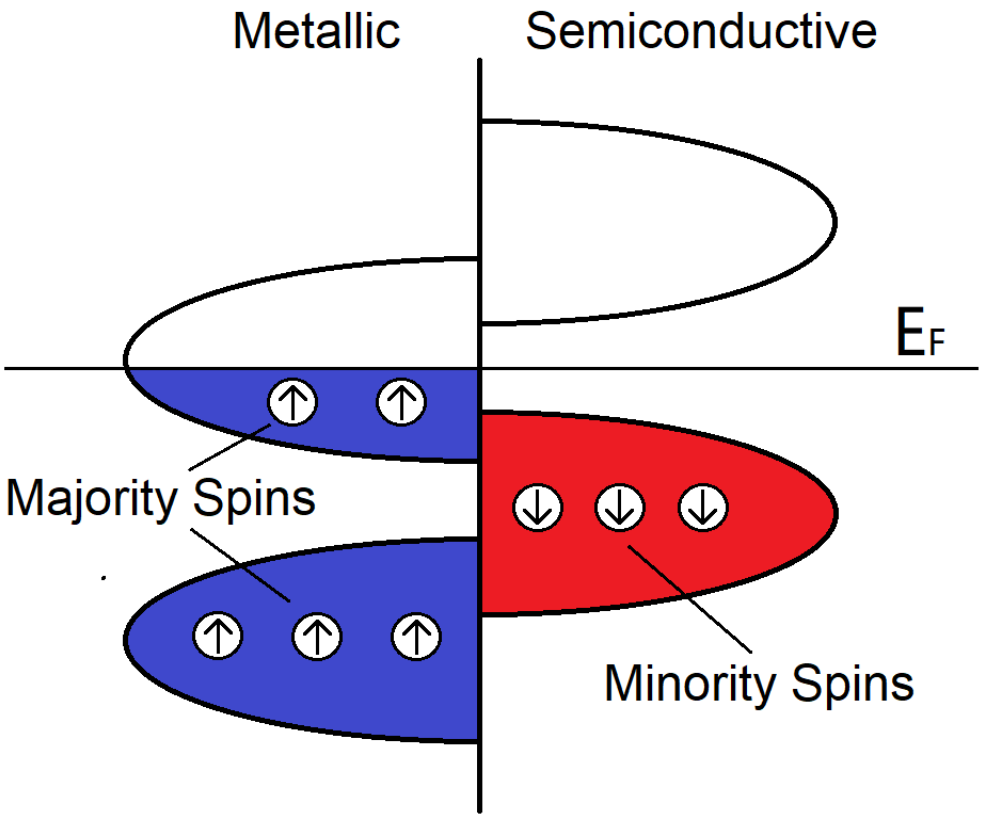

Figure 3.1 Schematic of band structure of half-metallic ferromagnetic material. E_F indicates Fermi level.

In the past decades, (III,Mn)V diluted magnetic semiconductors (DMSs), which are introduced by substituting group-III cations with Mn^{2+} ions in III-V-based DMSs, attract more and more attention since their

magnetic functionality is able to be mediated in ultrafast switching spintronic devices [22, 26-28]. Two kinds of influence are expected by introducing Mn^{2+} ions. On the one hand, magnetic moments are induced after substitution. On the other hand, these Mn acceptors are the source of free holes, which can mediate interactions between local magnetic moments and hence cause ferromagnetic ordering in the semiconductor material [29]. Among all the (III,Mn)V DMSs, (Ga,Mn)As is one of the most attractive structures because it introduces a spin component into the GaAs-based high-speed devices which have already been well studied and utilized in the semiconductor industry [29]. The photo-enhanced ferromagnetism of around 1% in (Ga,Mn)As has been discovered under pump excitation with energy density ~10 μJ/cm^2 [31]. Control of the Curie temperature ***Tc*** is achieved by applying external electric fields [32-33]. Recent studies demonstrated femtosecond optical control of coercivity [34] and complete reversal of magnetic hysteresis loop in (Ga,Mn)As [31, 34-35].

Considering the metal/(Ga,Mn)As bilayer system, the pump-probe magneto-optical spectroscopy can be an ideal experimental technique for detecting the spin dynamics and the exchange coupling interaction at the interfacial layers. Many works have been performed on the Fe/(Ga,Mn)As bilayers to investigate the static exchange coupling effect and the magnetization response under applied magnetic field [36-41]. Xie et al

reported the ferromagnetic proximity effect in the Co_2FeAl/(Ga,Mn)As bilayer system [42]. But the bilayer magnetization dynamics and their exchange coupling interaction has not been adequately understood. The question is still open whether it is possible to drive ferromagnetic magnetization at low laser fluence through exchange coupling across metal/semiconductor heterostructure interface.

3.2 Samples and Experiments

Co_2FeAl/(Ga,Mn)As bilayers are grown on GaAs (001) substrates by molecular-beam epitaxy (MBE) with two growth chambers (VG80) without being exposed to air during the entire synthesis process [42]. The thickness of Co_2FeAl and $Ga_{1-x}Mn_xAs$ (x=0.07) layers are 10 nm and 150 nm, respectively. The bilayers are capped with 2-nm thick Al layer to avoid oxidation. For reference, a single 10-nm thick Co_2FeAl layer is directly grown on GaAs (001) substrate by MBE without the (Ga,Mn)As layer. Reflection high-energy electron diffraction (RHEED) patterns, high-resolution double-crystal x-ray diffraction (DCXRD) measurements, and high-resolution cross-sectional transmission electron microscopy (HRTEM) reveal high-quality, single-crystalline, epitaxial growth of the Co_2FeAl and (Ga,Mn)As films, as seen in Fig. 3.2 [42]. The closeup inset reveals a

narrow (Ga,Mn)As (004) peak, indicating the high quality of the sample synthesis. However, the peak for the Co_2FeAl layer is missing. This is because the thickness of the Co_2FeAl layer is only 10 nm, which is too thin for the detection. In addition, the position of its XRD peak is very close to the (Ga,Mn)As peak and the GaAs peak, which makes it difficult to distinguish them [42].

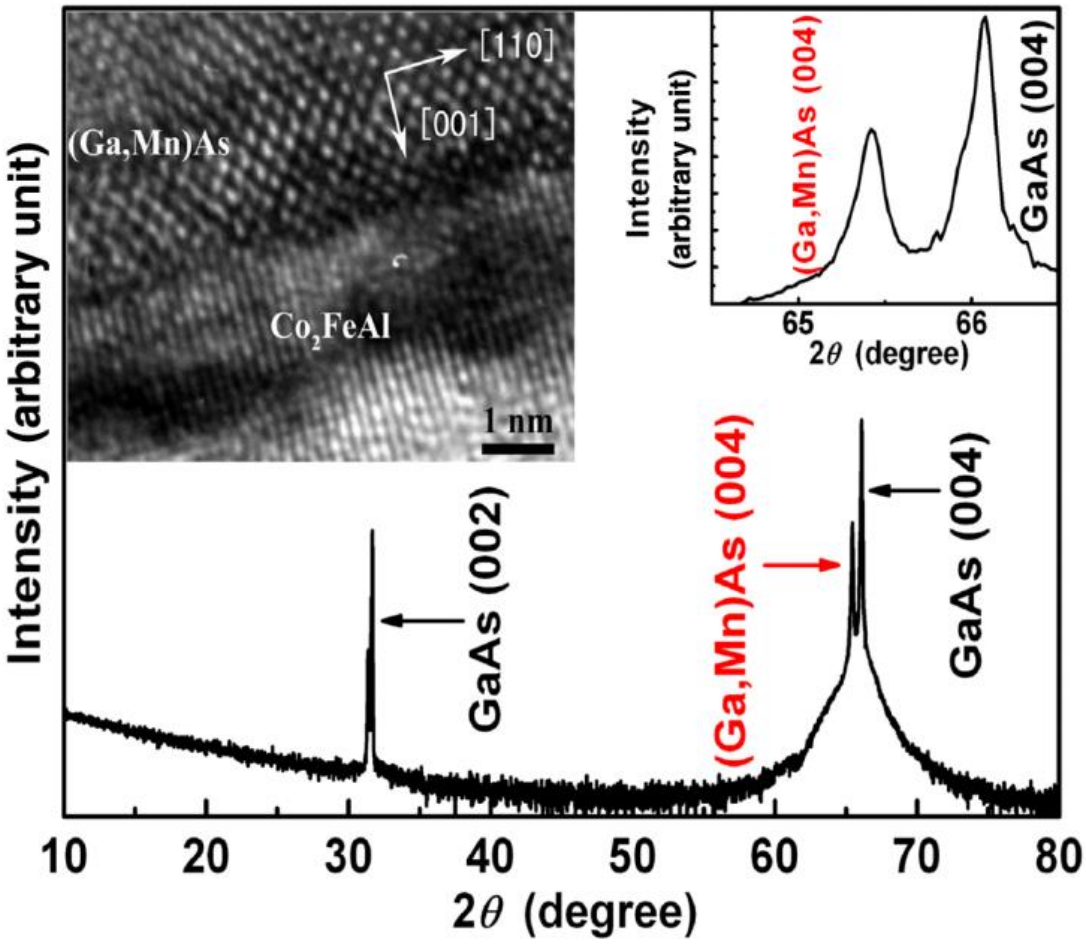

Figure 3.2 DCXRD measurement of Co_2FeAl/(Ga,Mn)As bilayer structure. Left inset shows HRTWM image. Right closeup inset exhibits

DCXRD curve from 64.5 degrees to 66.5 degrees as a clear view of (Ga,Mn)As (004) peak [42].

Magnetic characterization: Magnetic measurements are conducted from 5 to 300 K in a magnetic field of 1 Tesla using a SQUID magnetometer [42]. The magnetic coupling at the interface between Co_2FeAl and (Ga,Mn)As layers is probed with element-resolved XMCD measurements [42]. *Ab-initio* density functional calculations are performed to support the experimental results [42].

MOKE experiments: The ferromagnetic magnetization of the exchange-coupled Co_2FeAl/(Ga,Mn)As bilayer is measured using the longitudinal MOKE setup. The sample is illuminated with p-polarized light and the reflected s-polarized light is detected with a photodiode. The magnetic field is applied along the in-plane [110] or [-110] crystallographic directions. The measurements are conducted from 5 K to above room temperature.

TRMOKE experiments: For the pump-probe TRMOKE measurements, a Ti:sapphire oscillator laser system is employed, which produces 150-fs pulses at 800-nm wavelength with a repetition rate of 80 MHz. The probe fluence is fixed at ~0.5 $\mu J/cm^2$ and the pump fluence varies from 0.5-100 $\mu J/cm^2$. The probe pulses (λ=800 nm) utilize the balanced detection technique with a half-wave plate and Wollaston prism

to investigate the transient magnetic state change along longitudinal and polar directions. The measurements are conducted from 5 K to above room temperature. An external magnetic field is applied on the surface plane of the sample, as shown in Fig. 3.3.

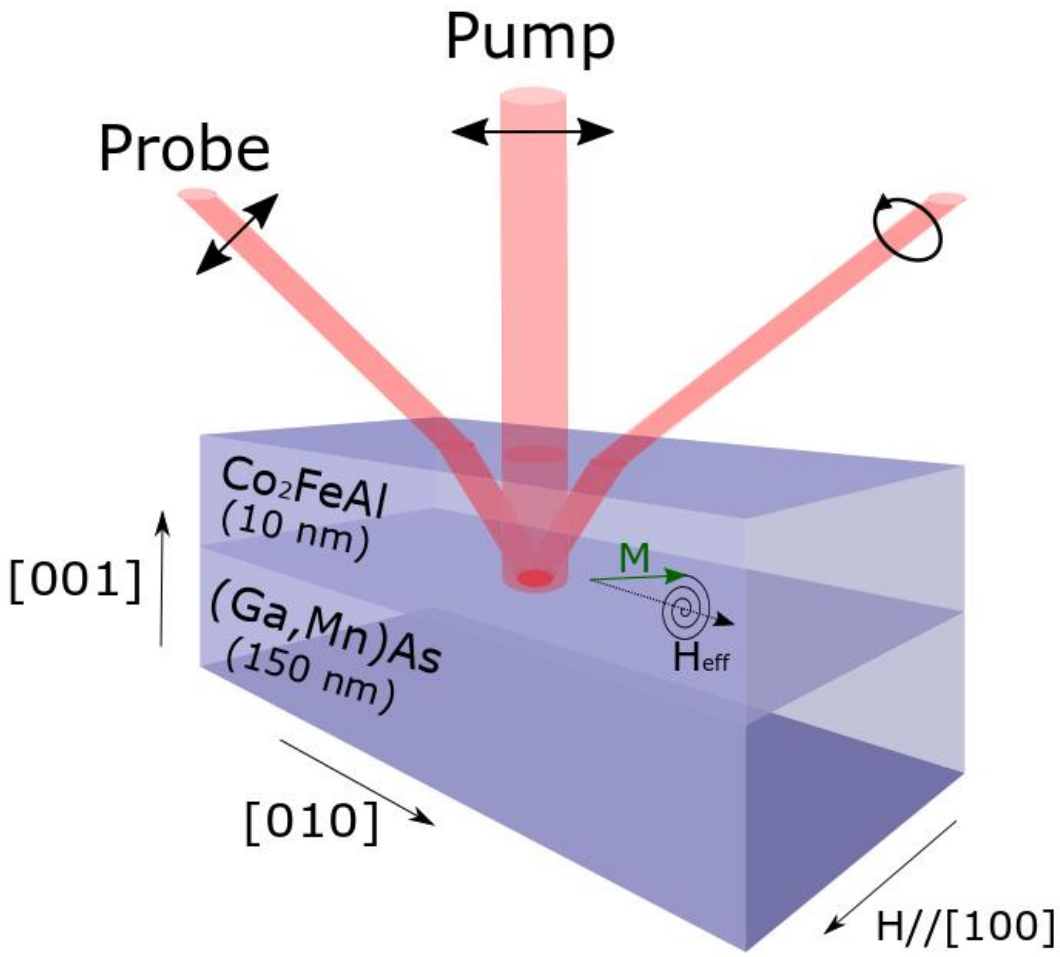

Figure 3.3 Schematic of TRMOKE measurement geometry, depicting the structure of the sample and the magnetization ***M*** precessing around the effective field $\boldsymbol{H_{eff}}$ in Co_2FeAl/(Ga,Mn)As bilayer in a canted magnetization configuration with H applied along hard axis [1-10].

3.3 Magnetization Precession and Simulation

The ferromagnetic material is expected to show magnetocrystalline anisotropy due to the spin-orbit interaction. In the 10-nm thick Co_2FeAl layer, the in-plane uniaxial anisotropy comes with an easy axis along the [110] direction and a hard axis along the [1-10] direction, while the in-plane fourfold anisotropy has easy axes along the [110] direction and the [1-10] direction, as shown in Fig 3.4(a) where the external magnetic field is applied along the easy axis [110]. The 150-nm thick (Ga,Mn)As film reveals an easy axis along the [1-10] direction below the Curie temperature $\boldsymbol{T_c}$ = 50 K [42], as revealed by the minor loop in Fig. 3.4(b). In the hysteresis loop at 15 K (in black), there is a minor loop at magnetic field around 10 Oe, indicating a magnetization reversal in the (Ga,Mn)As layer, while no switching behavior is observed in the Co_2FeAl layer. This can be seen as evidence of the noncollinearity between the two ferromagnetic orders in the Co_2FeAl layer and the (Ga,Mn)As layer. Due to the strong coupling at the interface and the relatively strong cubic anisotropy constant $\boldsymbol{K_1}$ of Co_2FeAl, the interfacial spin alignment of the (Ga,Mn)As layer should be very close to that in the Co_2FeAl layer [42]. At low temperature ($\boldsymbol{T} < \boldsymbol{T_c}$) a ferromagnetic alignment of Mn spins in the (Ga,Mn)As layer is expected, whereas at high temperatures ($\boldsymbol{T} > \boldsymbol{T_c}$) Mn ions extending a few nanometers in the (Ga,Mn)As layer remain spin-polarized due to the ferromagnetic proximity effect [42]. Such a FM metal/semiconductor

heterostructure is ideal for examining interfacial magnetic interactions, due to their different magnetic anisotropy and strong interfacial exchange coupling. Furthermore, one can envision an additional level of optoelectronic control over the underlying exchange interaction, which makes this bilayer system attractive for ultrafast coherent spin manipulation studies.

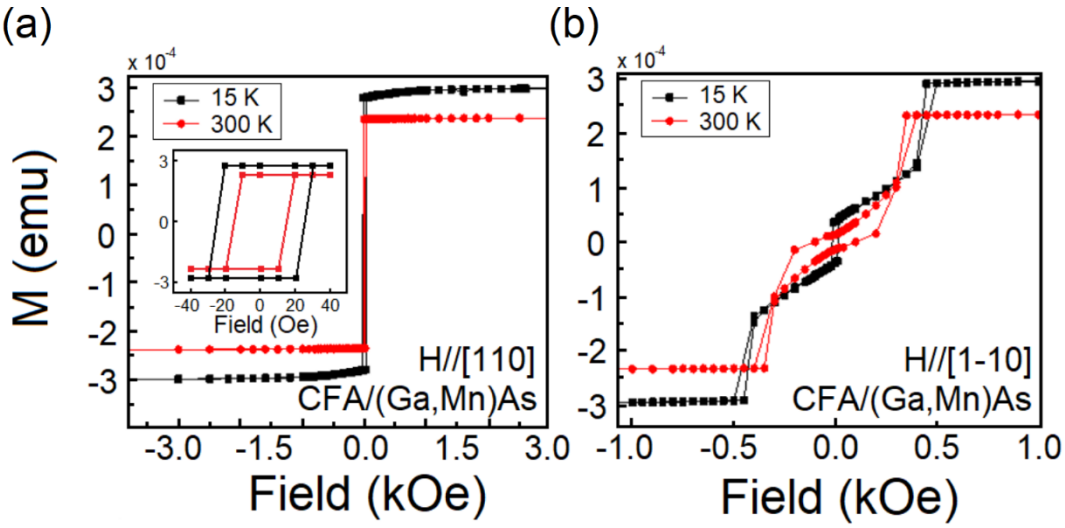

Figure 3.4 (a) SQUID measurement in Co_2FeAl/(Ga,Mn)As bilayer along the easy axis [110] direction. The inset shows the closeup around zero magnetic field. (b) SQUID measurement in Co_2FeAl/(Ga,Mn)As bilayer along the hard axis [1-10] direction[1].

Coherent spin precessions in the Co_2FeAl/(Ga,Mn)As bilayer and a reference sample of a single Co_2FeAl layer are investigated by near-infrared (λ=800 nm), low-fluence (I_0 = 5 μJ/cm^2), pump-probe TRMOKE

[1] The data was taken by Prof. Haibin Zhao's group in Fudan University.

measurements (see Methods) in a canted magnetization configuration where the magnetic field ***H*** is applied along the hard axis [1-10], as depicted in Fig. 3.3. In equilibrium, the magnetization ***M*** is along an effective field $\boldsymbol{H_{eff}}$, which is the sum of ***H***, the demagnetizing field, the anisotropy fields, and the exchange-coupling field. The s-polarized incident pump pulses create a strong dynamic spin torque $\boldsymbol{\tau_{ex}(t)}$ in the FM-coupled Co_2FeAl/(Ga,Mn)As bilayer through modulation of interfacial exchange interaction. The magnetization ***M*** starts to precess, and when $\boldsymbol{\tau_{ex}(t)}$ has vanished, the vector ***M*** is away from its original equilibrium orientation along $\boldsymbol{H_{eff}}$. Therefore, it starts to precess around $\boldsymbol{H_{eff}}$ in a damped circling way, as depicted in Fig. 3.3. The ultrafast spin precession excitation is described by a modified Landau-Lifshitz-Gilbert (LLG) equation with an additional torque term [17]:

$$\frac{\partial \boldsymbol{M}}{\partial \boldsymbol{t}} = -\boldsymbol{\gamma}\left(\boldsymbol{M} \times \boldsymbol{H_{eff}}\right) + \boldsymbol{\alpha M} \times \frac{\partial \boldsymbol{M}}{\partial \boldsymbol{t}} + \boldsymbol{\tau_{ex}(t)}, \qquad (3.1)$$

where γ is gyromagnetic ratio, $\boldsymbol{\alpha}$ is the Gilbert damping constant, $\boldsymbol{\tau_{ex}(t)} = -\boldsymbol{\gamma}(\boldsymbol{M} \times \Delta \boldsymbol{H_{ex}(t)})$ denotes the instant spin exchange-coupling torque, and $\Delta \boldsymbol{H_{ex}(t)}$ is the change of FM exchange field $\boldsymbol{H_{ex}}$ by modulation of interfacial exchange coupling strength $\boldsymbol{J_1}$, as discussed further below.

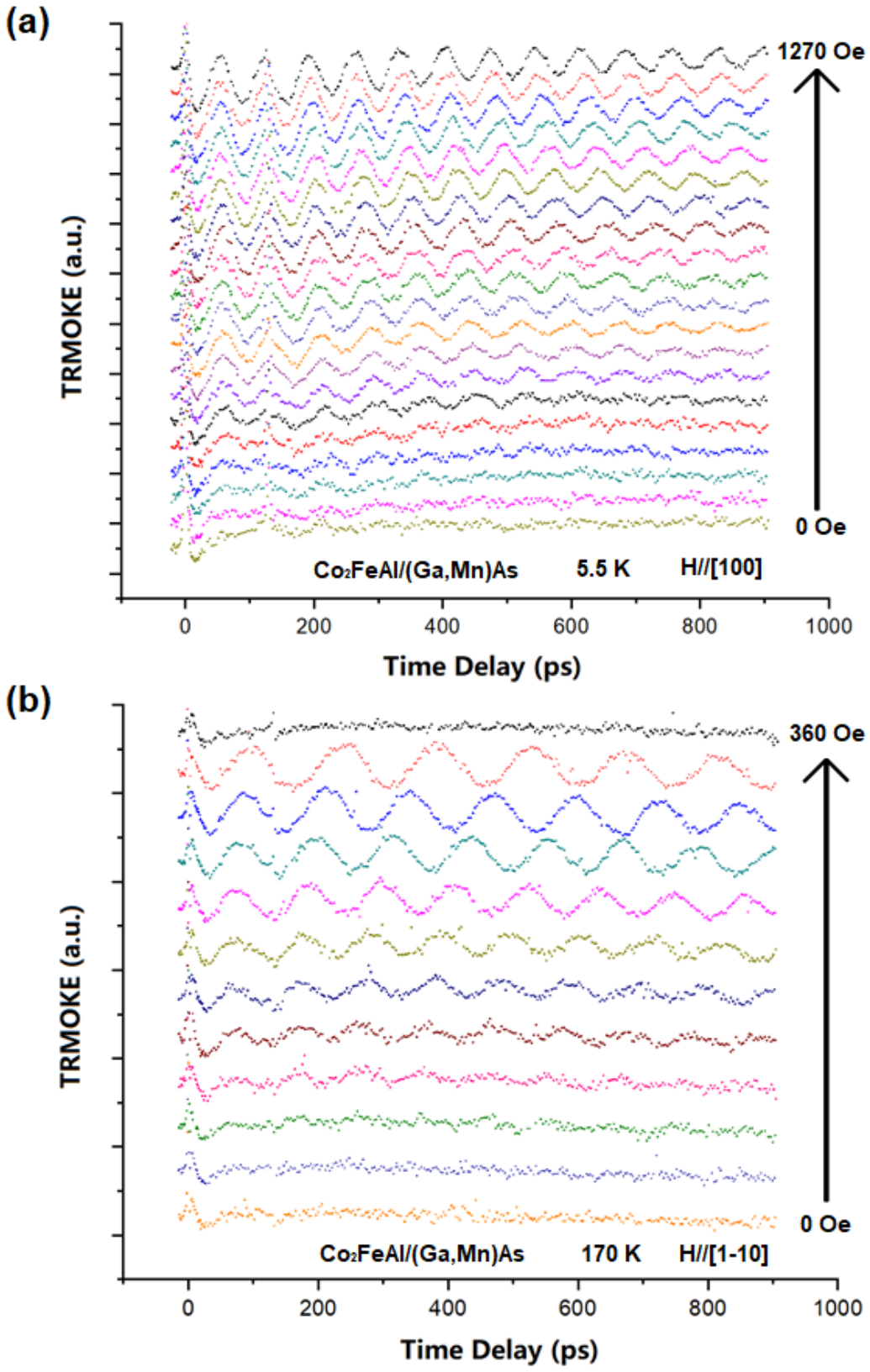
(a)
TRMOKE (a.u.)
1270 Oe
0 Oe
Co2FeAl/(Ga,Mn)As 5.5 K H//[100]
0
200
400
600
800
1000
Time Delay (ps)
(b)
TRMOKE (a.u.)
360 Oe
0 Oe
Co2FeAl/(Ga,Mn)As 170 K H//[1-10]
0
200
400
600
800
1000
Time Delay (ps)

Figure 3.5 TRMOKE data from Co_2FeAl/(Ga,Mn)As bilayer with magnetic field along [100] direction at 5.5 K (a) and along [1-10] direction at 170 K (b).

Figure 3.5 presents the field-dependence of the TRMOKE measurement in the Co_2FeAl/(Ga,Mn)As material. One can see the magnetization precesses in a damped circling way in the bilayer when the external magnetic field is applied along both the intermediate axis [100] (Fig. 3.5 (a)) and hard axis [1-10] (Fig. 3.5(b)). One can also see the precession signal exhibits an obvious field-dependence in both measurements. The magnetization precession is observed not only at temperatures (5.5 K) below the Curie temperature of (Ga,Mn)As ***Tc*** = 50 K, but also at much higher temperature (170 K) where the (Ga,Mn)As layer has already turned into the paramagnetic phase and lost its bulk ferromagnetism, indicating the coherent spin precession may be arising from the Co_2FeAl layer.

Figure 3.6 displays the TRMOKE result from Co_2FeAl/(Ga,Mn)As bilayer at 5 K with pump pulse fluence I_0 = 5 μJ/cm^2 and magnetic field H = 227 Oe. The magnetic response is modelled by a red curve and a blue curve separately in order to highlight the different dynamic magnetization processes. The magnetization precession is well fitted by a damped sine function superimposed onto an exponentially-decaying background, as following:

$$\boldsymbol{\theta_k = a_0 + b_0\, exp\left(-\frac{t}{\tau}\right) + A \times exp\left(-\frac{t}{\tau}\right) sin(2\pi ft + \varphi_0)}, \qquad (3.2)$$

where $\boldsymbol{a_0}$ denotes the background magnitudes and $\boldsymbol{b_0}$ represents the decay time, $\boldsymbol{A}$ is the amplitude of the magnetization precession, $\boldsymbol{\tau}$ is the relaxation time of the magnetization precession, $\boldsymbol{f}$ is the precession frequency and $\boldsymbol{\varphi_0}$ is the phase. The blue curve (Fig. 3.6) shows the fitting result, which agrees well with the experiment data. There is an initial dip observed at ~30 ps which is obviously different from the thermal demagnetization that usually occurs at less than 10 ps, as reported by Qi et al [43]. This dip can be attributed to the ultrafast demagnetization induced by photo-excited hot electrons, which then diffuse quickly through the Co_2FeAl layer. The subsequent relatively gradual rise on a 100-ps time scale arises from the enhanced magnetization due to the increased density of the photo-excited holes that live longer than the electrons. Such increase of magnetization with weak photo-excitation was also observed in (Ga,Mn)As [30, 44] and in (In,Mn)As [45]. At a longer time scale, the magnetization enhancement decays slowly due to the processes of hole diffusion and recombination. The initial ultrafast demagnetization and the following gradual enhancement of magnetization is well described by [30]:

$$\boldsymbol{\theta_k = \Delta\theta_k^d\, exp\left(-\frac{t}{\tau_d}\right) + \Delta\theta_k^m \left[1 - exp\left(-\frac{t}{\tau_m}\right)\right] exp(-\frac{t}{\tau_c})}, \qquad (3.3)$$

where $\Delta\boldsymbol{\theta}_{\boldsymbol{k}}^{\boldsymbol{d}}$ and $\boldsymbol{\tau}_{\boldsymbol{d}}$ denote the magnitude and the recovery time of the demagnetization, respectively, $\Delta\boldsymbol{\theta}_{\boldsymbol{m}}^{\boldsymbol{d}}$ and $\boldsymbol{\tau}_{\boldsymbol{m}}$ represent the magnitude and the buildup time of the enhanced magnetization, respectively, and $\boldsymbol{\tau}_{\boldsymbol{c}}$ is the relaxation time of the increase in magnetization. The simulation curve is indicated in red in Fig. 3.6. As a result, the Kerr rotation of the ultrafast demagnetization turns out to be -0.46 micro degree with recovery time of 30 ps, while the magnetization enhancement turns out to be 0.41 micro degree with buildup time of 32 ps and decay time of 240 ps.

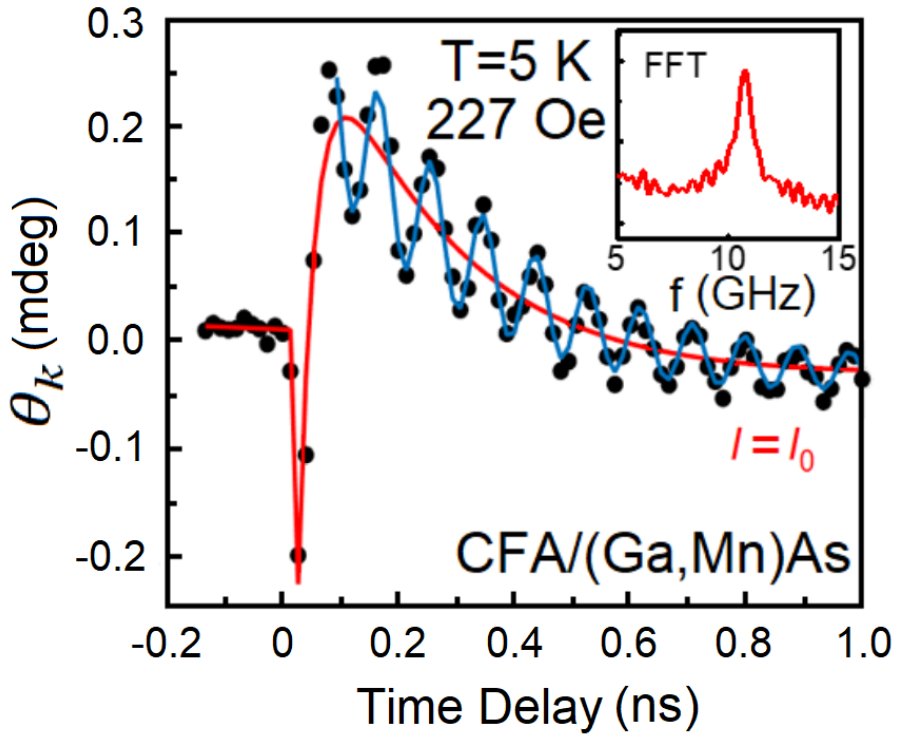

Figure 3.6 TRMOKE data from Co_2FeAl/(Ga,Mn)As bilayer at 5K, exhibiting the initial demagnetization (-0.41 mdeg) and the subsequent

100-ps magnetization rise (0.46 mdeg) and uniform spin precession. The red and blue curves are fits of LLG equation[2].

The fast Fourier transform (FFT) of the TRMOKE signal is shown in the inset of Fig. 3.6, indicating a precession frequency around 11 GHz, which is similar to that observed in the single Co_2FeAl layer [46]. The uniform magnetization precession exists up to room temperature where ferromagnetic order is absent in the (Ga,Mn)As layer, indicating the uniform magnetization precession originates from the Co_2FeAl film. Actually, there might be no uniform magnetization in the (Ga,Mn)As layer when it is exchange-coupled to the Co_2FeAl layer. The ferromagnetic magnetization in the Co_2FeAl layer applies a torque on the Mn spins at the interface, which leads to reorientation of the magnetic moments with increasing depth in the (Ga,Mn)As layer [47]. The magnetic inhomogeneities in the (Ga,Mn)As layer significantly increase the damping of the magnetization precession. Although the (Ga,Mn)As layer contributes to the overall MOKE signal of the bilayer, this contribution does not affect the amplitude of the oscillating TRMOKE signal originating from magnetization precession in the Co_2FeAl layer. We can therefore ascribe the precession mode observed in the Co_2FeAl/(Ga,Mn)As bilayer to the uniform magnetization precession of Co_2FeAl.

[2] The data was taken by Prof. Haibin Zhao's group in Fudan University.

In order to fully understand the magnetization dynamics in the Co_2FeAl/(Ga,Mn)As bilayer, the quantitative value of the magnetic anisotropy fields and the exchange coupling fields need to be determined. The magnetization dynamics in this bilayer system is described by a modified LLG equation with an additional term of exchange coupling torque (Eq. (3.1)). The magnetic free energy is also more complicated, as represented by:

$$\boldsymbol{E = -M_s H cos(\varphi_M - \varphi_H) - (2\pi M_s^2 + K_\perp) sin^2 \varphi_\perp + K_u sin^2 \varphi_M}$$

$$\boldsymbol{+\frac{K_1}{4} sin^2(2\varphi_M) + K_{ud} sin(\varphi_M - \varphi_{ud})} \qquad (3.4)$$

$$\boldsymbol{+K_{ra} cos^2(\varphi_M - \varphi_H) + J_1 M_s M_s' cos\theta}.$$

The last term $\boldsymbol{J_{ex} = J_1 M_s M_s' cos\theta}$ represents the contribution from the exchange coupling effect, where $\boldsymbol{M_s}$ is the saturation magnetization in the Co_2FeAl layer and $\boldsymbol{M_s'}$ is the saturation magnetization in the (Ga,Mn)As layer, $\boldsymbol{J_1}$ is the exchange-coupling stiffness, and $\boldsymbol{\theta}$ is the angle between the magnetization directions in Co_2FeAl and (Ga,Mn)As. $\boldsymbol{H}$ denotes the applied field. $\boldsymbol{\varphi_M}$ is the equilibrium angle of the magnetization vector with respect to the easy axis [110] direction. $\boldsymbol{\varphi_H}$ is the angle between external field and [110] axis. $\boldsymbol{\varphi_\perp}$ represents the angle of the magnetization vector with respect to the sample plane. $\boldsymbol{\varphi_{ud}}$ denotes the angle of unidirectional anisotropy field. $\boldsymbol{K_\perp}$, $\boldsymbol{K_u}$, $\boldsymbol{K_1}$, $\boldsymbol{K_{ud}}$ and $\boldsymbol{K_{ra}}$ are the out-of-plane, in-plane

uniaxial, in-plane crystalline cubic, unidirectional and rotatable magnetic anisotropy constants, respectively.

The uniform magnetization precession can be described by Eq. (2.2.11). According to the free energy (Eq. 3.4), $\boldsymbol{H_a}$ and $\boldsymbol{H_a}$ have the following expressions:

$$\boldsymbol{H_a = Hcos(\varphi_M - \varphi_H) + H_u cos(2\varphi_M) + H_1 cos(4\varphi_M)} \\ \boldsymbol{- \frac{H_{ud}}{2} sin(\varphi_M - \varphi_{ud}) - H_{ra} cos2(\varphi_M - \varphi_H) - J_1 M_s' cos\theta}$$

$$\boldsymbol{H_b = Hcos(\varphi_M - \varphi_H) + 4\pi M_{eff} - H_u sin^2\varphi_M + \frac{H_1}{4}\left(3 + cos(4\varphi_M)\right)} \\ \boldsymbol{- \frac{H_{ud}}{2} sin(\varphi_M - \varphi_{ud}) - H_{ra} cos^2(\varphi_M - \varphi_H) - J_1 M_s' cos\theta}$$

where $\boldsymbol{M_{eff} = M_s + \frac{K_\perp}{2\pi M_s}}$ is the effective magnetization of the sample, $\boldsymbol{H_u = \frac{2K_u}{M_s}}$, $\boldsymbol{H_1 = \frac{2K_1}{M_s}}$, $\boldsymbol{H_{ud} = \frac{2K_{ud}}{M_s}}$, $\boldsymbol{H_{ra} = \frac{2K_{ra}}{M_s}}$ represent the uniaxial, cubic, unidirectional and rotatable anisotropy fields, respectively, and $\boldsymbol{\gamma = \frac{\gamma_e g}{2}}$ (with $\gamma_e = 1.76\times10^7$ Hz/Oe) is the gyromagnetic ratio.

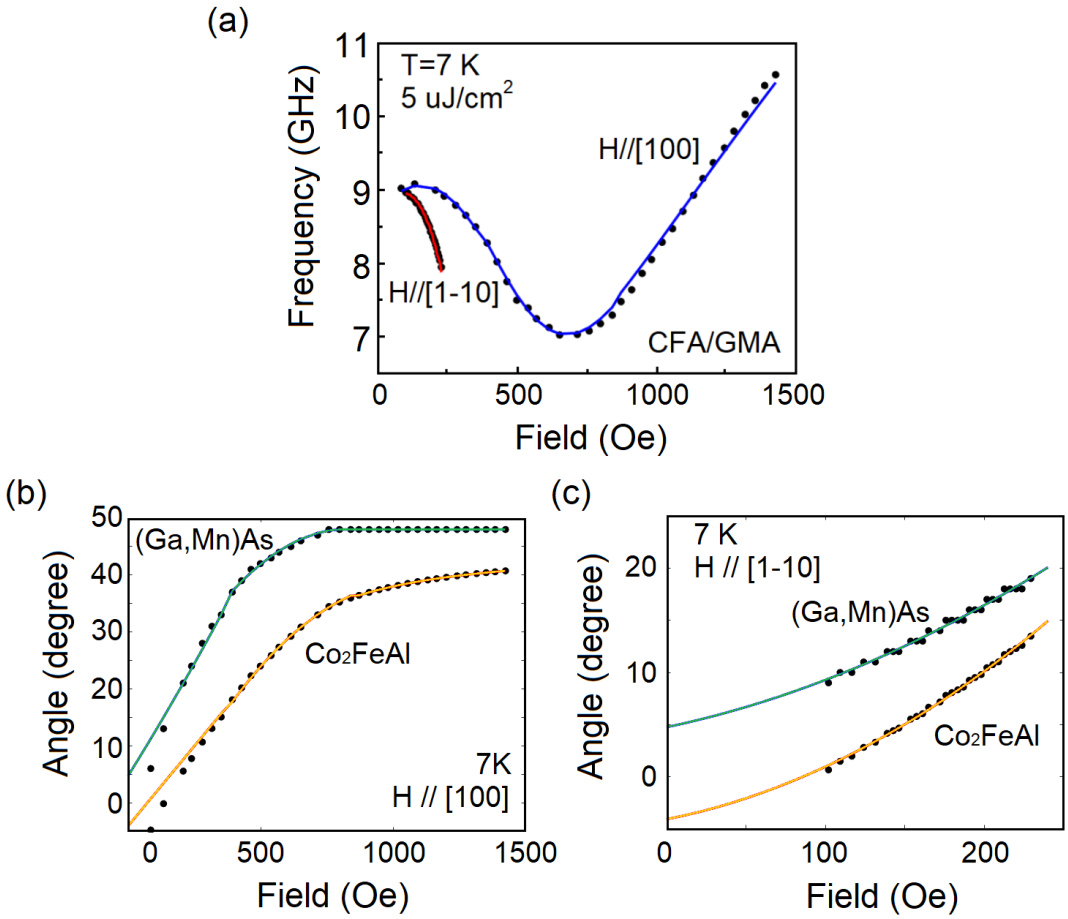

Figure 3.7 (a) Precession frequency as a function of external applied field along intermediate axis [100] and hard axis [1-10]. (b) Equilibrium angle of magnetization in Co_2FeAl and (Ga,Mn)As as a function of external magnetic field applied along [100] direction. (c) Equilibrium angle of magnetization in Co_2FeAl and (Ga,Mn)As as a function of external magnetic field applied along [1-10] direction.

Figure 3.7(a) shows the field dependence of the magnetization precession frequency at 7 K with pump fluence of 5 $\mu J/cm^2$ on the Co_2FeAl/(Ga,Mn)As bilayer. The blue and red curves are the fits based on

Eq. (2.2.11) for data measured with external magnetic field applied along intermediate axis [100] and hard axis [1-10], respectively. The best fitting results are $\boldsymbol{K_u}$ = 0 erg/cm^3, $\boldsymbol{K_1}$ = 290,000 erg/cm^3, $\boldsymbol{K_{ud}}$ = 155,000 erg/cm^3 along [100] direction, $\boldsymbol{K_{ra}}$ = 30,000 erg/cm^3, $\boldsymbol{M_{eff}}$ = 880 emu/cm^3, $\boldsymbol{M_s}$ = 1,127 emu/cm^3 and $\boldsymbol{J_{ex}}$ = 326,056 erg/cm^3. The field dependence of the corresponding equilibrium angles in Co_2FeAl and (Ga,Mn)As are shown in blue and red, respectively, as shown in Fig. 3.7(b) and Fig. 3.7(c). One can see as the intensity of the external magnetic field becomes stronger, the equilibrium direction of the magnetization is "pulling" towards the direction of the external magnetic field.

Figure 3.8 exhibits the angle dependence of the magnetic free energy under different applied magnetic fields. Since the equilibrium direction of the magnetization in both layers lies at the minimum of the magnetic free energy, the angle of the equilibrium direction is calculated by minimizing the free energy during the simulation process.

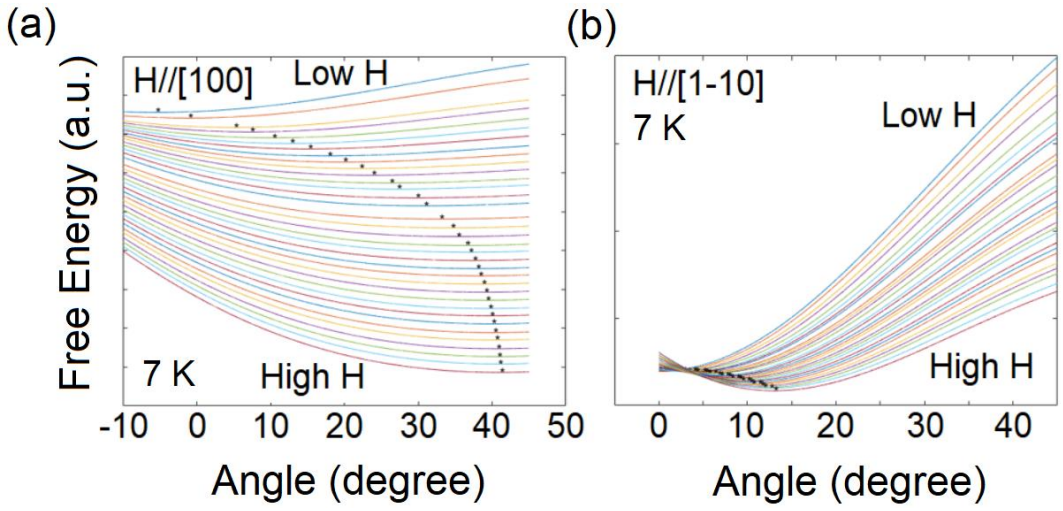

Figure 3.8 Magnetic free energy as a function of magnetization direction in Co_2FeAl layer with the external magnetic field applied along (c) [100] direction and (d) [1-10] direction. Curves in different colors correspond to different external fields. The black dot in each curve indicates the minimum of magnetic free energy for each applied field.

3.4 Photo-enhanced Amplitude of Magnetization Precession

In order to proof that the photo-enhanced excitation is induced by the (Ga,Mn)As layer, we performed TRMOKE experiment on both the Co_2FeAl/(Ga,Mn)As bilayer and the single Co_2FeAl film under the same experimental conditions. Figure 3.9 (squares) shows TRMOKE results from Co_2FeAl film directly grown on GaAs(001) substrate, which are remarkably different from the Co_2FeAl/(Ga,Mn)As bilayer. First, very little picosecond demagnetization and no magnetization rise on a 100 ps time scale are observed. Second, almost no coherent spin precession signal can be seen with the same excitation laser fluence as the measurement on Co_2FeAl/(Ga,Mn)As bilayer, while only small oscillations (circles) are noticeable at higher pump energy density, $I = 15\ I_0$. One can clearly see that the spin precession amplitude is much larger in the Co_2FeAl/(Ga,Mn)As bilayer than in the Co_2FeAl without the (Ga,Mn)As

layer. The key finding here is that the excitation efficiency is improved by 30-40 times in the Co_2FeAl/(Ga,Mn)As bilayer! This significant increase in spin precession amplitude below the Curie temperature of (Ga,Mn)As may not be attributed simply to the enhancement of the static MOKE signal from (Ga,Mn)As layer. In order to elucidate the enhanced optical excitation mechanism, fluence-, field- and temperature-dependent TRMOKE measurements have been carried out, as discussed below.

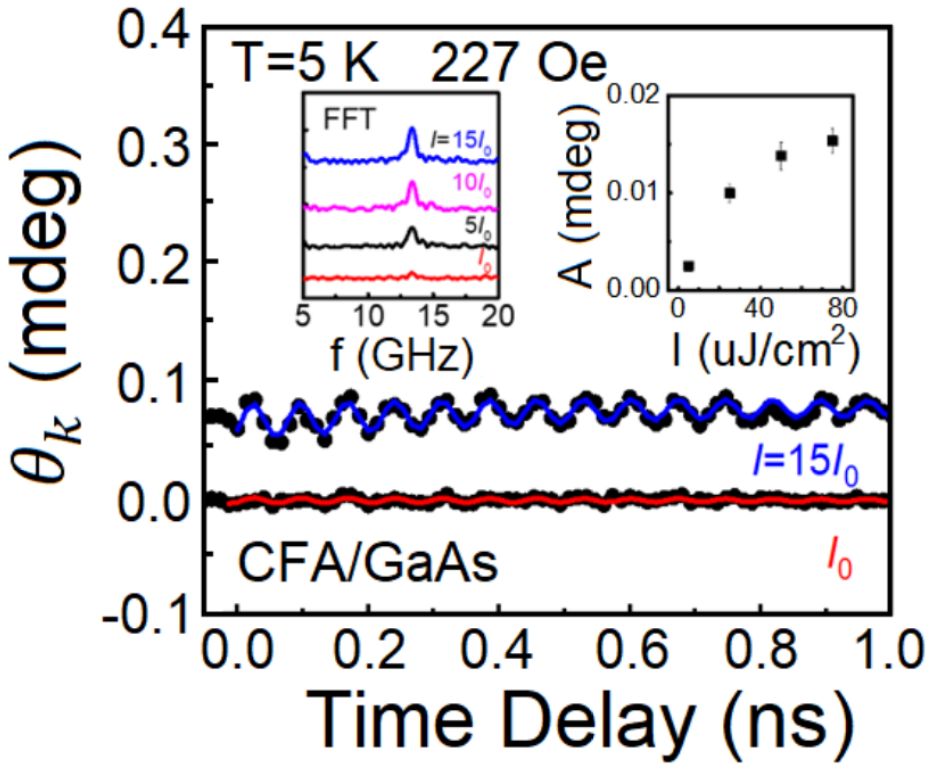

Figure 3.9 TRMOKE data from Co_2FeAl layer without (Ga,Mn)As layer at 5K. The FFT analysis for precession frequency and the precession amplitude as a function of pump-energy density are shown as insets[3].

[3] The data was taken by Prof. Haibin Zhao's group in Fudan University.

Figures 3.10(a) present TRMOKE results from Co_2FeAl/(Ga,Mn)As bilayer as a function of pump-pulse fluence with H = 227 Oe applied along the hard axis [1-10]. The pump energy density dependence of the precession amplitude on both Co_2FeAl/(Ga,Mn)As bilayer and single Co_2FeAl layer is shown in Fig. 3.10(b). The precession amplitude A increases dramatically with increasing pump-pulse fluence, making the magnetization dynamics a sensitive function of the photoexcited hole density, $\Delta \boldsymbol{p}$. One can also see the precession amplitude in Co_2FeAl/(Ga,Mn)As bilayer is significantly larger than in the single Co_2FeAl film under the same energy density of the pump excitation.

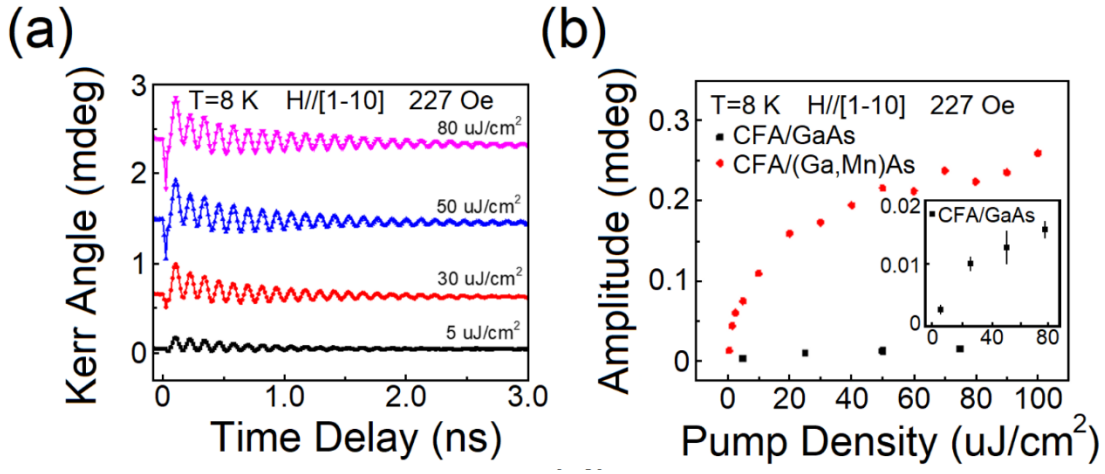

Figure 3.10 (a) TRMOKE results from Co_2FeAl/(Ga,Mn)As bilayer at 8 K with $\boldsymbol{H}$ applied along hard axis [1-10] for different pump-energy densities. (b) Precession amplitude as a function of pump-energy density for

Co_2FeAl/(Ga,Mn)As (red dots) and Co_2FeAl/GaAs (blue dots), respectively. The inset shows close-up of precession amplitude in single Co_2FeAl film[4].

The field dependence of the magnetization precession amplitude in Co_2FeAl/(Ga,Mn)As bilayer at different temperatures with ***H*** applied along intermediate axis [100] and hard axis [1-10] are shown in Fig. 3.11(a) and Fig. 3.11(b). When the magnetic field is applied along the [100] direction, a peak of the precession amplitude occurs at a field around 500 Oe, while the precession amplitude increases nearly linearly with applied field along the [1-10] direction. Fig. 3.11(c) presents pump-probe measurements with applied field of 411 Oe along the [1-10] direction. The TRMOKE results at T = 5 K and 25 K clearly exhibit the photo-induced transient enhancement of magnetization with 100-ps rise time after initial fast demagnetization, while at T = 80 K, 170 K and 260 K the transient enhancement of magnetization is absent (Fig. 3.11(c)). Figure 3.11(d) displays the temperature dependence of the precession amplitude ***A*** for three applied fields: 227 Oe, 374 Oe and 411 Oe. From the data, one can clearly distinguish two distinct regimes: (i) Below $\boldsymbol{T_c}$ = 50 K, ***A*** rapidly decreases with increasing temperature; and (ii) above $\boldsymbol{T_c}$, ***A*** remains constant up to room temperature at small magnitude. Furthermore, at ***T*** = 5 K, ***A*** strongly decreases with decreasing field (411 Oe to 227 Oe), and remains smaller at lower fields up to room temperature. This behavior clearly suggests that

[4] The data was taken by Prof. Haibin Zhao's group in Fudan University.

the proximity-induced ferromagnetism plays a crucial role in the optical excitation mechanism of coherent spin precession in Co_2FeAl/(Ga,Mn)As bilayer. Note that we observed that the excitation efficiency is increased by 30-40 times in the Co_2FeAl/(Ga,Mn)As bilayer than in the Co_2FeAl/GaAs structure under the same experimental conditions at 5 K. For the Co_2FeAl/(Ga,Mn)As bilayer, the precession amplitude of the magnetization is roughly 10 times larger at 5 K than at room temperature. We attribute the origin of this enhancement to the modulation of the interfacial ferromagnetic exchange coupling effect. However, the precession amplitude in the reference sample Co_2FeAl/GaAs keeps almost unchanged in 5-300 K. This suggests that the magnetization precession amplitude is 3-4 times larger at room temperature in the Co_2FeAl/(Ga,Mn)As bilayer than in the Co_2FeAl/GaAs structure. This enhancement can be ascribed to the magnetic proximity effect [42]. At a temperature above $\boldsymbol{T_c}$ = 50 K, the (Ga,Mn)As layer exhibits paramagnetic properties. The spin polarization of Fe(Co) magnetizes the (Ga,Mn)As film due to the magnetic proximity effect without bulk ferromagnetic orders formed [42]. As a result, the Mn spins couple closely to the Fe(Co) spins so that there is no large exchange-coupling torque between them. When the temperature falls below T_c = 50 K, the ferromagnetism establishes and begins to dominate the magnetic behavior in the (Ga,Mn)As layer. The ferromagnetic exchange interaction between the two ferromagnets thus strengthens in the bilayer system.

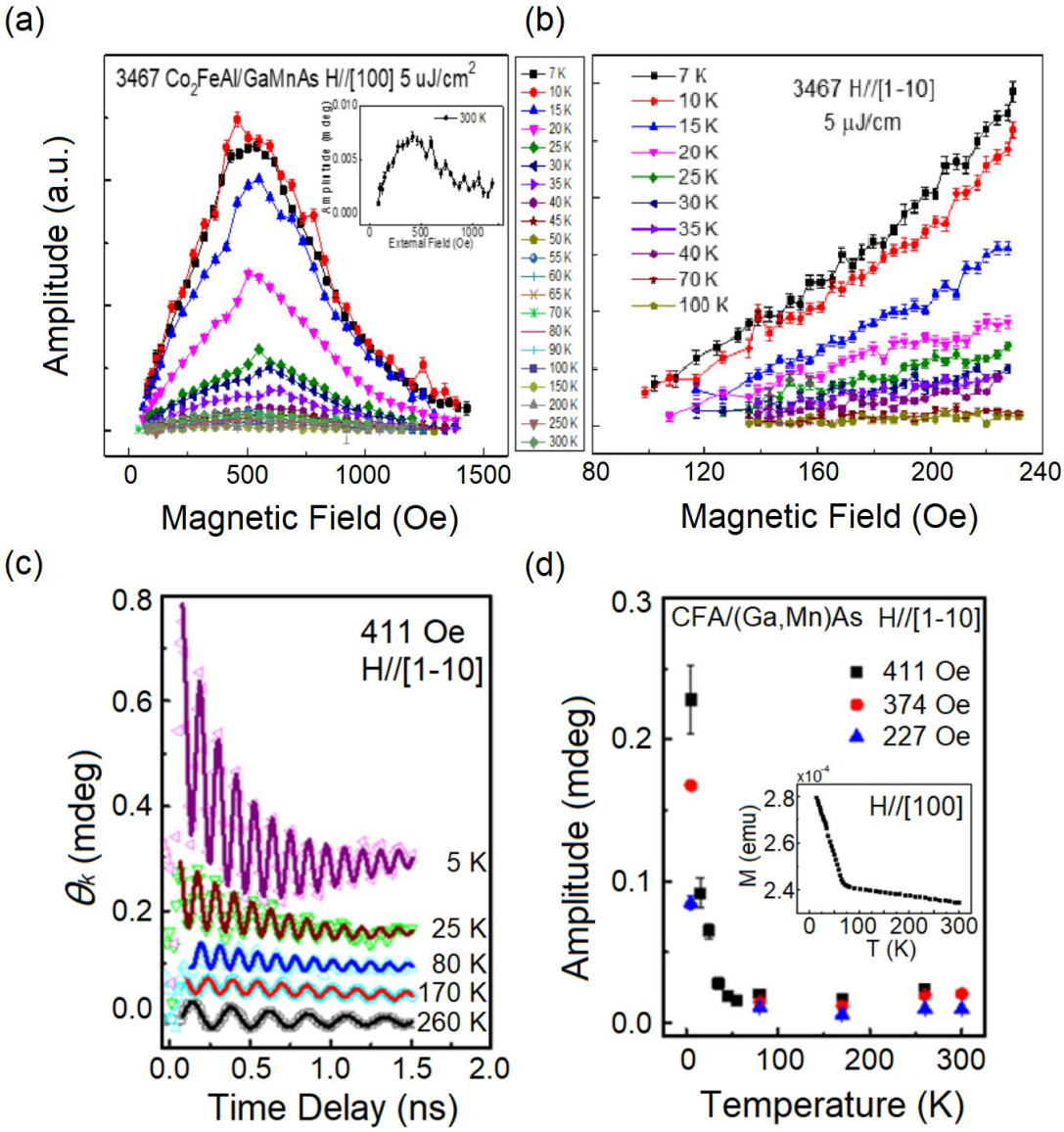

Figure 3.11 Field dependence of precession amplitude in Co_2FeAl/(Ga,Mn)As bilayer at different temperatures with ***H*** applied along intermediate axis [100] (a) and hard axis [1-10] (b). (c) TRMOKE signal with ***H*** of 411 Oe along [1-10] direction at different temperatures. (d) Precession amplitude as a function of temperature at different applied

fields. Inset: temperature dependence of static magnetization in Co_2FeAl/(Ga,Mn)As bilayer[5].

The amplitude of magnetization precession is approximated by the change in magnetization direction due to the photoenhanced interfacial exchange interaction, as expressed by:

$$\boldsymbol{A} = \boldsymbol{a}\Delta\boldsymbol{\varphi}, \tag{3.5}$$

where $\boldsymbol{a}$ is a scaling pre-factor for the conversion from $\Delta\boldsymbol{\varphi}$ to $\boldsymbol{A}$, and $\Delta\boldsymbol{\varphi}$ is the change in magnetization direction. By introducing a modulation onto the exchange coupling constant, $\Delta\boldsymbol{\varphi}$ is calculated and is then used to simulate the precession amplitude $\boldsymbol{A}$. The fits for data at 7 K are shown in blue and red with applied external field along the [100] direction and [1-10] direction, respectively, as shown in Fig. 3.12. The simulation result of the modulation in exchange coupling fields turns out to be an increase of 20% in $\boldsymbol{J_1}$ and 6% in $\boldsymbol{K_{ud}}$. The simulation of *A* versus *H* (red curve), where *A* is assumed to be proportional to the change of equilibrium magnetization direction caused by photo-induced modulation of J_1, agrees quite well with the experimental data. Simulation of *A* versus *H* by modulation of magnetic anisotropy fields or saturation magnetization does not yield a satisfactory agreement with the experimental data, illustrating the model is incomplete without considering the contribution from exchange coupling field.

[5] The data was taken by Prof. Haibin Zhao's group in Fudan University.

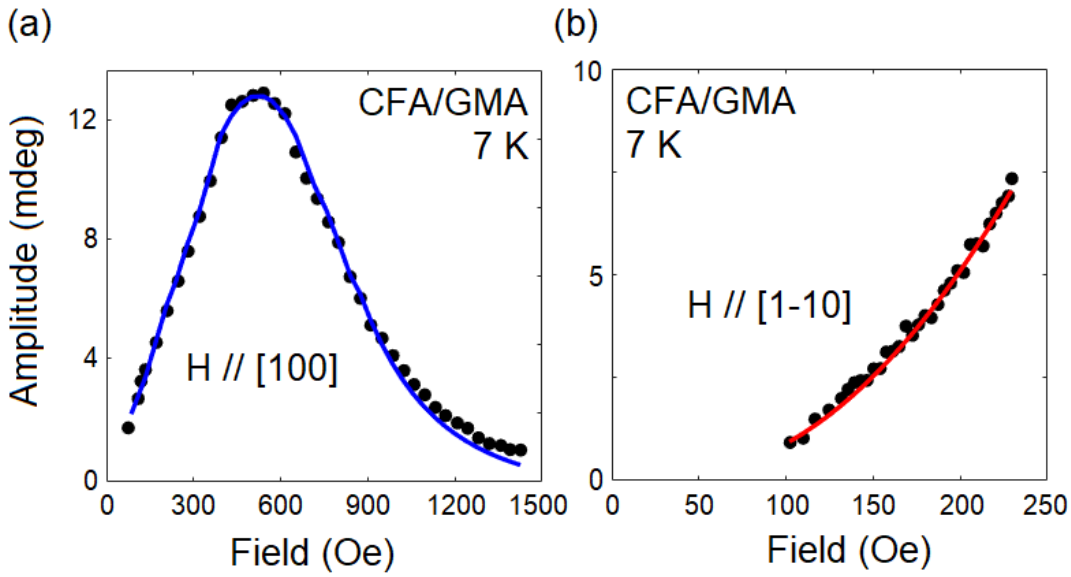

Figure 3.12 Precession amplitude as a function of the applied magnetic field for [100] (top) and [1-10] direction (bottom), respectively. The black points show the experimental result. The blue and red lines represent fits.

In order to investigate the origin of the high-efficiency excitation mechanism, the spin precession frequency and amplitude from 7 K to 300 K are simulated. Figure 3.13 presents the fitting result for the precession frequency when external field applies along the [100] direction. The blue stars show the frequency obtained from the experimental data while the red lines indicate the simulation curve. The curves of the field-dependent precession frequency from 7 K to 300 K are well modelled by LLG equation. The simulated parameters, including magnetic anisotropy constants, the effective magnetization, the exchange coupling stiffness and the modulation of the exchange coupling field, are summarized in Table 3.1.

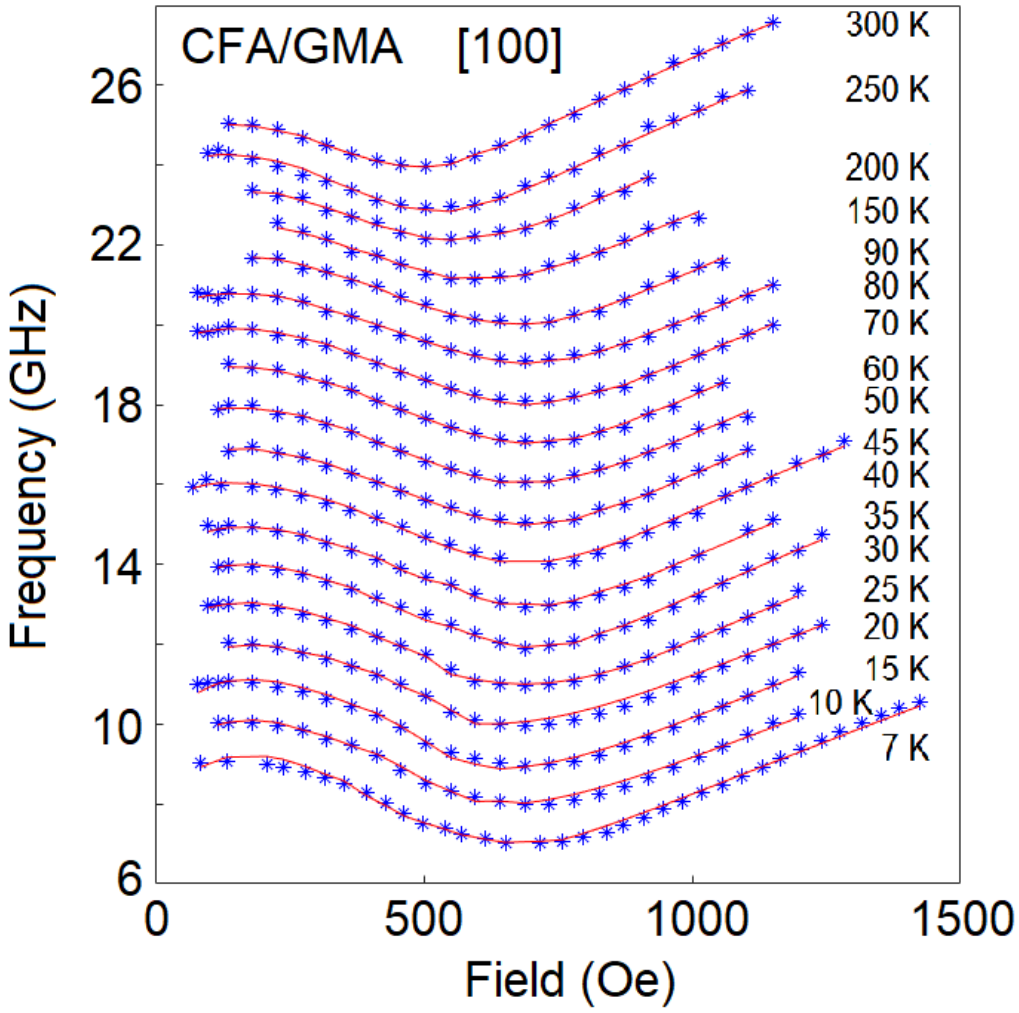

Figure 3.13 Field dependence of magnetization precession frequency at temperatures from 7 K to 300 K. Blue stars present experimental results. Red curves indicate fitting results from LLG equation[6].

Table 3.1 Magnetic anisotropy constants, effective magnetization, exchange coupling constant and modulation of exchange coupling fields simulated from TRMOKE result on the Co_2FeAl/(Ga,Mn)As bilayers.

[6] The data was taken by Prof. Haibin Zhao's group in Fudan University.

T (K)	J_{ex} (erg/cm^3)	K_{ud} (erg/cm^3)	K_{ra} (erg/cm^3)	K_1 (erg/cm^3)	K_u (erg/cm^3)	M_{eff} (emu/cm^3)	M_s (emu/cm^3)	ΔJ_1	ΔK_{ud}
7	326,056	155,000	30,000	290,000	0	880	1,127	20%	6%
10	279,212	150,000	30,000	290,000	10,000	880	1,129	19.50%	6%
15	264,963	150,000	30,000	290,000	0	920	1,124	18%	6%
20	249,886	160,000	15,000	290,000	0	910	1,126	16%	6%
25	255,190	120,000	10,000	300,000	0	910	1,130	16.50%	6%
30	245,125	130,000	10,000	290,000	10,000	950	1,126	14%	5%
35	255,190	120,000	10,000	290,000	0	910	1,126	13%	5%
40	235,824	100,000	5,000	290,000	10,000	950	1,122	11%	5%
45	221,333	100,000	5,000	290,000	10,000	90	1,134	11%	4.50%
50	241,276	100,000	5,000	290,000	10,000	920	1,129	12.50%	5.50%
60	238,560	80,000	0	300,000	10,000	910	1,131	11%	3.50%
70	238,560	80,000	0	300,000	10,000	900	1,130	10%	3%
80	247,800	90,000	0	290,000	10,000	880	1,122	9.5%	3.50%
90	228,850	80,000	0	280,000	10,000	910	1,128	8%	3%
150	209,937	65,000	0	250,000	10000	910	1,131	7.5%	0.50%
200	159,920	80,000	0	220,000	0	980	1,134	4%	0%
250	179,946	60,000	0	220,000	0	920	1,140	5.50%	0%
300	144,957	65,000	0	190,000	0	950	1,136	5%	1%

Figure 3.14 exhibits the temperature dependence of the magnetic parameters given in Tab. 3.1. The red vertical line indicates the Curie temperature T_c of the (Ga,Mn)As layer. As a result, one can see the change of the equilibrium direction $\Delta\varphi$, induced by modulation of the exchange coupling fields, increases rapidly as temperature falls below T_c

(Fig. 3.14 (b). This agrees well with the temperature dependence of the precession amplitude (Fig. 3.11 (d)). The temperature dependence of K_1 is induced by the Co2FeAl layer. The exchange-coupling term J_{ex} and the unidirectional field K_{ud} increase considerably with decreasing temperature, while the anisotropy fields and the saturation magnetization remain unchanged below T_c (Fig. 3.11 (h)). This is consistent with the fact that when the temperature is below 50 K, a strong exchange-coupling effect arises between the two ferromagnetic orders in the Co_2FeAl/(Ga,Mn)As bilayer [42]. In contrast, it is quite different for the case in single Co_2FeAl film where we attribute the magnetization precession excitation mechanism to the ultrafast modification of the magnetic anisotropy field by the laser induced heat effect with applying a much higher pump energy density of 2 mJ/cm^2 [46]. Actually, the Co_2FeAl/(Ga,Mn)As bilayer exhibits very weak temperature dependence of magnetization precession frequency below 50 K, which also proves that the magnetic anisotropy is temperature independent. Hence, we cannot merely use the ultrafast modification of magnetic anisotropy by the heat effect to account for the pronounced increase of precession amplitude. The only way that the (Ga,Mn)As layer can influence the spin dynamics in the Co_2FeAl layer is through altering the exchange-coupling strength J_1. Therefore, the origin of this efficient excitation mechanism with low-power pump pulses is the modulation of J_1.

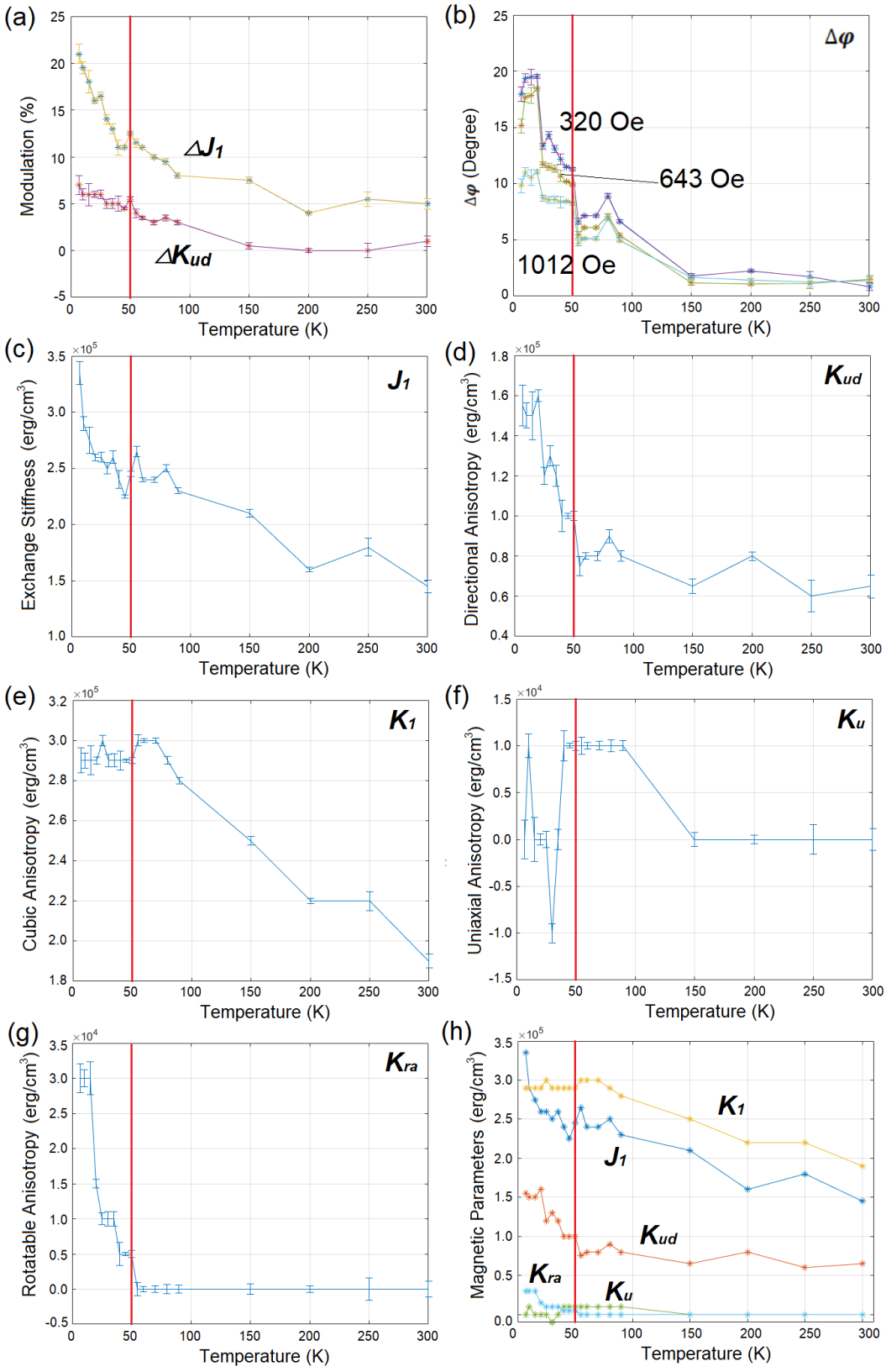
(a)
Modulation (%)
ΔJ1
ΔKud
Temperature (K)
(b)
Δφ
Δφ (Degree)
320 Oe
643 Oe
1012 Oe
Temperature (K)
(c)
J1
Exchange Stiffness (erg/cm3)
Temperature (K)
(d)
Kud
Directional Anisotropy (erg/cm3)
Temperature (K)
(e)
K1
Cubic Anisotropy (erg/cm3)
Temperature (K)
(f)
Ku
Uniaxial Anisotropy (erg/cm3)
Temperature (K)
(g)
Kra
Rotatable Anisotropy (erg/cm3)
Temperature (K)
(h)
Magnetic Parameters (erg/cm3)
K1
J1
Kud
Kra
Ku
Temperature (K)

Figure 3.14 (a)-(g) Temperature dependence of modulation of exchange coupling fields, angle change of equilibrium direction, exchange coupling stiffness, unidirectional anisotropy, cubic anisotropy, uniaxial anisotropy and rotatable anisotropy. (h) Comparison of temperature dependence of exchange coupling fields and anisotropy fields.

In the following, we discuss the observed optical excitation mechanism of coherent spin precession in the ferromagnetic-coupled bilayer under applied magnetic field, which can be attributed to photo-enhanced interfacial exchange interactions. Since the temperature dependence of the precession amplitude $\boldsymbol{A}$ (Fig. 3.11 (d)) follows the same trend as the increase of magnetization, we do think the photo-enhanced ferromagnetism in the (Ga,Mn)As layer contributes directly to the high-efficient excitation of coherent spin precession. However, this contribution may be small to the modulation of interfacial exchange coupling strength $\boldsymbol{J_1}$. According to our simulation, the increase of magnetization is less than 1% because it is already close to saturation. This is consistent with Wang et al's result [30]. Apparently, the limited enhanced ferromagnetism (~ 1%) can barely trigger the noticeable increase (~ 20%) in $\boldsymbol{J_1}$ directly. The origin of the significantly enhanced excitation needs to be further elucidated.

At temperatures below $\boldsymbol{T_c}$ = 50 K, the low-fluence, near-infrared pump-light excitation creates a nonequilibrium distribution of spin-unpolarized charge carriers in the exchange-coupled bilayer under applied

magnetic field. At first, a fast demagnetization process occurs (the initial dip shown in Fig. 3.6), because the optically generated hot charge carriers will undergo rapid spin-flip scattering with the local magnetic moments in the bilayer and acquire their spin polarization. In the meantime, efficient carrier-phonon scattering (optical phonon energy ~36 meV) causes a rapid termination of the demagnetization process as the hot carrier distribution quickly loses its energy. At extended time delays, the hole-mediated ferromagnetic ordering process takes place as the optically generated, thermalized holes populate the spin-split bands of the (Ga,Mn)As layer [31]. These additional holes cause an increase of macroscopic magnetization as they polarize the Mn spins via enhanced Mn-Mn exchange correlation due to the diagonal elements of the mean-field exchange Hamiltonian $\boldsymbol{H_{p\text{-}d}}$ ($\sim \boldsymbol{J_{pd}}\, \boldsymbol{S_z \cdot s_z}$), while the optically generated electrons contribute very little to the transient enhancement of magnetization, because their lifetime is too short [31]. As Fe(Co) spins and Mn spins precess along their own equilibrium directions, one moving magnetization pumps a spin current out of the ferromagnet, carrying angular momentum perpendicular to the magnetization direction. The ejected spin angular momentum can either scatter back or be absorbed by the adjacent ferromagnetic layer. In the former case, the magnetization dynamics are not affected. In the latter case, the two ferromagnets become coupled by an exchange of itinerant spins, which may result in collective excitation modes [48]. By conservation

of spin angular momentum, the ejected spins exert a relaxation torque on the precessing magnetization in the adjacent ferromagnet that turns it towards the magnetization direction in the first ferromagnet in order to stabilize the parallel configuration even without the presence of charge current [48-52]. As a consequence, the interfacial exchange interaction gets enhanced by dynamic exchange coupling. Rather than the limited modulation of the static exchange coupling effect, the emergence of the dynamic exchange coupling interaction is likely the origin of the 20% increase in the interfacial exchange-coupling strength. Therefore, we can attribute the high-efficient excitation of coherent spin precession to the emergence of dynamic exchange coupling field.

At temperatures above T_c = 50 K, the ferromagnetic ordering in the (Ga,Mn)As layer is almost vanished, but the spin precession can still be excited in the Co_2FeAl/(Ga,Mn)As bilayer with oscillation amplitude 3-4 times larger than the spin precession signal in the sample without the (Ga,Mn)As layer. The magnetization precession amplitude *A* exhibits very little variation with temperature up to 300 K (Fig. 3.11(d)). Nie and coworkers have shown that even above the Curie temperature of (Ga,Mn)As, the Mn spins in a 2.11-nm thick interfacial layer remain spin polarized up to 300 K and FM exchange-coupled to the Co_2FeAl layer via the magnetic proximity effect [42]. When photoexcited, these interface spins in (Ga,Mn)As are strongly modulated by Fe(Co) spins and thus

produce the magnetic torque on the Co_2FeAl layer, driving its magnetization precession. This finding may provide a viable pathway for designing semiconductor spintronic devices for ultrafast, low-power spin manipulation at room temperature through magnetic proximity effect.

Reference:

[1] Lambert C-H, et al. All-optical control of ferromagnetic thin films and nanostructures. Science 345, 1337 (2014).

[2] Le Guyader L, et al. Nanoscale sub-100 picosecond all-optical magnetization switching in GdFeCo microstructures. Nat. Commun. 6, 5839 (2015).

[3] Rudolf D, et al. Ultrafast magnetization enhancement in metallic multilayers driven by superdiffusive spin current. Nat. Commun. 3, 1037 (2012).

[4] Choi G-M, Min B-C, Lee K-J, Cahill DG. Spin current generated by thermally driven ultrafast demagnetization. Nat. Commun. 5, 4334 (2014).

[5] Nemec P, et al. Experimental observation of the optical spin transfer torque. Nat. Phys. 8, 411-415 (2012).

[6] Tesarova N, et al. Experimental observation of the optical spin-orbit torque. Nat. Photon. 7, 492-498 (2013).

[7] Jun-Yang C, et al. Time-resolved magneto-optical Kerr effect of magnetic thin films for ultrafast thermal characterization. J. Phys. Chem. Lett. 7.13: 2328-2332 (2016).

[8] El Hadri, M. S., et al. Electrical characterization of all-optical helicity-dependent switching in ferromagnetic Hall crosses. Appl. Phys. Lett. 108.9: 092405 (2016).

[9] Jun-Yang C, et al. All-optical switching of magnetic tunnel junctions with single subpicosecond laser pulses. Phys. Rev. Applied 7.2: 021001 (2017).

[10] Mentink J H. Manipulating magnetism by ultrafast control of the exchange interaction. J. Phys.: Condens. Matter 29, 453001 (2017).

[11] Kirilyuk A, Kimel A V, Rasing T. Ultrafast optical manipulation of magnetic order. Rev. Mod. Phys. 82, 2731 (2010).

[12] Hashimoto Y, et al. Photoinduced Precession of Magnetization in Ferromagnetic (Ga,Mn)As. Phys. Rev. Lett. 100, 067202 (2008).

[13] Radu I, et al. Transient ferromagnetic-like state mediating ultrafast reversal of antiferromagnetically coupled spins. Nature 472, 205 (2011).

[14] Mathias S, et al. Probing the timescale of the exchange interaction in a ferromagnetic alloy. Proc. Natl. Acad. Sci. 109, 4792 (2012).

[15] Stupakiewicz A, et al. Ultrafast nonthermal photomagnetic recording in a transparent medium. Nature 542, 71 (2017).

[16] Mikhaylovskiy R V, et al. Ultrafast optical modification of exchange interactions in iron oxides. Nat Commun. 6, 8190 (2015).

[17] Ma X, et al. Ultrafast spin exchange-coupling torque via photo-excited charge-transfer processes. Nat. Commun. 6, 8800 (2015).

[18] Fan Y, et al. Photoinduced spin angular momentum transfer into an antiferromagnetic insulator. Physical Review B 89, 094428 (2014).

[19] Matsubara M, et al. Ultrafast optical tuning of ferromagnetism via the carrier density. Nature Commun. 6, 6724 (2015).

[20] Galanakis, I., Ph Mavropoulos, and P. H. Dederichs. "Introduction to half-metallic Heusler alloys: electronic structure and magnetic properties." *arXiv preprint cond-mat/0510276* (2005).

[21] Kandpal, Hem C., Gerhard H. Fecher, and Claudia Felser. "Calculated electronic and magnetic properties of the half-metallic, transition metal based Heusler compounds." *Journal of Physics D: Applied Physics* 40.6 (2007): 1507.

[22] Wolf, S. A., et al. "Spintronics: a spin-based electronics vision for the future." *science* 294.5546 (2001): 1488-1495.

[23] Trudel, Simon, et al. "Magnetic anisotropy, exchange and damping in cobalt-based full-Heusler compounds: an experimental review." *Journal of Physics D: Applied Physics*43.19 (2010): 193001.

[24] Heusler F. (1903). "Über magnetische Manganlegierungen". Verhandlungen der Deutschen Physikalischen Gesellschaft (in German). 12: 219.

[25] Webster, P. J. "Magnetic and chemical order in Heusler alloys containing cobalt and manganese." *Journal of Physics and Chemistry of Solids* 32.6 (1971): 1221-1231.

[26] Chen, Lin, and Jianhua Zhao. "Magneto-Transport Behaviors of (Ga, Mn) As Based Nano-structures and Devices." *Handbook of Spintronics* (2016): 585-614.

[27] Zhu, Yonggang, et al. "Ultrafast dynamics of four-state magnetization reversal in (Ga, Mn) As." *Applied Physics Letters* 95.5 (2009): 052108.

[28] Dietl, Tomasz, et al. "Zener model description of ferromagnetism in zinc-blende magnetic semiconductors." *science* 287.5455 (2000): 1019-1022.

[29] Lee, Sanghoon, et al. "Ferromagnetic semiconductor GaMnAs." *Materials Today* 12.4 (2009): 14-21.

[30] Wang J, et al. Ultrafast Enhancement of Ferromagnetism via Photoexcited Holes in GaMnAs. Phys. Rev. Lett. 98, 217401 (2007).

[31] Wang J, et al. Memory effects in photoinduced femtosecond magnetization rotation in ferromagnetic GaMnAs. Appl. Phys. Lett. 94, 021101 (2009).

[32] Ohno, H., et al. "Electric-field control of ferromagnetism." *Nature* 408.6815 (2000): 944.

[33] Sawicki, Maciej, et al. "Experimental probing of the interplay between ferromagnetism and localization in (Ga, Mn) As." *Nature Physics* 6.1 (2010): 22.

[34] Hall K C, et al. Ultrafast optical control of coercivity in GaMnAs. Appl. Phys. Lett. 93, 032504 (2008).

[34] Astakhov G V, et al. Magnetization manipulation in (Ga,Mn)As by subpicosecond optical excitation. Appl. Phys. Lett. 86, 152506 (2005).

[35] Zhu Y G, et al. Ultrafast dynamics of four-state magnetization reversal in (Ga,Mn) As. Appl. Phys. Lett. 95, 052108 (2009).

[36] Maccherozzi, F., et al. "Evidence for a magnetic proximity effect up to room temperature at Fe/(Ga, Mn) As interfaces." *Physical review letters* 101.26 (2008): 267201.

[37] Sperl, Matthias, et al. "Identifying the character of ferromagnetic Mn in epitaxial Fe/(Ga, Mn) As heterostructures." *Physical Review B* 81.3 (2010): 035211.

[38] Sperl, Matthias, et al. "Reorientation transition of the magnetic proximity polarization in Fe/(Ga, Mn) As bilayers." *Physical Review B* 85.18 (2012): 184428.

[39] Alsmadi, A. M., et al. "Interfacial exchange coupling in fe/(ga, mn) as bilayers." *Physical Review B* 89.22 (2014): 224409.

[40] Tivakornsasithorn, Kritsanu, et al. "Interlayer Exchange Coupling Between Fe and GaMnAs Ferromagnetic Semiconductor." *IEEE Transactions on Magnetics* 99 (2018): 1-4.

[41] Tivakornsasithorn, Kritsanu, et al. "Magnetization reversal and interlayer exchange coupling in ferromagnetic metal/semiconductor Fe/GaMnAs hybrid bilayers." *Scientific reports* 8.1 (2018): 10570.

[42] Nie, S. H., et al. "Ferromagnetic interfacial interaction and the proximity effect in a Co 2 FeAl/(Ga, Mn) As bilayer." *Physical review letters* 111.2 (2013): 027203.

[43] Qi, J., et al. "Ultrafast laser-induced coherent spin dynamics in ferromagnetic Ga 1− x Mn x As/GaAs structures." *Physical Review B* 79.8 (2009): 085304.

[44] Patz, Aaron, et al. "Ultrafast probes of nonequilibrium hole spin relaxation in the ferromagnetic semiconductor GaMnAs." *Physical Review B* 91.15 (2015): 155108.

[45] Koshihara, S., et al. "Ferromagnetic order induced by photogenerated carriers in magnetic III-V semiconductor heterostructures of (In, Mn) As/GaSb." *Physical review letters*78.24 (1997): 4617.

[46] Yuan, H. C., et al. "Different temperature scaling of strain-induced magneto-crystalline anisotropy and Gilbert damping in Co_2FeAl film epitaxied on GaAs." *Applied Physics Letters*105.7 (2014): 072413.

[47] Stiles, Mark D., and Robert D. McMichael. "Model for exchange bias in polycrystalline ferromagnet-antiferromagnet bilayers." *Physical Review B* 59.5 (1999): 3722.

[48] Tserkovnyak, Yaroslav, Arne Brataas, and Gerrit EW Bauer. "Dynamic exchange coupling and Gilbert damping in magnetic multilayers." *Journal of applied physics* 93.10 (2003): 7534-7538.

[49] Heinrich, B., et al. "Role of dynamic exchange coupling in magnetic relaxations of metallic multilayer films." *Journal of applied physics* 93.10 (2003): 7545-7550.

[50] Heinrich, Bret, et al. "Dynamic exchange coupling in magnetic bilayers." *Physical review letters* 90.18 (2003): 187601.

[51] Tserkovnyak, Yaroslav, Arne Brataas, and Gerrit EW Bauer. "Spin pumping and magnetization dynamics in metallic multilayers." *Physical Review B* 66.22 (2002): 224403.

[52] Myers, E. B., et al. "Current-induced switching of domains in magnetic multilayer devices." *Science* 285.5429 (1999): 867-870.

Chapter 4

Gilbert Damping Properties in Co_2FeAl/(Ga,Mn)As

In this chapter, the magnetic damping behavior in the Co_2FeAl/(Ga,Mn)As bilayer heterostructures is investigated. The magnetization dynamics in both ferromagnetic layers is modulated by the dynamic exchange coupling interaction through spin-pumping (SP) effect. Section 4.1 introduces recent works on SP effect. Section 4.2 presents the photo-enhanced Gilbert damping effect in the Co_2FeAl/(Ga,Mn)As bilayer system. The dynamic exchange coupling interaction is discussed in Section 4.3. Section 4.4 investigates the phase-shift of the magnetization precession induced by the dynamic exchange coupling effect.

4.1 Introduction

There has been growing interest in ultrafast optical magnetic dynamics in low-dimensional ferromagnetic heterostructures due to its potential applications in advanced functional spintronic devices. The spin-pumping (SP) effect, in which a ferromagnetic layer with magnetization precession creates and injects a flow of angular momentum without

accompanying a charge current into the adjacent material, which is typically a nonmagnetic metallic layer, brings a new mechanism for controlling spin and hence plays an important role in the design of future spintronic devices [1]. Since Heinrich, B. *et al* first reported spin-pumping effect as an increased damping of the source layer in ferromagnetic resonance (FMR) experiments [2], a number of FMR experiments on SP effect have been performed on transition-metal multilayers [3-6], topological insulators [7-8] and semiconductors [9-11]. Besides, Danilov A. et al demonstrated optically that the mutual SP effect modifies the precession dynamics in a pseudo spin-valve by simultaneously exciting magnetization precession in two magnetic layers with femtosecond laser pulses [12]. However, there has not been any SP effect reported yet when it comes to the combination of a Heusler alloy and a ferromagnetic semiconductor. As an important ferromagnetic semiconductor material, (Ga,Mn)As exhibits high spin polarization and noticeable conductivity which is attractive for spintronic applications. The SP effect in ferromagnetic semiconductor/metal heterostructures provides a promising route of ultrafast low-power spin manipulation and hence attracts high interest.

4.2 Photo-enhanced Gilbert Damping

The TRMOKE measurement are performed on the Co_2FeAl/(Ga,Mn)As bilayer heterostructures below the Curie temperature ***Tc*** = 50 K. Figure 4.1 (a) and (c) display the TRMOKE data at 10 K and 25 K, respectively, with an in-plane magnetic field applied along the intermediate axis [100]. The precession signal can be well fitted by Eq. 3.2, as shown by the red curves. One can see that the magnetization precession decays with different relaxation times for different applied magnetic fields. The fastest decay of the oscillation occurs at the external magnetic field of 458 Oe at 10 K and 550 Oe at 25 K, indicating an interlayer dynamic coupling effect may occur between the magnetization precession in the Co_2FeAl layer and the (Ga,Mn)As layer. Furthermore, a shift of fastest decay in relation to the magnetic field is observed when the temperature increases from 10 K to 25 K. This will be discussed below. Figures 4.1 (b) and (d) exhibit the Fast Fourier Transform (FFT) analysis at 10 K and 25 K corresponding to the TRMOKE data shown in Figs. 4.1 (a) and (c), respectively. Due to the fast decay of the spin precession in the (Ga,Mn)As layer as discussed in Chapter 3, we can extract only one frequency from FFT analysis, which is arising from the Co_2FeAl layer.

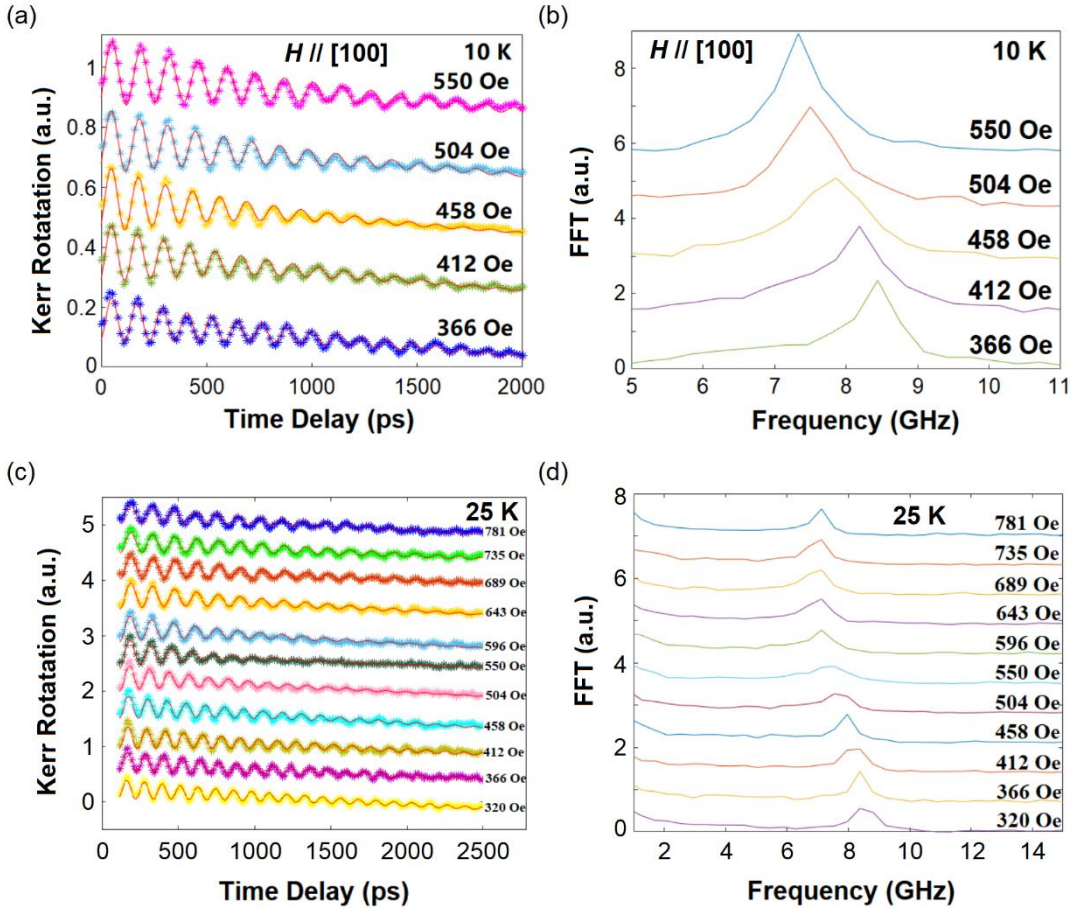

Figure 4.1 (a) TRMOKE data of Co_2FeAl/(Ga,Mn)As bilayer at 10 K with applied magnetic field from 366 Oe to 550 Oe. (b) FFT analysis for magnetization precession frequency at 10 K. (c) TRMOKE data at 25 K with applied magnetic field from 320 Oe to 781 Oe. (d) FFT analysis for magnetization precession frequency at 25 K[7].

The magnetization dynamics in the Co_2FeAl/(Ga,Mn)As bilayer system is described by a modified Landau-Lifshitz-Gilbert (LLG) equation with an additional spin torque term:

[7] The data was taken by Prof. Haibin Zhao's group in Fudan University.

$$\frac{dm}{dt} = -\gamma \boldsymbol{m} \times \boldsymbol{H_{eff}} + \alpha_0 \boldsymbol{m} \times \frac{dm}{dt} + \alpha_{sp}\left(\boldsymbol{m} \times \frac{dm}{dt} - \boldsymbol{m'} \times \frac{dm'}{dt}\right), \qquad (4.1)$$

where $\boldsymbol{m}$ is the magnetization of the Co_2FeAl layer, γ is the gyromagnetic ratio, α_0 is the intrinsic Gilbert damping constant, and $\boldsymbol{H_{eff}}$ is the effective magnetic field in the Co_2FeAl layer determined by the external magnetic field, the demagnetization field, the anisotropy field, and the exchange-coupling field. The last term describes the spin torque which acts on both layers as a bidirectional effect. Here $\boldsymbol{m'}$ denotes the magnetization of the (Ga,Mn)As layer, and α_{sp} represents the contribution of spin pumping effect to the damping.

By analyzing the TRMOKE data with LLG equation, we notice a strong enhancement of the effective Gilbert damping as a function of the external magnetic field, as seen in Fig. 4.2. Here the effective Gilbert damping is calculated from the fitted anisotropy parameters and the lifetime of the spin waves, using

$$\alpha = 2/[\tau\gamma(2H\cos(\varphi_M - \varphi_H) + H_a + H_b)],$$

where φ_M and φ_H are the angles of magnetization and applied field. The damping of the magnetization precession is most pronounced for a field of 458 Oe at 10 K (Fig. 4.1(a)). Below the Curie temperature $\boldsymbol{Tc}$ = 50 K of (Ga,Mn)As, the effective damping peak shifts from 450 Oe to 650 Oe when the temperature increases from 10 K to 40 K, then it disappears at Tc (Fig.

4.2). The most pronounced damping peak occurs at 25 K compared to the other temperatures. The temperature-dependent measurement clearly exhibits that the damping peak arises only at the presence of ferromagnetism in (Ga,Mn)As layer. This implies that the ferromagnetically aligned spins in the semiconductor layer must be taken into consideration for the enhanced damping below ***Tc*** = 50 K. Furthermore, at 10 K the damping of the magnetization precession reaches the highest value at an applied field of 458 Oe, where the FFT analysis exhibits the broadest peak (Fig. 4.1 (b)). This further suggests that the precession dynamics of the Co_2FeAl layer and the (Ga,Mn)As layer are coupled near the appearance of the damping peak.

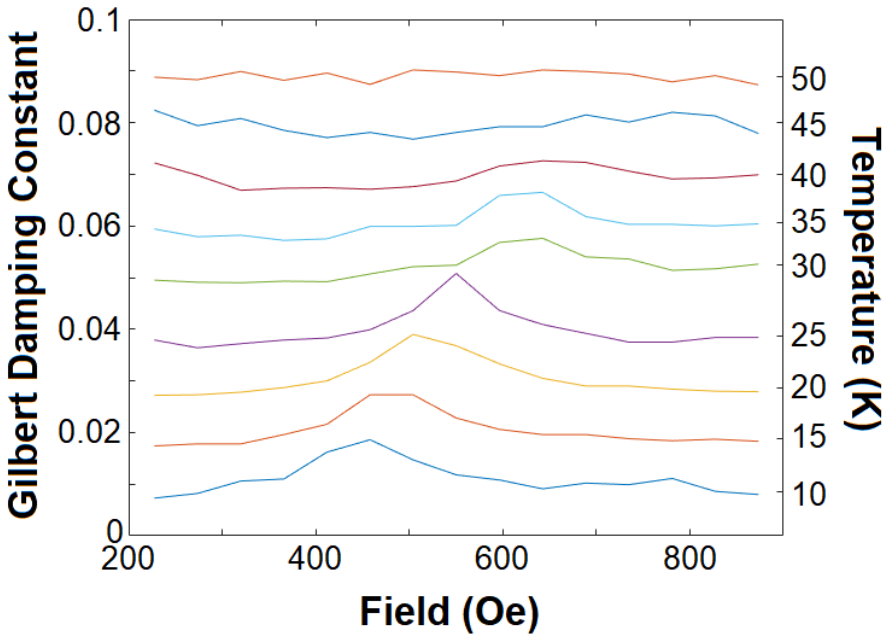

Figure 4.2 Effective Gilbert damping constant as a function of external applied field at temperatures from 10 K to 50 K.

4.3 Dynamic exchange interaction in Co_2FeAl/(Ga,Mn)As

We attribute the effective Gilbert damping peak to the “dynamic exchange coupling” between the precessing magnetization in the Co_2FeAl layer and the (Ga,Mn)As layer, as illustrated in Fig. 4.3. At the temperature below ***Tc*** = 50 K of the (Ga,Mn)As layer, the ultrafast pump excitation induces a sudden change in the direction of the effective field by modulating the strength of the exchange coupling effect, leading to a photoexcited exchange-coupling torque $\Delta\boldsymbol{\tau}_{\mathrm{ex}}(t)$ which acts on both Fe(Co) spins and Mn spins. The magnetization in both ferromagnetic layers are suddenly pulled towards each other and then start to precess with opposite angular momentum (one is clockwise and the other is anticlockwise) along their own equilibrium directions, as shown in Fig. 4.3. At a certain intensity of the applied field, the magnetization in the Co_2FeAl layer precesses at the same frequency as that in the (Ga,Mn)As layer (***f*** $_{CFA}$ = ***f*** $_{GMA}$). At this point, the precessing magnetization in one ferromagnet is expected to “pump” a spin current ***I*** $_i$ into the adjacent ferromagnet which can be seen as a spin sink. As a consequence, the magnetization precession in the first ferromagnetic layer loses some of the spin angular momentum due to the conservation of angular momentum, leading to an enhancement of the Gilbert damping constant. On the other hand, the outgoing spin current ***I*** $_i$ is absorbed by the second ferromagnet, exerting a torque onto the precessing magnetization in this layer and thereby influences its

precession as well, as shown in Fig. 4.3. The exchange coupling interaction, which only occurs between the magnetization precessions in two ferromagnets, is called “dynamic” exchange coupling interaction.

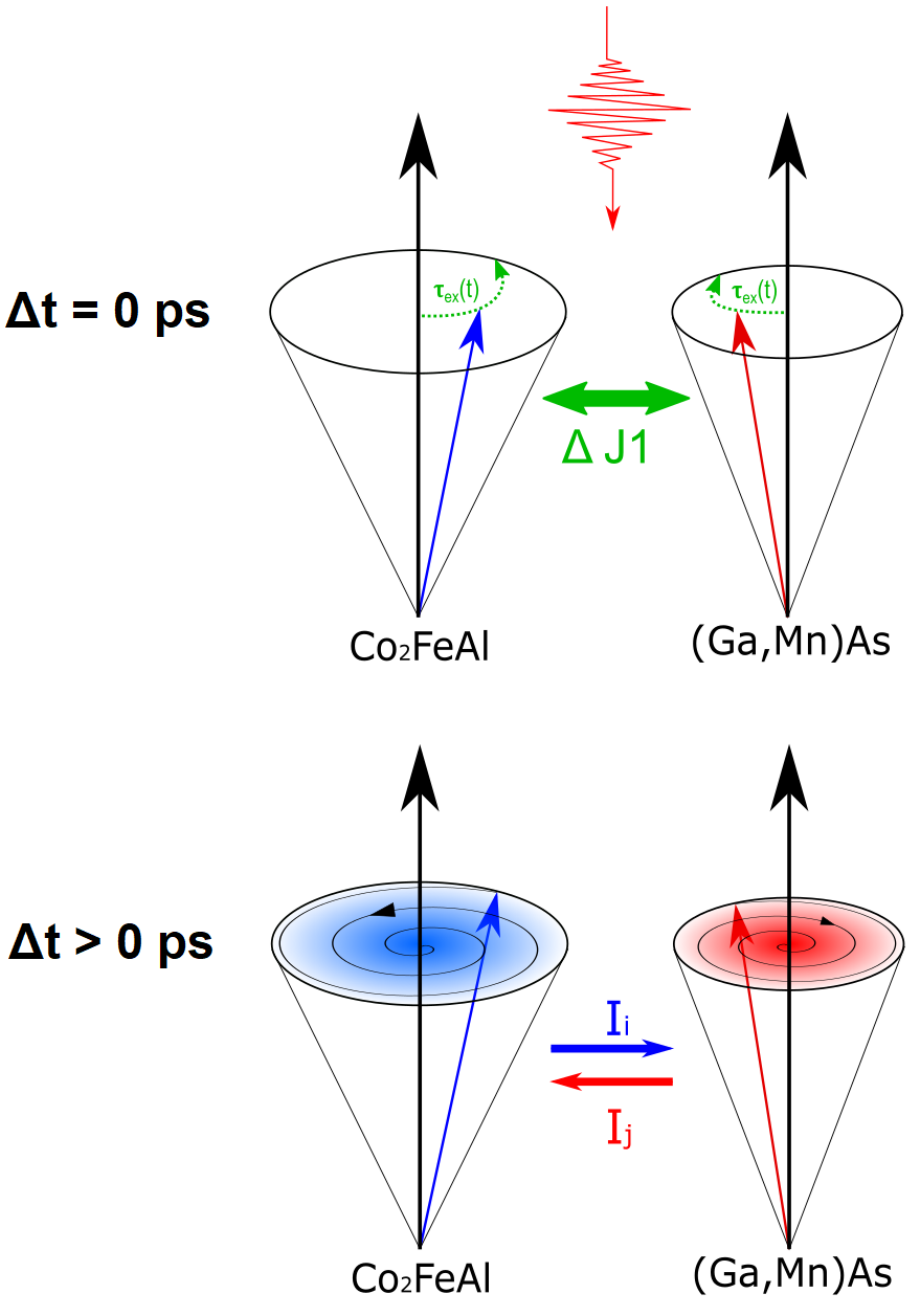

Figure 4.3 Illustration of photo-excited exchange-coupling torque and dynamic exchange coupling mode.

Typically, the reversed spin current leads to an “anti-damping term” if the magnetization in both ferromagnets precesses at the same frequency $f_{CFA} = f_{GMA}$ with the same angular momentum, as reported in many FMR experiments on the ferromagnetic multilayers [2, 13-14]. However, in our case, the magnetization in both ferromagnetic layers precesses with the opposite angular momentum at the same frequency $f_{CFA} = f_{GMA}$, leading to an increase of the damping in the spin sink layer. As a result, both magnetization precessions are strongly damped at the resonance frequency due to the dynamic exchange coupling effect. Furthermore, in this coupled mode, the pumped spin current between the coupled precessions is probably a bidirectional effect. According to B. Heinrich et al’s theoretical work [2], there is also a spin current I_j injected into the first ferromagnetic layer from the second one. That means both ferromagnets can be seen as mutual spin pumps and spin sinks. But in our case, the magnetization precession in the Co_2FeAl layer is more significant than in the (Ga,Mn)As layer, and hence the impact of the spin currents on the magnetization precession is more pronounced in the ferromagnetic semiconductor layer, where a fast decay of magnetization precession is expected to occur. This may explain the absence of the magnetization precession signal of the (Ga,Mn)As layer in the TRMOKE result.

In order to investigate the dynamic exchange-coupling effect at the interfacial layer, we look into the precession frequency behavior of the Co_2FeAl/(Ga,Mn)As bilayer around the resonance field, i.e., where the strongest damping occurs. We performed an approximation of the magnetization precession frequency for the (Ga,Mn)As layer so that the precession frequency from both ferromagnets can be compared. The strength of the external applied magnetic field that triggers the strongest damping indicates where the two magnetizations precess at the same frequency. In other words, the precession frequency in the (Ga,Mn)As layer is known at these fields. By projecting the precession frequency of the Mn spins from one temperature onto another temperature at the same intensity of the applied magnetic field, the precession frequency in the (Ga,Mn)As layer at the new temperature can be approximated, as demonstrated in Figure 4.4.

Figure 4.5 shows the observed precession frequency of the Co_2FeAl layer (blue curves), while the field-dependence of the precession frequency of the (Ga,Mn)As layer (red curves) is approximated by projecting the precession frequency of the Mn spins at all other temperatures onto a certain temperature below ***Tc***. As the temperature increases to ***Tc*** = 50 K, the damping resonance peak shifts to higher field, which may be due to a decrease of the interfacial exchange-coupling field and the anisotropy fields in the (Ga,Mn)As layer. On one hand, the increasing temperature

weakens the ferromagnetism of the (Ga,Mn)As layer and hence reduces the interfacial exchange-coupling effect between the two layers. On the other hand, previous studies have shown that the anisotropy fields are approaching zero with the temperature increasing to ***Tc*** [15]. As a consequence, a more intensive external magnetic field is necessary for the (Ga,Mn)As layer to ensure the precession frequency matches with that of the Co_2FeAl layer, since the contribution from the interfacial exchange-coupling field and the anisotropy fields to the precession frequency becomes reduced as the temperature increases in the (Ga,Mn)As layer. The shift of the damping peak with increasing temperature also can be seen in Fig. 4.2. Furthermore, according to the resonance condition $f_{CFA} = f_{GMA}$, how close the precession frequency of the (Ga,Mn)As layer is to that of the Co_2FeAl layer around the resonance field determines the strength of the dynamic exchange coupling effect and hence significantly influences the formation of the spin current between the two ferromagnetic layers. The spin current induced by the modulation of the interfacial exchange-coupling effect strongly damps the magnetization oscillation in both layers. At temperatures from 20 K to 25 K, the two frequency curves overlap with each other around the resonance field when compared with those at other temperatures where the frequency splitting is clear near the resonance. This is consistent with our observation that the most pronounced damping peak occurs at 25 K as shown in Fig. 4.2. As the temperature increases

close to ***Tc*** = 50 K, the ferromagnetism of the (Ga,Mn)As layer is too weak to support the formation of an effective spin current pumped between the two layers. This explains the absence of the damping peak near the Curie temperature.

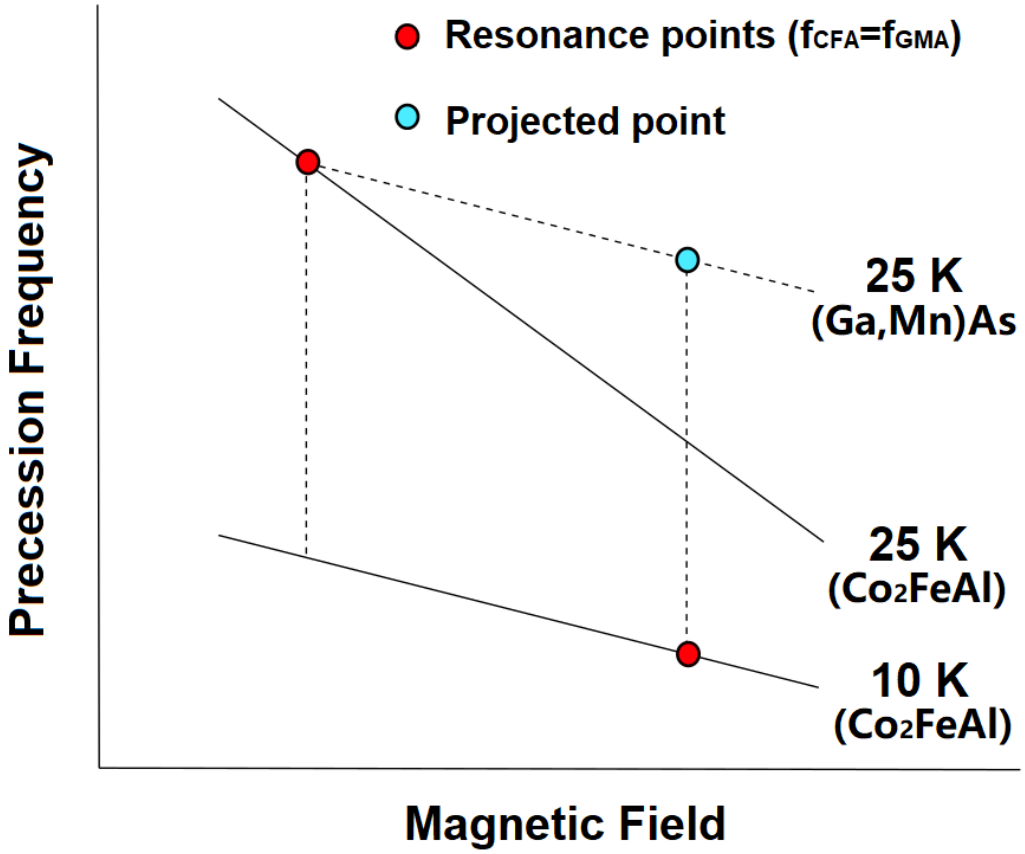

Figure 4.4 Demonstration of approximation of magnetization precession frequency in (Ga,Mn)As layer

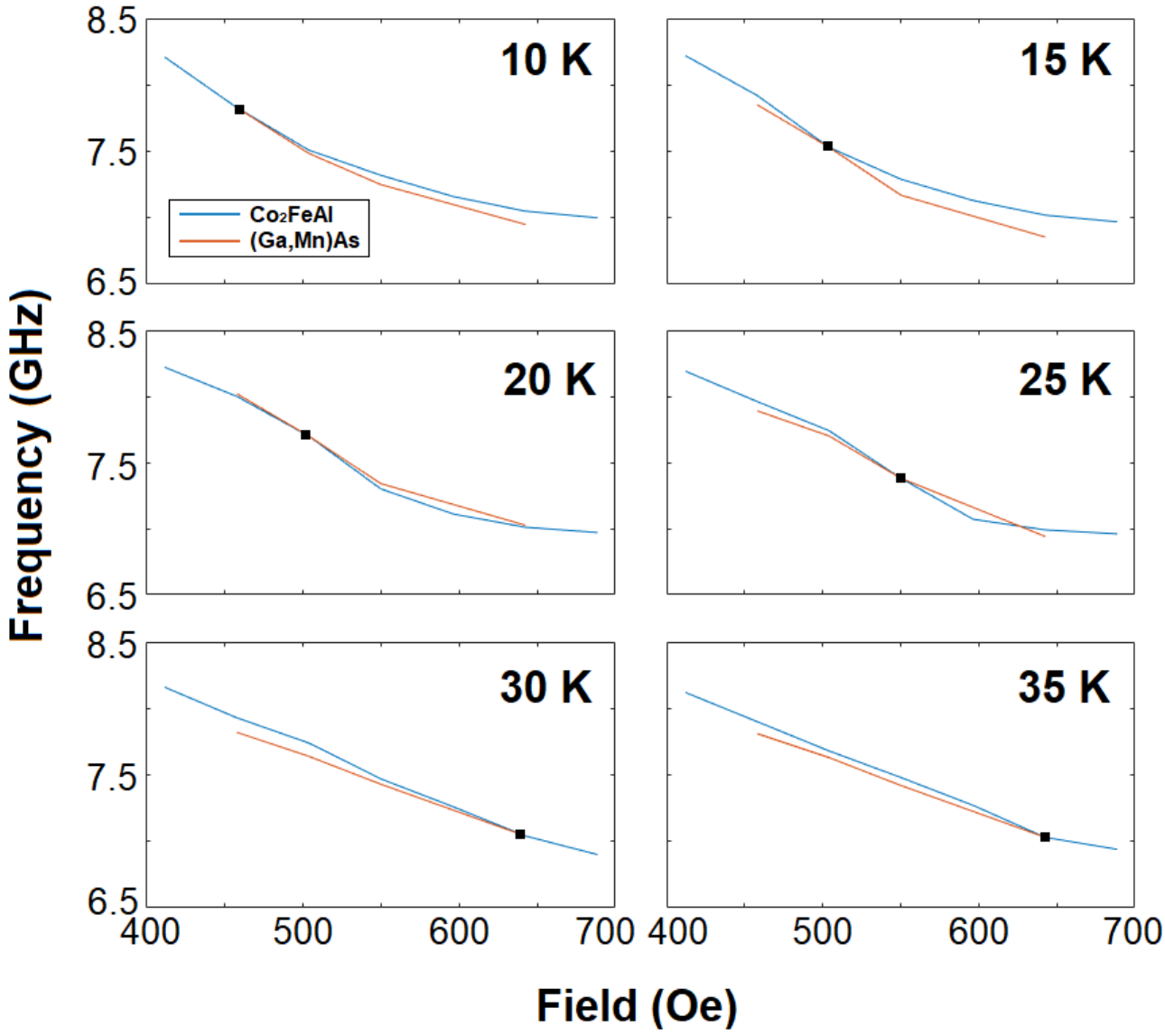

Figure 4.5 Magnetization precession frequency as a function of the external applied field at different temperatures from 10 K to 35 K. The black dot indicates the resonance field at each temperature.

4.4 Phase-Shift of the Magnetization Precession

Under optical pump excitation, the damping of magnetization precession is increased due to the dynamic exchange coupling interaction. In addition to the enhanced Gilbert damping constant, a phase-shift of magnetization precession with respect to the applied magnetic field is also observed. It is difficult to distinguish the phase-shift directly from the TRMOKE signal (Fig. 4.1(a)), because the phase change is relatively small and it is also influenced by the difference in precession frequency. Therefore, we modeled the magnetization precession with Eq. 3.2 and converted the delay time into the phase of precession (x – axis) in order to eliminate the contribution from the difference in precession frequency, as seen in Fig. 4.6. The red straight line indicates the first minimum of precession signal in order to determine the phase-shift.

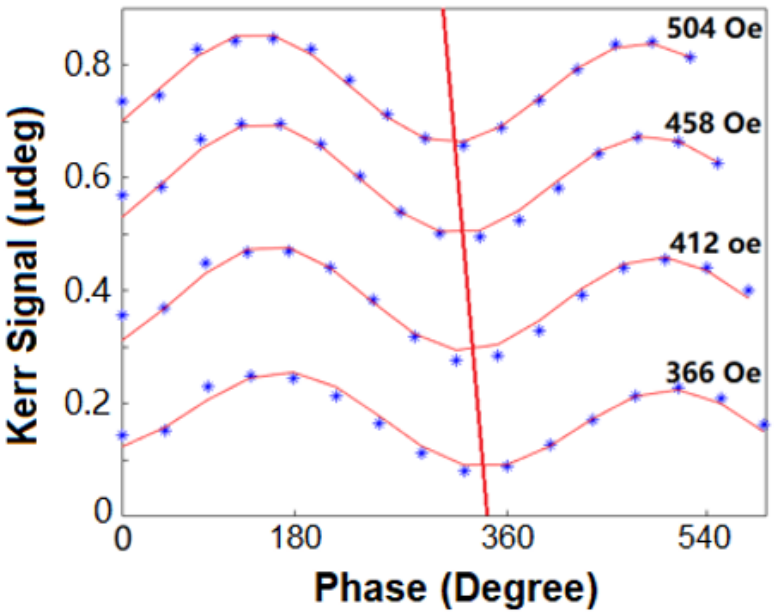

Figure 4.6 TRMOKE data as a function of phase-angle of magnetization precession for different applied fields. The red straight line indicates the phase-shift[8].

Figure 4.7(a) presents the field dependence of the initial phase-angle of magnetization precession. Below the Curie temperature ***Tc*** = 50 K of (Ga,Mn)As layer, the phase of the magnetization precession exhibits a noticeable shift of around 20 degree that moves to higher field as temperature increases from 10 K to 35 K, then the phase-shift disappears near ***Tc*** = 50 K, which is similar to the temperature-dependent behavior of the photo-enhanced damping peak. Furthermore, the phase-shift occurs across a range of around 200 Oe which overlaps well with the damping peak, as seen in Fig. 4.7(b). This suggests that the phase-shift may be induced by the dynamic exchange-coupling effect between the Co_2FeAl layer and the (Ga,Mn)As layer. Several research groups have reported a much larger phase-shift (nearly 180°) due to spin-pumping effect in ferromagnetic/nonmagnetic metallic/ferromagnetic heterostructures in FMR experiments [7, 16-19]. The phase behavior was attributed to the change in orientation of the torque from that of the RF-field torque to the total torque due to the spin current [17]. However, in our case, the observed phase-shift is relatively small (20 degree) (Fig. 4.7(b)), since it is induced by the

[8] The data was taken by Prof. Haibin Zhao's group in Fudan University.

modulation of the interfacial exchange-coupling effect between the metal layer and the ferromagnetic semiconductor layer.

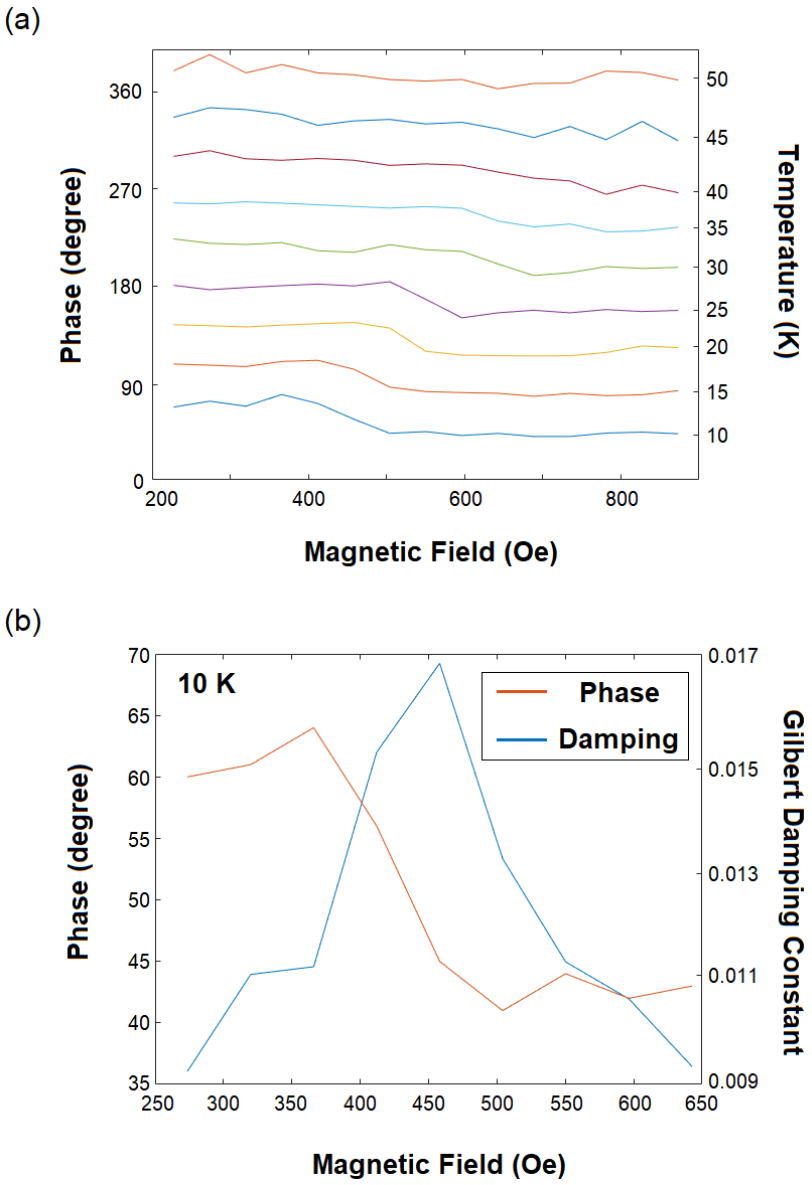

Figure 4.7 (a) Phase of magnetization precession as a function of external applied field at different temperatures from 10 K to 50 K. (b) Phase-angle and Gilbert damping constant of magnetization precession as

a function of external applied field at 10 K. The red curve indicates the phase-angle, while the blue curve represents the Gilbert damping constant.

References:

[1] Tserkovnyak, Y., Brataas, A., & Bauer, G. E. (2002). Enhanced Gilbert damping in thin ferromagnetic films. *Physical review letters*, *88*(11), 117601.

[2] Heinrich, B., Tserkovnyak, Y., Woltersdorf, G., Brataas, A., Urban, R., & Bauer, G. E. (2003). Dynamic exchange coupling in magnetic bilayers. *Physical review letters*, *90*(18), 187601.

[3] Stenning, G. B. G., Shelford, L. R., Cavill, S. A., Hoffmann, F., Haertinger, M., Hesjedal, T., ... & de Groot, P. A. J. (2015). Magnetization dynamics in an exchange-coupled NiFe/CoFe bilayer studied by x-ray detected ferromagnetic resonance. *New Journal of Physics*, *17*(1), 013019.

[4] van der Laan, G. (2017). Time-resolved X-ray detected ferromagnetic resonance of spin currents. *Journal of Electron Spectroscopy and Related Phenomena*, *220*, 137-146.

[5] Saitoh, E., Ueda, M., Miyajima, H., & Tatara, G. (2006). Conversion of spin current into charge current at room temperature: Inverse spin-Hall effect. *Applied physics letters*, *88*(18), 182509.

[6] Costache, M. V., Sladkov, M., Watts, S. M., Van Der Wal, C. H., & Van Wees, B. J. (2006). Electrical detection of spin pumping due to the precessing magnetization of a single ferromagnet. *Physical review letters*, *97*(21), 216603.

[7] Figueroa, A. I., Baker, A. A., Collins-McIntyre, L. J., Hesjedal, T., & van der Laan, G. (2016). Spin pumping through a topological insulator probed by x-ray detected ferromagnetic resonance. *Journal of Magnetism and Magnetic Materials*, *400*, 178-183.

[8] Shiomi, Y., Nomura, K., Kajiwara, Y., Eto, K., Novak, M., Segawa, K., ... & Saitoh, E. (2014). Spin-electricity conversion induced by spin injection into topological insulators. *Physical review letters*, *113*(19), 196601.

[9] Shikoh, E., Ando, K., Kubo, K., Saitoh, E., Shinjo, T., & Shiraishi, M. (2013). Spin-pump-induced spin transport in p-type Si at room temperature. *Physical review letters*, *110*(12), 127201.

[10] Žutić, I., & Dery, H. (2011). Spintronics: Taming spin currents. *Nature materials*, *10*(9), 647.

[11] Ando, K., Takahashi, S., Ieda, J., Kurebayashi, H., Trypiniotis, T., Barnes, C. H. W., ... & Saitoh, E. (2011). Electrically tunable spin injector free from the impedance mismatch problem. *Nature materials*, *10*(9), 655.

[12] Danilov, A. P., Scherbakov, A. V., Glavin, B. A., Linnik, T. L., Kalashnikova, A. M., Shelukhin, L. A., ... & Yakovlev, D. R. (2018).

Optically driven spin pumping mediating collective magnetization dynamics in a spin valve structure. *arXiv preprint arXiv:1805.07669*.

[13] Tserkovnyak, Yaroslav, Arne Brataas, and Gerrit EW Bauer. "Spin pumping and magnetization dynamics in metallic multilayers." *Physical Review B* 66.22 (2002): 224403.

[14] Tserkovnyak, Yaroslav, et al. "Nonlocal magnetization dynamics in ferromagnetic heterostructures." *Reviews of Modern Physics* 77.4 (2005): 1375.

[15] Wang, K. Y., Sawicki, M., Edmonds, K. W., Campion, R. P., Maat, S., Foxon, C. T., ... & Dietl, T. (2005). Spin reorientation transition in single-domain (Ga, Mn) As. *Physical review letters*, *95*(21), 217204.

[16] Marcham, M. K., Shelford, L. R., Cavill, S. A., Keatley, P. S., Yu, W., Shafer, P., ... & Telling, N. D. (2013). Phase-resolved x-ray ferromagnetic resonance measurements of spin pumping in spin valve structures. *Physical Review B*, *87*(18), 180403.

[17] Li, J., Shelford, L. R., Shafer, P., Tan, A., Deng, J. X., Keatley, P. S., ... & Qiu, Z. Q. (2016). Direct detection of pure ac spin current by x-ray pump-probe measurements. *Physical review letters*, *117*(7), 076602.

[18] Baker, A. A., Figueroa, A. I., Pingstone, D., Lazarov, V. K., Van Der Laan, G., & Hesjedal, T. (2016). Spin pumping in magnetic trilayer structures with an MgO barrier. *Scientific reports*, *6*, 35582.

[19] Baker, A. A., Figueroa, A. I., Love, C. J., Cavill, S. A., Hesjedal, T., & Van Der Laan, G. (2016). Anisotropic absorption of pure spin currents. *Physical review letters*, *116*(4), 047201.

Chapter 5

Conclusion

The fundamental understandings of the ultrafast magnetization dynamics and interfacial exchange coupling interaction provide a promising pathway of low power spin manipulation in the design and application of advanced spintronic devices. In this dissertation, a detailed study of the dynamic exchange coupling effect and photo-enhanced Gilbert damping constant $\boldsymbol{\alpha}$ is performed on the ferromagnetic metal/ferromagnetic semiconductor exchange-coupled bilayer heterostructure – $Co_2FeAl(Ga,Mn)As$.

The time-resolved magneto optical Kerr effect (TRMOKE) is utilized to investigate the ultrafast spin dynamics. A coherent magnetization precession is observed in the exchange-coupled $Co_2FeAl/(Ga,Mn)As$ bilayer system. The efficiency of magnetization precession excitation induced by laser pulses can be significantly improved in the ferromagnetic bilayer, which establishes a large interfacial exchange-coupling strength $\boldsymbol{J_1}$. The low-fluence, near-infrared pump-light excitation creates spin-polarized hot carriers which recombine at the interface by transferring spin between the two ferromagnets, inducing a dynamic exchange coupling that noticeably enhances interfacial exchange-coupling strength $\boldsymbol{J_1}$. The photo-

excited coherent spin precession persist to room temperature, though the precession amplitude drops significantly around the Curie temperature of (Ga,Mn)As, indicating that the proximity-induced ferromagnetism plays a crucial role in the optical excitation mechanism of coherent spin precession in Co_2FeAl/(Ga,Mn)As bilayer.

Furthermore, a photo-induced enhancement of the Gilbert damping constant in the Co_2FeAl/(Ga,Mn)As bilayer is studied. At temperatures below $\boldsymbol{T_C}$ = 50 K of the (Ga,Mn)As layer, the low power laser pulses induce a modulation of the interfacial exchange coupling effect, which causes the magnetizations in both ferromagnetic layers to precess along their own equilibrium directions. Under the counter-precessing exchange-coupled mode created by the photoexcited torque $\Delta\boldsymbol{\tau_{ex}(t)}$, the precessing magnetization in the Co_2FeAl layer transfers a pure spin current directly into the (Ga,Mn)As layer without passing through a nonmagnetic metal spacer layer. This results in an enhanced Gilbert damping at the resonance magnetic field. A corresponding phase shift of the magnetization precession is also observed at the resonance field due to the dynamic exchange coupling mechanism.

Our results highlight the importance of considering the range of interfacial exchange interactions in ferromagnetic heterostructures and will help promote the development of low-energy consumption magnetic device concepts for ultrafast spin manipulation.